

June. 2016

Vol. 9 No. 1
ISSN 2005-9043

Technical Review

Bio / Medical

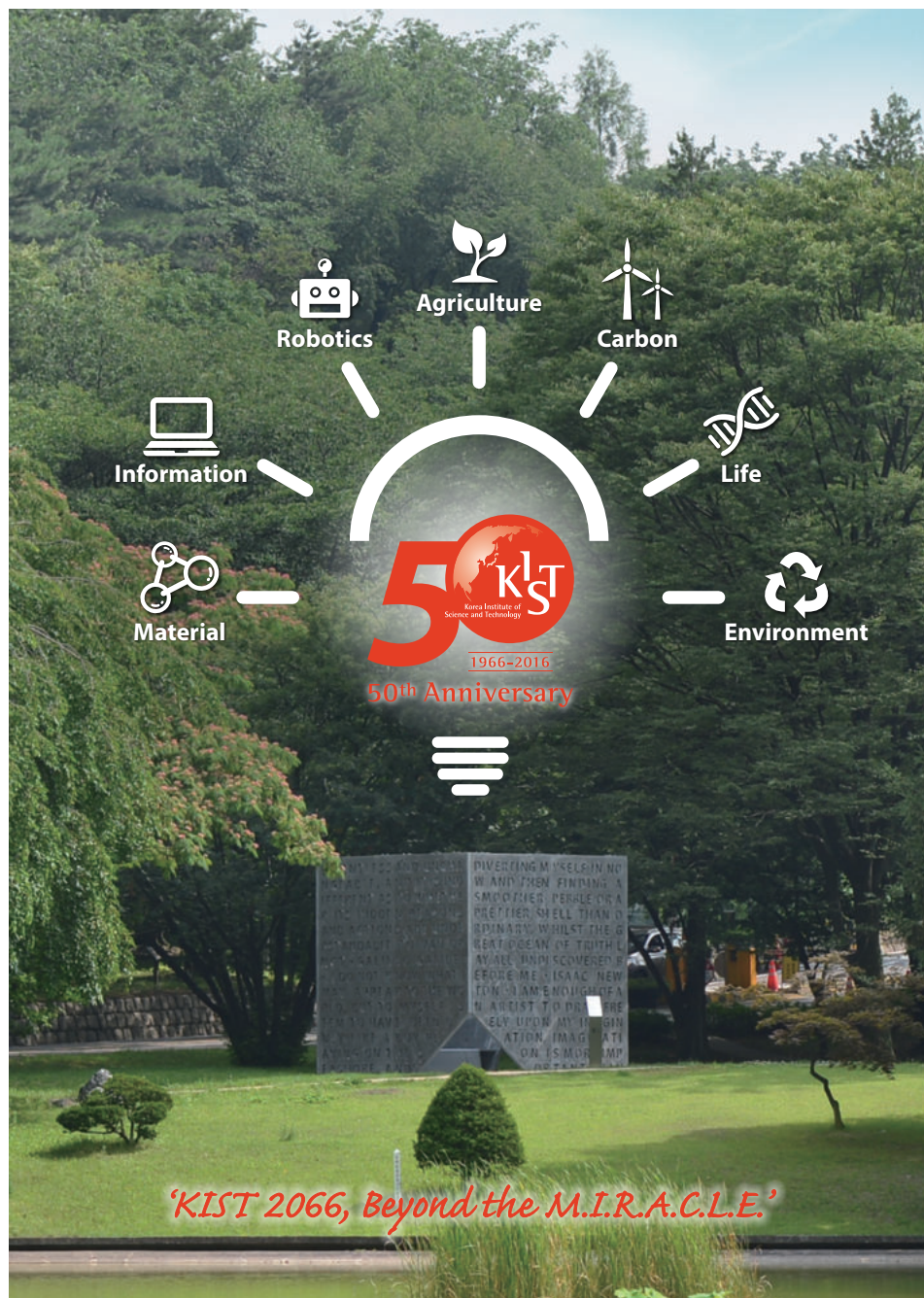
Targeting Amyloid- β Peptides in Plasma for Alzheimer's Blood Test

Materials / Systems

Neuromorphic Engineering Based on a Spiking Neural Network

Energy / Environment

Highly Efficient Ceria-Promoted Sb-V/TiO₂ Catalyst for the Abatement of NO_x by NH₃ from the Exhaust of Stationary and Marine Engines



Contents

Foreword	03
Bio / Medical	
Technical Review	
Targeting Amyloid- β Peptides in Plasma for Alzheimer's Blood Test	04
Feature Articles	
Bio-Lighted Nanotorch Capable of Systemic Self-Delivery and Diagnostic Imaging	16
Design of a Platform Technology for Systemic Delivery of siRNA to Tumors Using Rolling Circle Transcription	22
Materials / Systems	
Technical Review	
Neuromorphic Engineering Based on a Spiking Neural Network	30
Feature Articles	
Electrical Detection of Coherent Spin Precession Using the Ballistic Intrinsic Spin Hall Effect	37
Thermal Spin Transfer Torque Driven by Spin-Dependent Seebeck Effect in Metallic Spin-Valve Structures	43
Energy / Environment	
Technical Review	
Highly Efficient Ceria-Promoted Sb-V/TiO ₂ Catalyst for the Abatement of NO _x by NH ₃ from the Exhaust of Stationary and Marine Engines	48
Feature Articles	
Heavy Metal-Free Copper-Indium-Selenide Quantum Dot Solar Cells	58
Achieving Selective and Efficient Electrocatalytic Activity for CO ₂ Reduction Using Immobilized Silver Nanoparticles	64
Research Highlights	
Recent Publications	70
New Patents	73
KIST News	77
A Sign of the Times	82
Interview	84
About the Cover	87

Foreword

This is a banner year for our institute. It began with a celebration of our 50th anniversary in February, an occasion when we could reflect on the truly remarkable achievements attained through the skill and hard work of our researchers and support of our government, despite times of limited resources and other difficulties. KIST's early efforts launched a technological boom, particularly in the fields of heavy chemical industries, and also led to the establishment of many domestic companies, such as Pohang Iron and Steel Company (POSCO). According to the Korea Society of Innovation Management and Economics, KIST created a social and economic added value of about 600 trillion Korean Won over its first half century of operations.

This issue of *KISToday* highlights current research that is indicative of the new era of innovation and research excellence which will define us in our next 50 years. It is no coincidence that Thomson Reuters recently ranked KIST the 6th most innovative public research institute in the world. Our scientists are looking past traditional topics and approaches to engage in unique, pioneering projects that have particular relevance to future issues. For example, KIST recently succeeded in developing technology for the early detection of Alzheimer's disease and has already transferred that technology to a company for commercialization. Other projects, several of which you can read about in the following pages, involve quantum computing, neuromorphic engineering and other innovative fields whose research outcomes will determine how Korea will perform economically in the future.

The new vision for KIST, introduced at our anniversary celebration, is to move beyond the miracle represented by our first 50 years and undertake collaborative large-scale, long-term projects designed to benefit Koreans and the world at large. As always, we depend on you, our friends and supporters, to make our journey successful.

Dr. Byung Gwon LEE
President of KIST



Technical Review

Targeting Amyloid- β Peptides in Plasma for Alzheimer's Blood Test



Young Soo KIM

Convergence Research Center for
Diagnosis, Treatment and Care System
of Dementia
yskim@kist.re.kr

Introduction

Blood amyloid- β ($A\beta$) is an attractive biomarker of Alzheimer's disease (AD) for the well-characterized efflux mechanism to pass the blood-brain barrier (BBB); the low-density lipoprotein receptor-related protein-1 in BBB allows brain $A\beta$ to be actively transported to blood [1, 2]. Thus, quantification of plasma $A\beta$ is considered as an emerging diagnostic tool for AD [2, 3]. Indeed, recent clinical studies have reported association of reduced $A\beta(1-42)$ level in plasma with cognitive decline and risk development of AD [1,4-6]. However, contrasting cross-sectional cases have claimed the medical use of blood-based $A\beta$ measurements to be debatable [7-10]; heterogeneity of patient groups and assay protocols may have contributed to the provocative results.

The diagnostic potential of plasma $A\beta$ in AD has been receiving attention because previous clinical studies indicated a possible relationship between increased risk of AD and lowered $A\beta(1-42) / A\beta(1-40)$ ratio due to the decrease in plasma $A\beta(1-42)$ concentrations [4, 11-14]. A meta-analysis of 13 studies that assessed the potential of plasma $A\beta$ as a diagnostic tool also reported a possibility of increased plasma $A\beta(1-40)$ leading to subsequent cognitive decline [1]. If the $A\beta$ concentration changes in the plasma can reflect the progression of AD in patients, it would enable the diagnosis of AD using less costly and less invasive methods. However, because there are studies that found either decreased or no meaningful changes in the plasma

A β level of AD patients [15-17], the potential of using the plasma A β measurements for AD diagnosis has been continuously debated. At this point, there is not enough evidence to acknowledge the level of plasma A β as a reliable biomarker for AD diagnosis yet. When human AD studies build their AD patient pool, the diagnosis of probable AD is made based on the patient's cognitive impairments described by the criteria of the National Institute of Neurological Disorders and Stroke and the AD and Related Disorders Association [18, 19]. These human studies select patients with clinical diagnosis and study their A β abnormalities because the A β plaque deposition proceeds cognitive impairments in AD patients [20, 21]. Current AD diagnosis can be confirmed with A β abnormalities detected by neuroimaging. Alternatively, measurements of A β in the cerebrospinal fluid (CSF) is known to reflect AD pathology in the brain [22-24]. If there were a method to diagnose AD prior to the A β plaque deposition in the brain, diagnosis and treatment of patients in early AD stages would be possible, even before at risk individuals develop cognitive impairments. This possibility led us to search for plasma biomarkers with diagnostic potentials for early AD stage.

Correlations of A β concentrations between CSF and plasma

Dissimilar aspects of plasma A β analysis in varied subjects are also observed in amyloid precursor protein (APP) transgenic mouse models. Studies of two APP mouse models with different point mutations argue

that the surrogate scale of plasma A β reflected A β abnormalities in CSF of AD brains [25, 26]. During the plaque formation, PDAPP mice, with Indiana APP mutation, lose the correlation between plasma and CSF A β ; meanwhile, Tg2576 mice, with Swedish APP mutation, show a significant and simultaneous decrease in both CSF and plasma A β . Thus, it is critical to proceed a clinical investigation of plasma A β for its validity as a surrogate marker of risk development of AD under controlled milieu.

The A β -infusion mouse model offers benefits to minimize neuropathological factors of AD over the use of APP overexpressing transgenic rodents [27]. In APP transgenic models, it is difficult to control isomer types, species and concentration of A β in their brains. Such diversity would interfere targeted diagnosis of A β in antibody-based measurements and may produce contrasting results depending on models. On the other hand, A β -infusion animal model allows administration of defined quantity and species of A β isomers and reduction of individual differences within each study group [27]. By mimicking certain aspects of AD with designated infusion of A β , researchers can bypass the aging process and acutely focus on downstream pathology of A β abnormality between plasma and CSF. Here, we examined the dynamic equilibrium of A β (1-42) between the brain and plasma after ICV injection of synthetic A β (1-42) monomers to normal ICR mice.

Despite the benefits to introducing A β -focused environments, it is critical to assess if the A β injection induces AD-like learning and memory impairments in this animal model before studying the surrogate role of

Table 1. Determined A β (1-42) concentration of CSF and plasma (mean \pm SD).

Injected A β (1-42) amount (nmole)	0 (vehicle)	0.25	0.5	2	4
CSF A β (1-42) conc. (pg/mL)	127.66 \pm 110.65	236.52 \pm 154.29	717.02 \pm 496.11	1,319.15 \pm 1516.58	3,431.91 \pm 1264.42
Plasma A β (1-42) conc. (pg/mL)	208.08 \pm 29.79	504.90 \pm 342.13	1,434.68 \pm 627.72	3,002.84 \pm 605.29	14,719.15 \pm 7,210.06

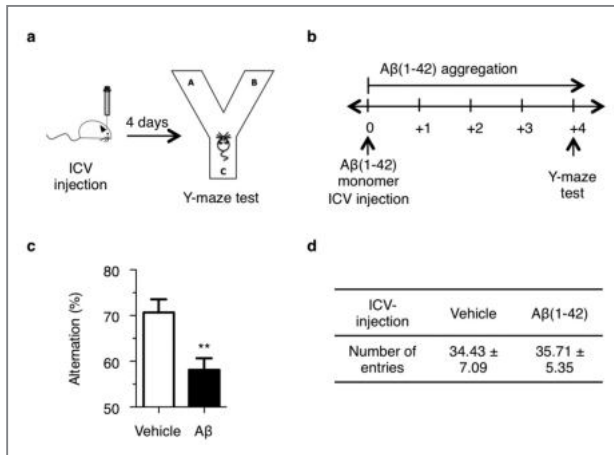


Figure 1. Y-maze test of Aβ-infused mouse model. (a) Experimental scheme (drawn by SM Cho) and (b) schedule of Y-maze test. (c) Spontaneous alternations in percent (mean ± SD, $p = 0.007$). (d) Number of arm entries (mean ± SD)

plasma Aβ to predict at-risk AD subjects. We performed Y-maze tasks to assess working memory alternations by measuring spontaneous alternation behaviors (Figure 1a,b) [28]. In a three-armed Y-shaped maze, the subjected animal must remember the order of arm entries, and the superior alternation rate indicates the better sustained cognition. Working memory ability and locomotion levels were determined as percent alternation and total arm entries, respectively, on the Y-maze. We found that single ICV injection of Aβ(1-42) monomers (0.25 nmole) significantly reduced cognitive behavioral performance on the Y-maze task when compared to vehicle-injected normal adult ICR mice (Figure 1c,d), without affecting locomotion levels.

In AD brains, alternations of CSF Aβ(1-42) levels were reversely correlated with progressive deposition of insoluble Aβ-plaques and development of AD [21, 29]. To mimic alternations of CSF Aβ levels in AD, we injected diverse concentrations of Aβ(1-42) (0, 0.25, 0.5, 2 and 4 nmole) in parallel into the ICV region of normal adult ICR mice (male, $n = 5$ per group). We collected CSF by laboratory-produced capillary tubes with tapered tips as previously described [30]. In sandwich ELISA

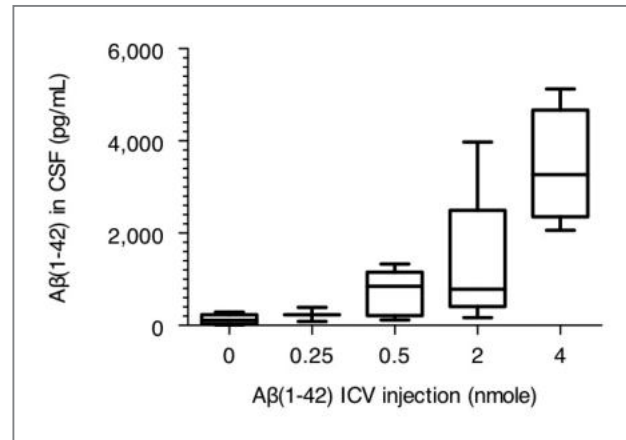


Figure 2. Concentration in CSF Aβ(1-42) after ICV injection. CSF was collected 30 minutes after ICV injection of Aβ(1-42) in serial amounts; 0, 0.25, 0.5, 2 and 4 nmole. Concentrations of Aβ(1-42) in CSF were measured using sandwich-ELISA.

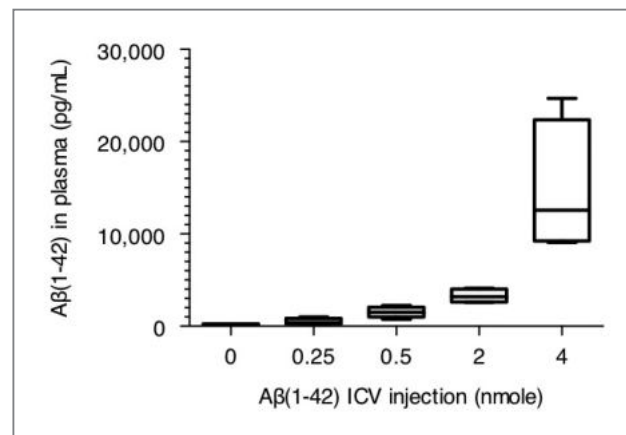


Figure 3. Concentration in plasma Aβ(1-42) after ICV injection. Plasma was collected 30 minutes after ICV injection of Aβ(1-42) in serial amounts; 0, 0.25, 0.5, 2 and 4 nmole. Concentrations of Aβ(1-42) in plasma were measured using sandwich-ELISA.

utilizing two anti-Aβ antibodies with different epitopes, we confirmed that CSF Aβ(1-42) levels directly replicated dose-dependency of the injected peptides (Figure 2 and Table 1) (Kruskal-Wallis test, $P = 0.0076$). After the CSF collection, we transferred blood from vena cava directly to EDTA tubes and isolated plasma. In order to assess validity of plasma Aβ as an AD surrogate biomarker, we measured Aβ(1-42) levels in plasma samples of

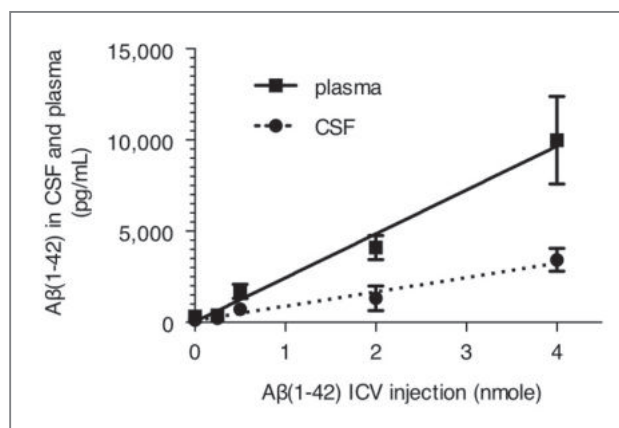


Figure 4. Comparison of Aβ(1-42) levels between CSF and plasma.

mice subjected to aforementioned CSF studies by the sandwich ELISA. We found that the levels of plasma Aβ(1-42) correspondingly elevated as we increased the amount of ICV-injected Aβ(1-42) monomers in mice (Figure 3 and Table 1) (*Kruskal-Wallis* test, $P = 0.0008$). Collectively, these results indicated that plasma Aβ(1-42) levels acutely reflected alternations of the CSF Aβ(1-42) concentration (Figure 4).

In this study, we compared Aβ(1-42) levels in CSF and plasma of at-risk AD model mice. We artificially raised amounts of Aβ(1-42) monomers in CSF of normal adult ICR mice by ICV injection and observed the corresponding increase of Aβ(1-42) levels in plasma. Our results correspond to two conflicting studies using APP transgenic mouse models; these studies conditionally agree on the significant association between CSF and plasma Aβ before the development of plaque deposition [25, 26]. Given that these transgenic mice have different genetic backgrounds and mutations, asymmetrical aspects of CSF-plasma Aβ ratio in these studies indicate strong needs for blood biomarker investigations to adopt Aβ specific animal models without additional neuropathological factors. Thus, we restricted neuropathology of subjected animals to abnormal increase of brain Aβ and measured Aβ levels considering the half-time for brain efflux of the peptide [31]. As we

intended to create Aβ-focused environment in mice, our study lacks many pathophysiological mechanisms in AD such as chronic processing and clearance of Aβ. Thus, additional studies are warranted to determine whether the correlation between plasma and CSF Aβ will translate into AD diagnosis within diverse neuropathological conditions.

Age-dependent inverse correlations in CSF and plasma Aβ(1-42) concentrations

A significant correlation between Aβ concentrations in the CSF and plasma were identified when we measured the Aβ levels prior to the plaque formation in the brain of transgenic mice. However, such correlations gradually disappeared as our mice aged and developed Aβ plaques in their brains. We hypothesized that the concentration changes in plasma Aβ can be utilized as a reliable biomarker for early diagnosis of AD prior to the plaque formation. In order to evaluate our hypothesis, we selected APP_{swe}, PS1_{M146V} and Tau_{p301L} transgenic (3xTg-AD) mice, which imitate human AD pathophysiologies including age-dependent behavioral and cognitive alterations. The 3xTg-AD mice show cognitive deficits in the Morris water maze at 6 months of age and present visible Aβ plaque deposition in the brain at 6 months of age [32-36]. They are also known to develop Aβ plaques more slowly compared with other transgenic mice, making the 3xTg-AD model fit for studying the relationship between AD and the plasma and CSF Aβ level alterations before the plaque formation.

In this study, we first confirmed the absence of ThS positive amyloid plaques, dense-core plaques, in the brains of young 3xTG-AD mice with immunohistochemical staining. We then measured the changes in concentration of Aβ(1-42) and Aβ(1-40) in the CSF and plasma of 5-, 7-, 9- and 12-month-old female transgenic mice using sandwich-ELISA to define a

relationship between the plasma A β and AD progression and, also, to confirm the diagnostic potential of the plasma A β prior to the plaque formation. We previously found that soluble monomeric A β (1-42) in the brain could pass the blood-brain barrier and can be found in the plasma [37]. To further confirm our hypothesis regarding the impact of plaque formation, we also assessed the

permeability of the blood-brain barrier to insoluble fibrillary A β (1-42) in 7-week-old ICR mice and studied whether plasma A β (1-42) can reflect the condition of brain A β (1-42) even after the plaque deposition.

Here, female 3xTg-AD mice aged 5, 7, 9 and 12 months were selected to study changes in the plasma and CSF A β levels since ThS-positive A β plaques become detectable in the brain as early as 12 months of age (female; 5-month, n = 32; 7-, 9- and 12-month, n = 33) [35]. To confirm the absence of ThS-positive A β plaque in the brains of transgenic mice prior to A β measurements, brain samples from each age group were cyrosectioned and fixed with 4% paraformaldehyde for 72 hours, which is different from widely used protocols in other studies [36, 38]. Then, they were stained with ThS for β -sheet-rich A β dense-core plaques, 6E10 antibody for both A β diffuse and dense-core plaques, DAPI for overall brain visualization and pS199 for hyperphosphorylated tau. We did not observe neither ThS- nor 6E10-positive plaques in the brain of 5-month-old mice (Figure 1a). 6E10 immunostaining showed diffuse plaques in the hippocampal regions of 7-, 9- and 12-month-old female 3xTg-AD mice (Figure 1a and 1b). In addition to the extracellular 6E10-positive plaques, we observed 6E10-stained neural cells from 7-month-old 3xTg-AD mice (Figure 1a). Of the ThS stained brain slices, only the 12 month-old 3xTg-AD mice showed ThS-positive, dense-core, A β plaque depositions in the brain (Figure 1b). In addition, we observed accumulations of hyperphosphorylated tau tangles in the brain of 12-month-old 3xTg-AD mice.

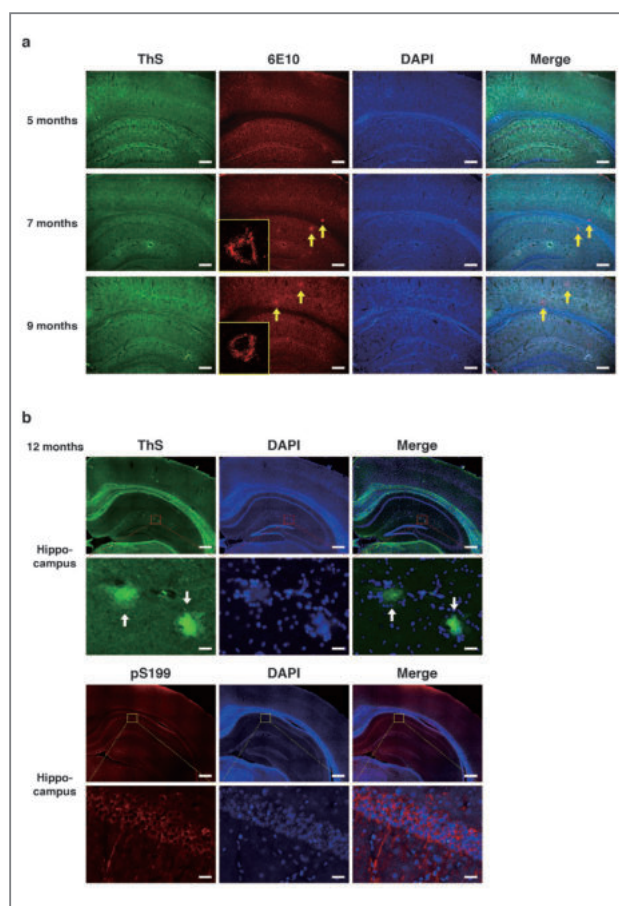


Figure 5. Age-dependent A β plaque deposition and hyperphosphorylated tau in the 3xTg-AD mice brain stained by ThS and IHC staining. 5-, 7-, 9- and 12-month-old female 3xTg-AD AD mice brains stained with ThS for β -sheet-rich A β plaques, 6E10 for detection of A β species and pS199 for hyperphosphorylated tau. (a) Hippocampus and cortex of 5-, 7-, 9- and 12-month-old female 3xTg-AD mice stained for A β plaques. Yellow boxes indicate whole-cell 6E10 immunostaining by confocal microscopy. Scale bar = 200 μ m. (b) Hippocampus of 12-month-old female 3xTg-AD mice stained for hyperphosphorylated tau and A β plaque. Scale bar = 1 mm (*upper*) and 200 μ m (*lower*). Yellow arrows indicate diffused A β plaque and white arrows indicate ThS positive A β plaque.

Decreased A β levels in CSF is a clinical indication of AD progression. To confirm the alterations of CSF A β levels in 3xTg-AD mice mimics those in AD patients, the levels of A β (1-42) in the CSF of 5-, 7-, 9- and 12-month-old 3xTg-AD mice were measured with sandwich-ELISA utilizing two anti-A β antibodies with different epitopes. The CSF was collected using laboratory-produced capillary tubes with tapered tips as previously described [39] and then we measured the levels of A β (1-42) and

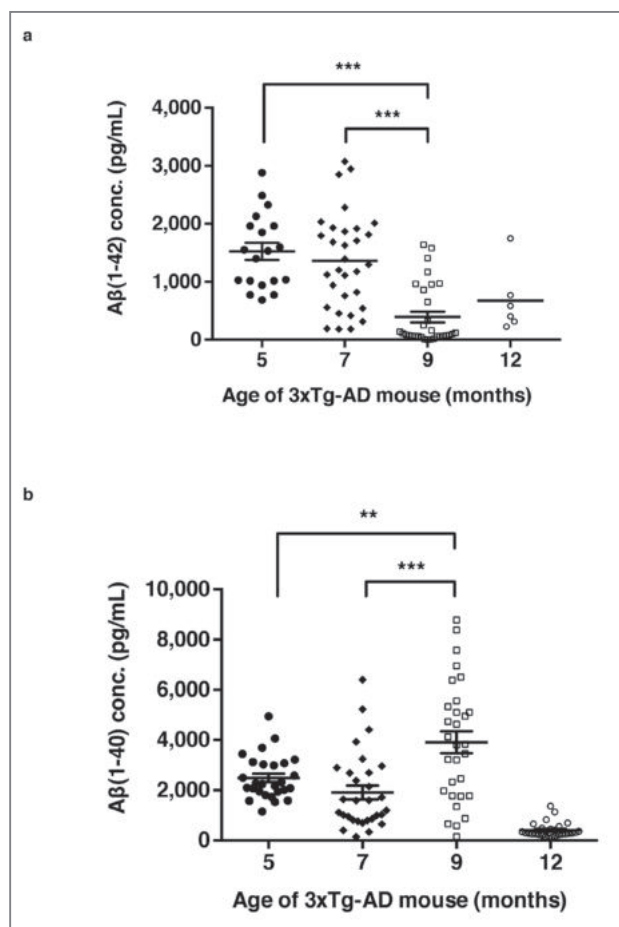


Figure 6. Age-dependent changes in A β (1-42) and A β (1-40) concentrations in the 3xTg-AD mice CSF (excluding saturated data). 5-, 7-, 9- and 12-month-old female 3xTg-AD AD mice A β in the CSF were measured using sandwich-ELISA. Data presented with scatter dot plot (mean \pm SEM). (a) A β (1-42) concentration in CSF (5-month, n = 19; 7-month, n = 31; 9-month, n = 31; 12-month, n = 6) and (b) A β (1-40) concentration in CSF (5-month, n = 27; 7-month, n = 30; 9-month, n = 30; 12-month, n = 30). The error bars represent the SEMs. One-way ANOVA followed by Bonferroni's post-hoc comparisons tests were performed in all statistical analyses (* P < 0.05, ** P < 0.01, *** P < 0.001; other comparisons were not significant).

A β (1-40). The concentration of A β (1-42) in the CSF of 3xTg-AD mice showed an age-dependent decrease with a statistical significance before the age of 12 months (female; 5-month, n = 19; 7-month, n = 31; 9-month, n = 31; 12-month, n = 6, P < 0.0001 for 5-month-old vs. 7-month-old and 7-month-old vs. 9-month-old, **Figure 2a**) (13 out of 32 brains from 5-month-old and 27 out of 33

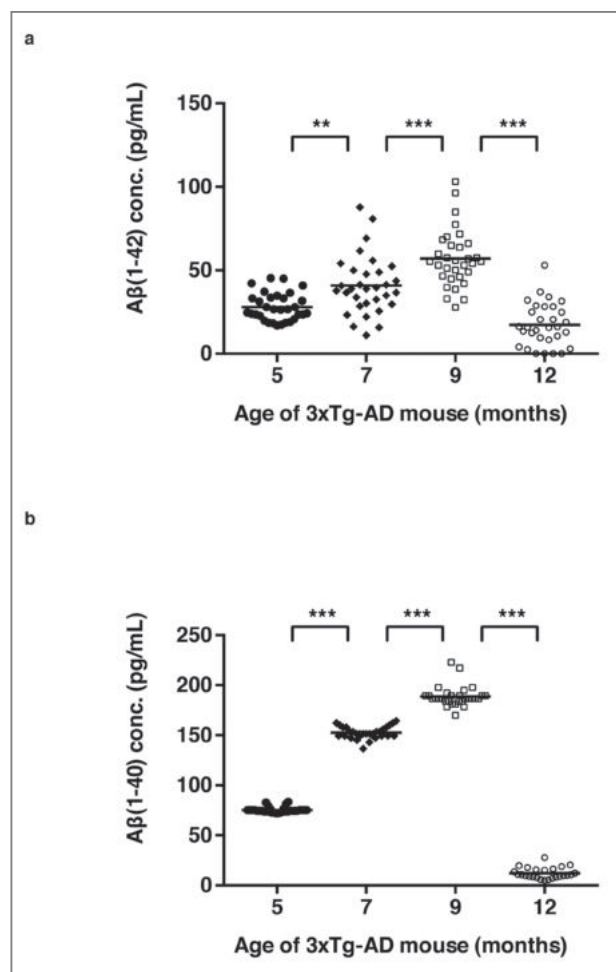


Figure 7. Age-dependent changes in A β (1-42) and A β (1-40) concentrations in the 3xTg-AD mice plasma. 5-, 7-, 9- and 12-month-old female 3xTg-AD mice A β (1-42) in the plasma were measured using sandwich-ELISA. Data presented with scatter dot plot (mean \pm SEM). (a) A β (1-42) concentration in plasma (5-month, n = 32; 7-month, n = 32; 9-month, n = 32; 12-month, n = 31) and (b) A β (1-40) concentration in plasma (5-month, n = 32; 7-month, n = 31; 9-month, n = 30; 12-month, n = 25). The error bars represent the SEMs. One-way ANOVA followed by Bonferroni's post-hoc comparisons tests were performed in all statistical analyses (* P < 0.05, ** P < 0.01, *** P < 0.001; other comparisons were not significant).

brains from 12-month-old groups were excluded from the results due to saturated values during ELISA readings). After the formation of ThS-positive plaques, the CSF A β (1-42) level no longer showed a decrease in the trend. On the contrary, we did not observe distinguishable trend in the age-dependent alterations of CSF A β (1-40) levels

($P = 0.0049$ for 5-month-old vs. 9-month-old, $P < 0.0001$ for 7-month-old vs. 9-month-old, **Figure 2b**). Our results agree with previous studies on the age-dependent decline of CSF A β (1-42) levels in both AD patients and animal models.

In order to study if the plasma A β level changes in an age-dependent manner in the 3xTg-AD mice, we measured the concentration of plasma A β (1-42) in the aforementioned mice used in the CSF A β measurements. The blood was first transferred directly from the vena cava to EDTA-containing tubes and the plasma was isolated using centrifugation. Then we measured the levels of A β (1-42) and A β (1-40). In contrast to the CSF measurements, we found that plasma A β (1-42) levels increased from 5- to 9-month-old 3xTg-AD mice (female; 5-month, $n = 32$; 7-month, $n = 32$; 9-month, $n = 32$, **Figure 3a**). Notably, the plasma A β (1-42) levels decrease in 12-month-old mice, of which brains only developed ThS-positive dense core plaques and hyperphosphorylated tau tangles (12-month, $n = 31$, **Figure 3a**). All the results were statistically significant by one-way ANOVA followed by Bonferroni's post-hoc comparisons ($P = 0.003$ for 5-month-old vs. 7-month-old, $P < 0.0001$ for 7-month-old vs. 9-month-old, $P < 0.0001$ for 9-month-old vs. 12-month-old). We observed identical trends in the alterations of plasma A β (1-40) to those of plasma A β (1-42). Between 5-, 7- and 9-month-old groups, 3xTg-AD mice showed significantly increasing levels of A β (1-40) in the plasma, whereas the 12-month-old group showed substantial decline ($P < 0.0001$ for 5-month-old vs. 9-month-old, $P < 0.0001$ for 7-month-old vs. 9-month-old, **Figure 3b**).

To directly compare the age-dependent alterations in A β levels, the A β (1-42) and A β (1-40) concentrations in the plasma and CSF were plotted onto the same graph. The graph shows that the A β (1-42) concentrations in the plasma increases with age while the A β (1-42) concentrations in the CSF decreases, indicating inverse correlations between the A β (1-42) levels in the plasma and CSF (**Figure 4a**). However, as there was no trend

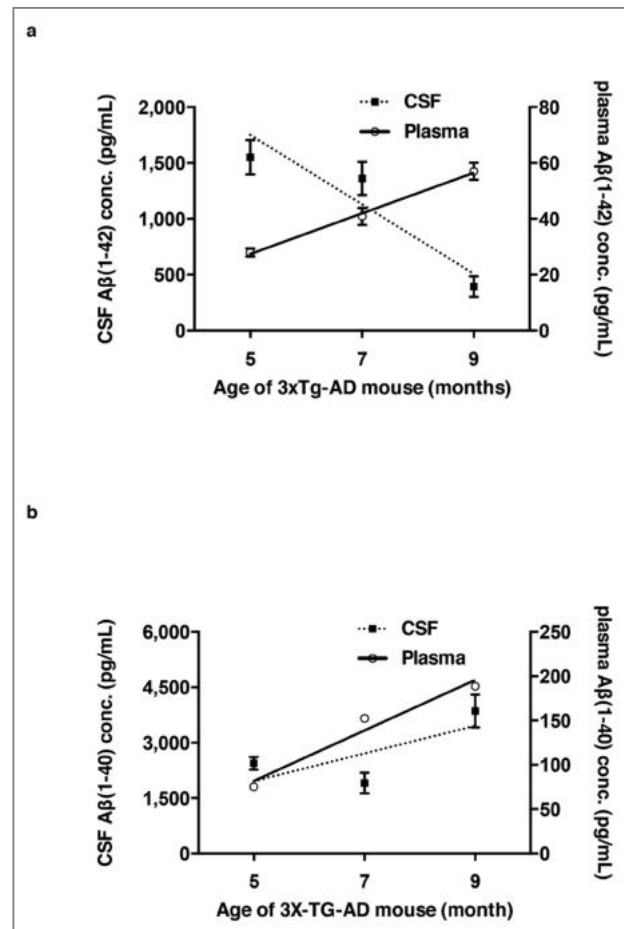


Figure 8. Comparison of age-dependent changes in A β (1-42) and A β (1-40) concentrations in 3xTg-AD mice between CSF and plasma. (a) Correlation of A β (1-42) concentrations between CSF and plasma of 5-, 7- and 9-month-old female 3xTg AD mice (CSF : $r = -0.9324$, $P < 0.0001$ / Plasma : $r = 0.9978$, $P < 0.0001$). (b) Correlation of A β (1-40) concentrations between CSF and plasma of 5-, 7- and 9-month-old female 3xTg AD mice (CSF : $r = 0.7030$, $P < 0.005$ / Plasma : $r = 0.9791$, $P < 0.0001$). The error bars represent the SEMs. One-way ANOVA followed by Bonferroni's post-hoc comparisons tests were performed in all statistical analyses (* $P < 0.05$, ** $P < 0.01$, *** $P < 0.001$; other comparisons were not significant).

in CSF A β (1-40) levels, it was difficult to conclude any correlations between the A β (1-40) levels in the plasma and CSF (**Figure 4b**). Collectively, our study concludes that the plasma A β (1-42) increases in age-dependent manner in 3xTg-AD mice and has the diagnostic potential for detecting AD until ThS-positive A β plaques form in the brain.

Because the blood-brain barrier is known to be permeable to soluble monomeric A β (1-42), plasma A β (1-42) is a viable candidate for early AD diagnosis. However, if the changes in plasma A β (1-42) levels can serve as a biomarker for AD only prior to the plaque formation in the brain, then the plasma should not be able to reflect the condition of brain A β (1-42), once the A β peptides become insoluble aggregates. Direct fibrillary A β injection to tissue enabled us to study the

blood-brain barrier's permeability to insoluble A β by measuring the levels of fibrillary A β in the plasma. As we observed ThS-negative diffuse plaques did not have an effect on the plasma levels of A β in 3xTg-AD mice, it is important to inject ThS-positive A β aggregates. Thus, we performed ThS fluorescence assays to confirm formation of ThS-positive aggregates before the intracerebral (IC) injections (Figure 5a). Then, we injected ThS-positive fibrillary A β (1-42) to the cortex of the brains of 7-week-old ICR mice (male, $n = 5$) by IC injection and assessed the permeability of the blood-brain barrier to fibrillary A β . We selected non-transgenic ICR mice for this study, since A β in the CSF of transgenic mice can potentially behave as a confounding factor. Additional 5 male ICR mice received IC injection with vehicle as controls. The blood was collected from the vena cava of the mice 30 minutes after the IC injection to allow sufficient time for fibrillary A β to pass the blood-brain barrier. After analyzing the plasma with sandwich-ELISA, no statistically significant differences in the plasma soluble A β concentrations of fibrillary A β -injected mice and vehicle-injected mice were found (Unpaired student's t -test, $P = 0.629$, Figure 5b). Therefore, the brain-blood barrier was not freely permeable to fibrillary A β (1-42), and the plasma A β (1-42) could not reflect the condition of brain A β (1-42) once they become insoluble plaques.

In this study, we found that the plasma A β (1-42) concentration increases in an age-dependent manner, while the level of CSF A β (1-42) decreases, indicating an inverse correlation between the plasma and CSF A β (1-42) levels in 3xTg-AD mice before dense-core A β plaque depositions appear in their brains. On the contrary, we did not observe such correlation in the alterations of A β (1-40) concentration between CSF and plasma. These results suggest that measuring the plasma A β (1-42) levels can function as an early diagnostic marker of AD. One previous comparison study involving the APP23 transgenic mice and the TG2576 mice also reported increasing plasma A β concentrations in age-dependent manner [40], and another comparison study

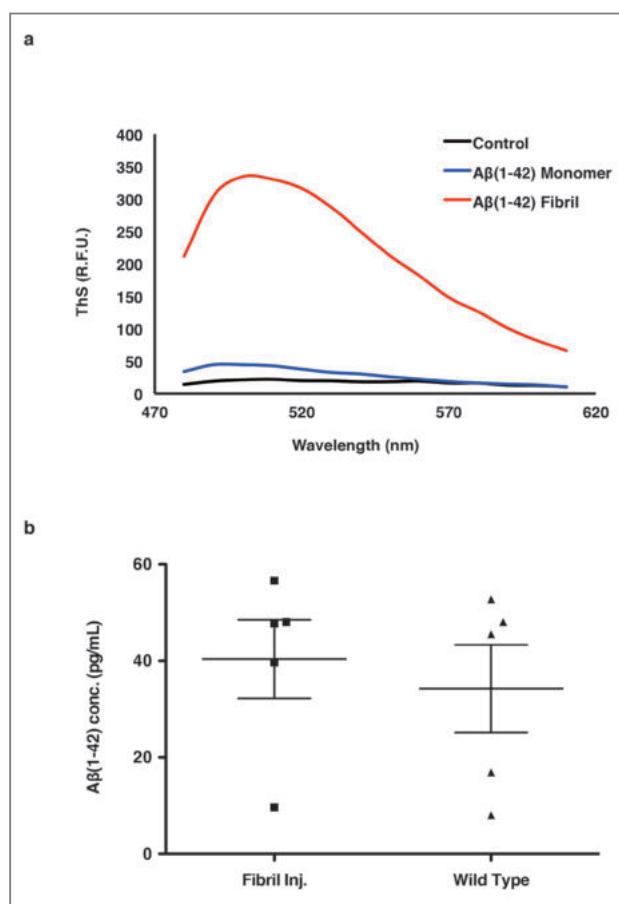


Figure 9. Evaluation of plasma A β (1-42) concentrations and ThS staining of fibrillary A β (1-42) after IC injection. (a) Excitation spectra of ThS ($\lambda_{\text{ex}} = 430$ nm) in the presence of vehicle, A β (1-42) monomer and fibrillary A β (1-42). R.F.U. refers to relative fluorescence units. (b) Plasma A β (1-42) concentrations of 7-week-old male ICR mice that received IC injection with fibrillary A β (1-42) and control ICR mice that received vehicle were measured using sandwich-ELISA. Data presented with scatter dot plot (mean \pm SD). The error bars represent the SEMs. Unpaired student's t -tests were performed in all statistical analyses (the comparison was not significant).

reported that in the amyloid precursor protein transgenic mouse models, A β concentrations in CSF decreases when A β deposition starts to appear [23], further supporting our inverse correlation of A β levels. Although other additional studies have investigated A β levels in the CNS, they did not directly compare the A β levels in the CSF and plasma before and after plaque formation. Our study has further determined the aforementioned issue.

Discussion

The former study provides assurance that the A β in plasma is an important target candidate for AD diagnosis. The concept of A β blood test is an unprecedentedly convenient tool for both physicians and patients to predict the pathological progress of AD. However, reliable measurements of plasma A β by overcoming cross-sectional diversity will subsequently confront the challenge as a valid surrogate biomarker for neurodegeneration of AD. Quantification of abnormal A β processing and clearance in the brain has been a major diagnostic method of AD. During the investigation of A β neuroimaging tracers, needs for additional biomarkers have been raised due to significant cases of non-demented, A β -positive individuals [41]. Thus, clinical evidences at present strongly support the view that diagnosis of AD requires detection of both A β and tau abnormalities [42]. As A β deposition timely leads to hyperphosphorylated tau aggregation followed by cerebral atrophy reduction, the former is considered useful for early diagnosis and the latter for neurodegeneration [21]. Given that plasma A β levels would limitedly reflect the status of A β abnormality in the central nervous system, further challenges of AD blood tests would be investigating additional blood surrogate markers of neurodegeneration [43]. Present findings propose that blood-based A β quantification should be investigated further as a possible surrogate biomarker for AD diagnosis.

Results of the latter study indicate that the plasma A β (1-42) concentration possesses a diagnostic potential as a biomarker for early diagnosis of AD when there is no ThS positive A β plaque depositions in the brain. This finding is important because it could provide a possible explanation for controversial results from previous studies on the A β measurements in blood. Although the plasma A β was thought to be related to AD progression and was suggested as a potential target for AD diagnosis, previous controversial results made it difficult to draw a meaningful conclusion. Our study shows that the plasma A β (1-42) levels increases with age and, therefore, it can be used as an early marker for AD progression. However, the plasma A β may not be an ideal biomarker for AD diagnosis in later developing stages of AD, since amyloid plaque formation makes the plasma A β measurements unreliable. The plasma A β (1-42) levels may become unable to reflect the AD prognosis after the plaque deposition because insoluble A β (1-42) cannot pass the blood-brain barrier as seen in this study. However, one study reported possible endothelial damages to the blood-brain barrier by A β (1-42) peptides, which will impair the barrier's function and increase its permeability [44]. Therefore, further study is recommended to warrant the diagnostic potential of plasma A β (1-42) levels after the plaque deposition in the brain.

It is not clear yet how the formation of amyloid plaques in the brain affects the age-dependent correlations between the plasma and CSF A β levels that we observed. Moreover, we only observed such correlations in female transgenic mice, which are known to develop amyloid plaques earlier than males [45, 46]. Thus, the underlying mechanism causing the inverse correlation between the plasma and CSF A β (1-42) levels needs to be further studied, and investigations with the Dominantly Inherited Alzheimer Network are desired for more clinical data [47]. Nonetheless, this study opens up more therapeutic strategies for AD patients and could potentially lead to development of more convenient and economic diagnosis of AD in its early stages.

Acknowledgments

This work was published by Scientific Reports (Scientific Reports 4, Article number: 6777 (2014) and Scientific Reports 6, Article number: 20185 (2016)). This work was supported by KIST Institutional Program (Open Research Program 2E24582).

References

- [1] Koyama, A. *et al.* Plasma amyloid-beta as a predictor of dementia and cognitive decline: a systematic review and meta-analysis. *Arch Neurol* 69, 824-831, doi:10.1001/archneurol.2011.1841 (2012).
- [2] Kang, D. E. *et al.* Modulation of amyloid beta-protein clearance and Alzheimer's disease susceptibility by the LDL receptor-related protein pathway. *J Clin Invest* 106, 1159-1166, doi:10.1172/JCI11013 (2000).
- [3] Jovanovic, K. *et al.* Anti-LRP/LR specific antibodies and shRNAs impede amyloid beta shedding in Alzheimer's disease. *Sci Rep* 3, 2699, doi:10.1038/srep02699 (2013).
- [4] Yaffe, K. *et al.* Association of plasma beta-amyloid level and cognitive reserve with subsequent cognitive decline. *Jama* 305, 261-266, doi:10.1001/jama.2010.1995 (2011).
- [5] Song, F., Poljak, A., Smythe, G. A. & Sachdev, P. Plasma biomarkers for mild cognitive impairment and Alzheimer's disease. *Brain Res Rev* 61, 69-80, doi:10.1016/j.brainresrev.2009.05.003 (2009).
- [6] Pesini, P. *et al.* Reliable Measurements of the beta-Amyloid Pool in Blood Could Help in the Early Diagnosis of AD. *Int J Alzheimers Dis* 2012, 604141, doi:10.1155/2012/604141 (2012).
- [7] Fukumoto, H. *et al.* Age but not diagnosis is the main predictor of plasma amyloid beta-protein levels. *Arch Neurol* 60, 958-964, doi:10.1001/archneur.60.7.958 (2003).
- [8] Schupf, N. *et al.* Elevated plasma amyloid beta-peptide 1-42 and onset of dementia in adults with Down syndrome. *Neurosci Lett* 301, 199-203 (2001).
- [9] Tamaoka, A. *et al.* Amyloid beta protein in plasma from patients with sporadic Alzheimer's disease. *J Neurol Sci* 141, 65-68 (1996).
- [10] Vanderstichele, H. *et al.* Standardization of measurement of beta-amyloid(1-42) in cerebrospinal fluid and plasma. *Amyloid* 7, 245-258 (2000).
- [11] Graff-Radford, N. R. *et al.* Association of low plasma A-beta42/Abeta40 ratios with increased imminent risk for mild cognitive impairment and Alzheimer disease. *Arch Neurol* 64, 354-362, doi:10.1001/archneur.64.3.354 (2007).
- [12] Schupf, N. *et al.* Peripheral Abeta subspecies as risk biomarkers of Alzheimer's disease. *Proceedings of the National Academy of Sciences of the United States of America* 105, 14052-14057, doi:10.1073/pnas.0805902105 (2008).
- [13] Schupf, N. *et al.* Change in plasma Aβ peptides and onset of dementia in adults with Down syndrome. *Neurology* 75, 1639-1644, doi:10.1212/WNL.0b013e-3181fb448b (2010).
- [14] Seppala, T. T. *et al.* Plasma Aβ42 and Aβ40 as markers of cognitive change in follow-up: a prospective, longitudinal, population-based cohort study. *Journal of neurology, neurosurgery, and psychiatry* 81, 1123-1127, doi:10.1136/jnnp.2010.205757 (2010).
- [15] Locascio, J. J. *et al.* Plasma amyloid beta-protein and C-reactive protein in relation to the rate of progression of Alzheimer disease. *Arch Neurol* 65, 776-785, doi:10.1001/archneur.65.6.776 (2008).
- [16] Sundelof, J. *et al.* Plasma beta amyloid and the risk of Alzheimer disease and dementia in elderly men: a prospective, population-based cohort study. *Arch Neurol* 65, 256-263, doi:10.1001/archneurol.2007.57 (2008).
- [17] van Oijen, M., Hofman, A., Soares, H. D., Koudstaal, P. J. & Breteler, M. M. Plasma Aβ(1-40) and Aβ(1-42) and the risk of dementia: a prospective case-cohort study. *Lancet Neurol* 5, 655-660, doi:10.1016/S1474-4422(06)70501-4 (2006).
- [18] Mehta, P. D. *et al.* Plasma and cerebrospinal fluid levels of amyloid beta proteins 1-40 and 1-42 in Alzheimer disease. *Arch Neurol* 57, 100-105, doi:10.1001/archneur.57.1.100. (2000).

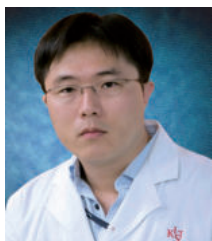
- [19] McKhann, G. *et al.* Clinical diagnosis of Alzheimer's disease: report of the NINCDS-ADRDA Work Group under the auspices of Department of Health and Human Services Task Force on Alzheimer's Disease. *Neurology* 34, 939-944, doi:http://dx.doi.org/10.1212/WNL.34.7.939 (1984).
- [20] Jack, C. R., Jr. *et al.* Serial PIB and MRI in normal, mild cognitive impairment and Alzheimer's disease: implications for sequence of pathological events in Alzheimer's disease. *Brain : a journal of neurology* 132, 1355-1365, doi:10.1093/brain/awp062 (2009).
- [21] Jack, C. R., Jr. *et al.* Hypothetical model of dynamic biomarkers of the Alzheimer's pathological cascade. *Lancet Neurol* 9, 119-128, doi:10.1016/S1474-4422(09)70299-6 (2010).
- [22] Maia, L. F. *et al.* Changes in amyloid-beta and Tau in the cerebrospinal fluid of transgenic mice overexpressing amyloid precursor protein. *Science translational medicine* 5, 194re192, doi:10.1126/scitranslmed.3006446 (2013).
- [23] Maia, L. F. *et al.* Increased CSF Aβ during the very early phase of cerebral Aβ deposition in mouse models. *EMBO molecular medicine* 7, 895-903, doi:10.15252/emmm.201505026 (2015).
- [24] Fagan, A. M. *et al.* Longitudinal change in CSF biomarkers in autosomal-dominant Alzheimer's disease. *Science translational medicine* 6, 226ra230, doi:10.1126/scitranslmed.3007901 (2014).
- [25] DeMattos, R. B. *et al.* Plaque-associated disruption of CSF and plasma amyloid-beta (Aβ) equilibrium in a mouse model of Alzheimer's disease. *J Neurochem* 81, 229-236 (2002).
- [26] Kawarabayashi, T. *et al.* Age-dependent changes in brain, CSF, and plasma amyloid (β) protein in the Tg2576 transgenic mouse model of Alzheimer's disease. *J Neurosci* 21, 372-381 (2001).
- [27] Van Dam, D. & De Deyn, P. P. Animal models in the drug discovery pipeline for Alzheimer's disease. *Br J Pharmacol* 164, 1285-1300, doi:10.1111/j.1476-5381.2011.01299.x (2011).
- [28] Bryan, K. J., Lee, H., Perry, G., Smith, M. A. & Casadesus, G. in *Methods of Behavior Analysis in Neuroscience Frontiers in Neuroscience* (ed J. J. Buccafusco) (2009).
- [29] Li, X. *et al.* Ratio of Aβ₄₂/P-tau_{181p} in CSF is associated with aberrant default mode network in AD. *Sci Rep* 3, 1339, doi:10.1038/srep01339 (2013).
- [30] Liu, L., Herukka, S. K., Minkevičienė, R., van Groen, T. & Tanila, H. Longitudinal observation on CSF Aβ₄₂ levels in young to middle-aged amyloid precursor protein/presenilin-1 doubly transgenic mice. *Neurobiol Dis* 17, 516-523, doi:10.1016/j.nbd.2004.08.005 (2004).
- [31] Shibata, M. *et al.* Clearance of Alzheimer's amyloid-ss(1-40) peptide from brain by LDL receptor-related protein-1 at the blood-brain barrier. *J Clin Invest* 106, 1489-1499, doi:10.1172/JCI10498 (2000).
- [32] Billings, L. M., Green, K. N., McGaugh, J. L. & LaFerla, F. M. Learning decreases Aβ*56 and tau pathology and ameliorates behavioral decline in 3xTg-AD mice. *J Neurosci* 27, 751-761, doi:10.1523/JNEUROSCI.4800-06.2007 (2007).
- [33] Billings, L. M., Oddo, S., Green, K. N., McGaugh, J. L. & LaFerla, F. M. Intraneuronal Aβ causes the onset of early Alzheimer's disease-related cognitive deficits in transgenic mice. *Neuron* 45, 675-688, doi:10.1016/j.neuron.2005.01.040 (2005).
- [34] Gimenez-Llort, L. *et al.* Modeling behavioral and neuronal symptoms of Alzheimer's disease in mice: a role for intraneuronal amyloid. *Neuroscience and biobehavioral reviews* 31, 125-147, doi:10.1016/j.neubiorev.2006.07.007 (2007).
- [35] Oddo, S. *et al.* Triple-transgenic model of Alzheimer's disease with plaques and tangles: intracellular Aβ and synaptic dysfunction. *Neuron* 39, 409-421, doi:10.1016/S0896-6273(03)00434-3 (2003).
- [36] Oh, K. J. *et al.* Staging of Alzheimer's pathology in triple transgenic mice: a light and electron microscopic analysis. *Int J Alzheimers Dis* 2010, doi:10.4061/2010/780102 (2010).
- [37] Cho, S. M. *et al.* Correlations of amyloid-beta concentrations between CSF and plasma in acute Alzheimer mouse model. *Sci Rep* 4, 6777, doi:10.1038/srep06777 (2014).

- [38] Kim, H. Y. *et al.* EPPS rescues hippocampus-dependent cognitive deficits in APP/PS1 mice by disaggregation of amyloid-beta oligomers and plaques. *Nature communications* 6, 8997, doi:10.1038/ncomms9997 (2015).
- [39] Liu, L. & Duff, K. A technique for serial collection of cerebrospinal fluid from the cisterna magna in mouse. *J Vis Exp*, doi:10.3791/960 (2008).
- [40] Kuo, Y. M. *et al.* The evolution of A beta peptide burden in the APP23 transgenic mice: implications for A beta deposition in Alzheimer disease. *Molecular medicine* 7, 609-618 (2001).
- [41] Duran-Aniotz, C., Morales, R., Moreno-Gonzalez, I., Hu, P. P. & Soto, C. Brains from non-Alzheimer's individuals containing amyloid deposits accelerate Abeta deposition in vivo. *Acta Neuropathol Commun* 1, 76, doi:10.1186/2051-5960-1-76 (2013).
- [42] Maruyama, M. *et al.* Imaging of tau pathology in a tauopathy mouse model and in Alzheimer patients compared to normal controls. *Neuron* 79, 1094-1108, doi:10.1016/j.neuron.2013.07.037 (2013).
- [43] Azhdarzadeh, M. *et al.* Serum multivalent cationic pattern: speculation on the efficient approach for detection of Alzheimer's disease. *Sci Rep* 3, 2782, doi:10.1038/srep02782 (2013).
- [44] Jancso, G. *et al.* Beta-amyloid (1-42) peptide impairs blood-brain barrier function after intracarotid infusion in rats. *Neurosci Lett* 253, 139-141, doi:10.1016/S0304-3940(98)00622-3 (1998).
- [45] Carroll, J. C. *et al.* Sex differences in beta-amyloid accumulation in 3xTg-AD mice: role of neonatal sex steroid hormone exposure. *Brain Res* 1366, 233-245, doi:10.1016/j.brainres.2010.10.009 (2010).
- [46] McCullough, L. D. *et al.* NIH initiative to balance sex of animals in preclinical studies: generative questions to guide policy, implementation, and metrics. *Biology of sex differences* 5, 15, doi:10.1186/s13293-014-0015-5 (2014).
- [47] Morris, J. C. *et al.* Developing an international network for Alzheimer research: The Dominantly Inherited Alzheimer Network. *Clinical investigation* 2, 975-984, doi:10.4155/cli.12.93 (2012).



Feature Articles

Bio-Lighted Nanotorch Capable of Systemic Self-Delivery and Diagnostic Imaging



Se Hoon KIM

Center for Theragnosis
Biomedical Research Institute
sehoonkim@kist.re.kr

Introduction

Sensitive imaging of inflammation with a background-free chemiluminescence (CL) signal has great potential as a clinically relevant approach for early diagnosis of various inflammatory diseases. However, to date, its feasibility has been demonstrated *in vivo* in only a limited way with locally induced inflammation models through *in situ* injection of CL probes. The focus of this article is on KIST's efforts in enabling systemic disease targeting and imaging by intravenous administration of CL probes. Our work has made significant progress by overcoming previous hurdles such as weak CL emission, short glowing duration and inadequate blood circulation time of conventional CL probes.

CL is the light emission produced by a specific chemical reaction whose intensity is proportional to the concentration of reactive analytes; it is useful for a wide range of analytical applications. Unlike photoluminescence (PL) by light excitation, CL measurements do not involve sources of background noise such as autofluorescence from biological specimens or stray excitation light, and thus offers extraordinary sensitivity in autofluorescence-rich *in vivo* media. In recent years, non-enzymatic peroxalate-based CL (POCL) has been applied to *in vivo* imaging of local inflammation. Hydrogen peroxide (H_2O_2), abnormally overproduced in the progress of inflammatory diseases, triggers a POCL reaction, i.e., oxidation of peroxalates to form 1,2-dioxetanedione that can transfer its high energy to nearby fluorescent

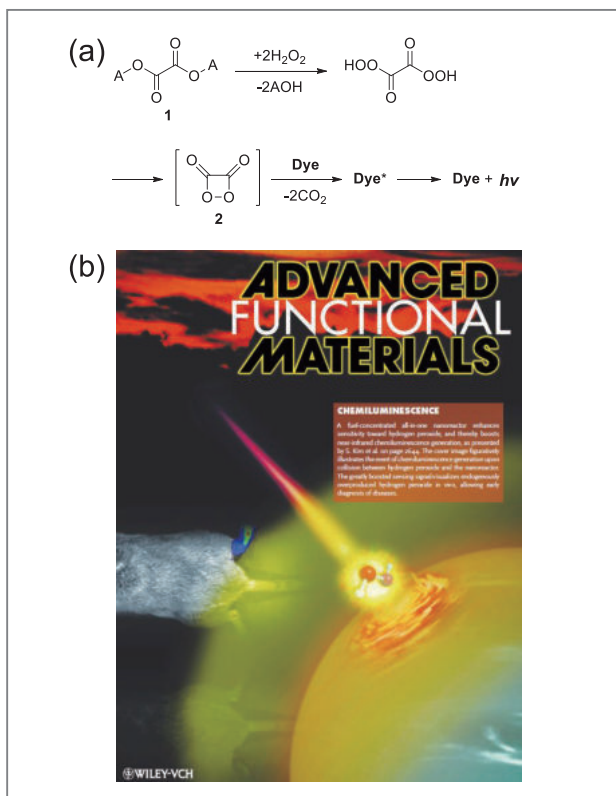


Figure 1. a) Simplified POCL reaction scheme. 1: peroxalate. 2: 1,2-dioxetanedione. b) Cover article in *Advanced Functional Materials* highlighting the work of our KIST research group [1].

molecules to emit CL (Figure 1a). POCL nanoprobes (nanoscale reactors loaded with peroxalates and dyes) have shown high sensitivity and selectivity toward H_2O_2 , thereby suggesting their potential for early diagnosis of inflammation. This advantageous feature has been conceptually demonstrated by direct local injection of POCL nanoprobes into inflamed tissues; however, it remains a challenge to make the probes operable by systemic delivery, which would allow for more advanced diagnostic imaging by sensitively discovering and locating inflammations in the body with background-free CL signals.

As demonstrated in our previous report, colloidal POCL nanoprobes filled with a highly reactive peroxalate (bis[3,4,6-trichloro-2-(pentyloxycarbonyl)phenyl]oxalate, CPPO) and a typical NIR-emissive cyanine dye (Cy5)

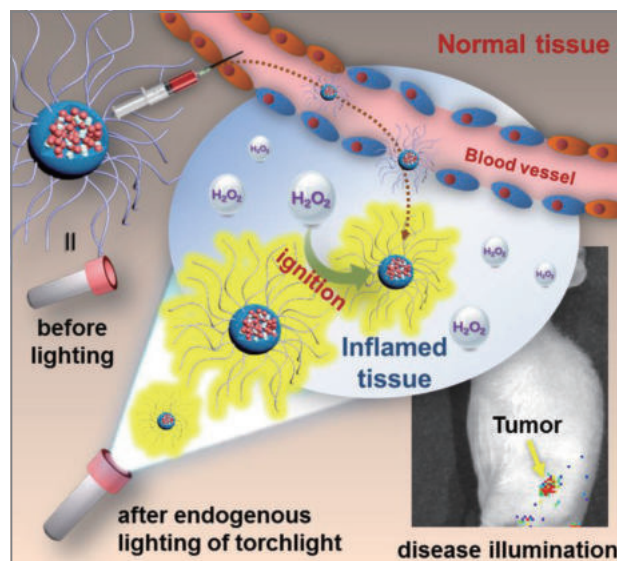


Figure 2. Graphical abstract representing how BioNT works *in vivo* for systemic targeting and imaging of diseases.

could detect H_2O_2 as low as $\sim 5 \times 10^{-8}$ M *in vivo* (Figure 1b) [1]. A simple way to enhance detection capability was to utilize a special dye that emits solid-state fluorescence (SSF) without typical self-quenching of fluorescence. By concentrating the POCL nanoreactor with a SSF dye in place of a dilute Cy5 dopant, the CL intensity could be simply enhanced by an order of magnitude [2]. An intriguing aspect of the SSF-induced enhanced POCL (SSF-CL) is that the achieved detection limit is far below the normal physiological level of H_2O_2 (10^{-7} M). The resulting ultrahigh sensitivity may render the following scenario plausible: 1) upon systemic administration of the nanoprobes, the SSF-CL reaction can be triggered even by the normal *in vivo* level of H_2O_2 to emit an endogenously lighted luminescence glow; and 2) if the lighted nanoprobes are sustained long enough in the circulatory system, they can illuminate the whole body and then accumulate in pathological tissues where the CL intensity reflects the level of H_2O_2 abnormally overproduced by inflammation (Figure 2).

In the research described here, we demonstrate that such a scenario is feasible with an ultrafine POCL nanoreactor (~ 15 nm in size) that is capable of strong

low-energy SSF-CL emission (Figure 3). This nanoreactor is called a “bio-lighted luminescent nanotorch (BioNT)” because SSF-CL is lighted and sustained by the reaction between nanoscopically confined fuels (peroxalates) and endogenous biological H_2O_2 and then extinguished after complete fuel consumption, similar to torchlight. In order for BioNT to accurately reflect the diagnostic H_2O_2 level, its CL torchlight needs to persist even after circulating in the blood and accumulating at a disease site. To control the duration of torchlight so that it circulates long enough to target and image a disease, we devised a simple way of tailoring the luminescence kinetics by loading the nanotorch with antioxidants. In this article we present a proof-of-concept study on the self-delivery and luminescence kinetics control of blood-circulating BioNT and its on-demand uses for diagnostic imaging of diseases by systemic injection.

Results and Discussion

BioNT and its constituents are sketched in Figure 3a. As an emitting component for POCL, we employed an anthracene-cored hydrophobic dye (BDSA) whose chromophoric unit had been reported to show strong reddish SSF in the nanoaggregated forms. The average diameter and the number-weighted hydrodynamic size of BioNT were estimated as 15.8 ± 4.8 nm and 15.4 ± 0.5 nm, respectively (Figure 3b), manifesting that the colloidal size was suitably engineered to be small enough for long systemic circulation. Upon addition of H_2O_2 to the BioNT dispersion, reddish luminescence was generated that was broad and significantly covered the tissue-penetrating near-infrared (NIR) region (>650 nm), making it advantageous for *in vivo* imaging (Figure 3c). The CL output from BioNT was so strong as to be seen vividly by the naked eye under room light (see Figure 3c inset), suggesting that the aggregated BDSA and CPPO are a good pair for the POCL reaction.

The luminescence characteristics of SSF-based BioNT

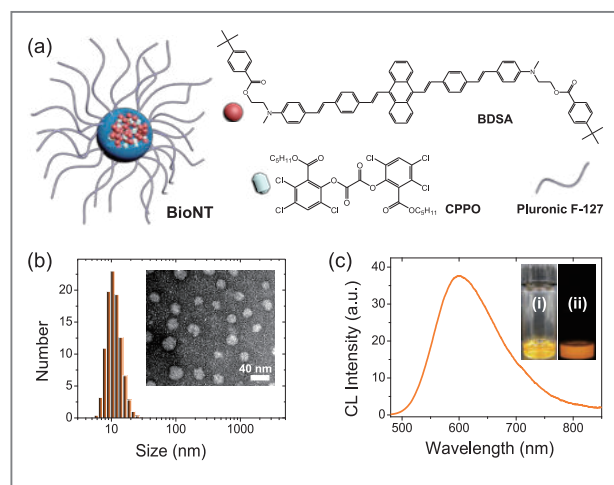


Figure 3. a) Schematic representation of BioNT. (b) Number-averaged hydrodynamic size distribution and TEM image (inset) of BioNT. (c) CL spectrum of water-dispersed BioNT, taken at 10 s after addition of H_2O_2 (0.17 M). The inset shows photographs of the generated CL under room light (i) and in the dark (ii).

were evaluated in comparison to a typical dye (Cy5)-doped POCL nanoprobe (FPOC). Upon subcutaneous injection into a normal mouse, both BioNT and FPOC displayed bio-lighted CL (lighted by endogenous H_2O_2 *in vivo*). The total signal output of BioNT over time was 11-fold intensified over that of FPOC, confirming that the SSF-based nanotorch can be lighted and emit enhanced luminescence even by a normal *in vivo* level of H_2O_2 . More importantly, immediately after intravenous injection of BioNT into a normal mouse, a bright CL glow was seen throughout the whole body with no significant localization (Figure 4a), implying that it could circulate well through the bloodstream due to the small colloidal size and the antifouling surface coat. All these observations confirm that BioNT satisfies the suggested requirements for the success of systemically targeted CL imaging, i.e., ultrahigh H_2O_2 sensitivity and facile blood circulation.

H_2O_2 -overproducing inflammatory diseases, such as atherosclerosis, cancer, arthritis or ischemia, are known to develop defective leaky vasculature. Such pathological tissues can be passively targeted with nanomaterials capable of long blood circulation. Systemic self-delivery

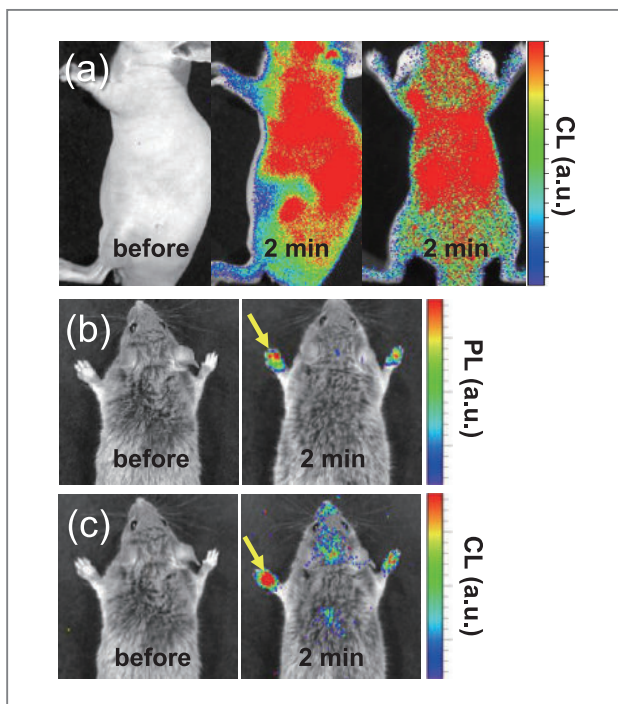


Figure 4. a) CL images (side and dorsal views) of a normal mouse before and 2 min after the tail vein injection of BioNT ($n = 4$). (b, c) Systemic inflammation model of rheumatoid arthritis (RA) imaged with PL (b) and CL (c) signals. The more inflamed foot is indicated with arrows.

of the H_2O_2 -imaging BioNT would provide an opportunity for the noninvasive detection and diagnosis of systemic inflammatory disorders in the body. For example, rheumatoid arthritis (RA) that is a chronic autoimmune disorder and occurs systemically, could be successfully located and visualized in a mouse model with diagnostic CL signals from the intravenously injected BioNT. In visual examination of the RA model, only the left forepaw seemed inflamed with apparent arthritic symptoms of redness and swelling. Upon intravenous injection of BioNT, however, its PL signals were observed in both left and right forepaws as early as 2 min post-injection and shown to accumulate gradually with time (Figure 4b). The PL signal accumulation is attributed to the population enrichment of BioNT by self-delivery, suggesting that both forepaws were in an arthritic condition with leaky blood vessels. The left forepaw that was apparently

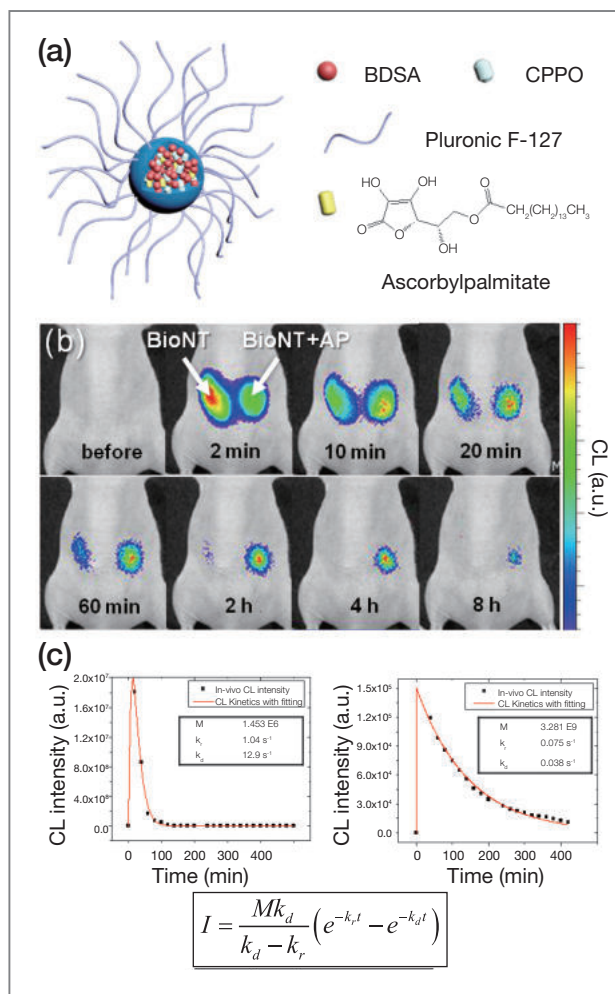


Figure 5. a) Schematic representation of ascorbyl palmitate (AP) coembedded BioNT (BioNT+AP). (b) Temporal intensity traces of endogenously generated CL from BioNT and antioxidant-loaded one (BioNT+AP) ($n = 4$). (c) *In vivo* CL kinetic profiles of BioNT (left) and BioNT+AP (right). The kinetic parameters were determined with nonlinear fitting according to the given equation, where I is the CL intensity. kr and kd are the rate constants for rising and decay, respectively.

more inflamed showed a higher PL intensity than the right which presented no apparent sign of inflammation ($I_{\text{PL, left}}/I_{\text{PL, right}} \sim 1.2$ at 2 min). This manifests that a larger number of nanoprobe accumulated in the left due to the more developed pathological condition. Importantly, such a diagnostic signal contrast was more enhanced by CL modality. As shown in Figure 4c, CL imaging of the same mouse showed a more clear-cut imaging contrast

between the developed and early inflammations ($I_{\text{CL, left}}/I_{\text{CL, right}} \sim 2.1$ at 2 min). This validates that the CL intensity reflects not only the self-delivered nanoprobe population but also molecular information on the overproduced inflammatory H_2O_2 level in the delivered tissue. The combined performance of systemic self-delivery and H_2O_2 -responsive molecular imaging well represents the potential merit of SSF-enhanced luminescent BioNT for diagnostic functional imaging.

Passive disease targeting may demand prolonged blood circulation that can be longer than the CL lifetime of BioNT. For instance, it was found that tumor targeting by intravenously injected BioNT took at least 3 hours, at which point the CPPO fuel was almost consumed and the inflammatory H_2O_2 level of the tumor was hard to image with the expiring CL torchlight. Such a limitation could be overcome by prolonging the glowing duration of the short-lived POCL emission. To tailor the decay kinetics, BioNT was further loaded with a hydrophobic derivative of ascorbic acid (ascobyl palmitate) that is an antioxidant known to break oxidative H_2O_2 into H_2O (Figure 5a). To see the antioxidant effect on the kinetics, BioNT particles with and without co-embedded ascobyl palmitate (AP) were subcutaneously injected and their bio-lighted CL signals were compared *in vivo* with time. As shown in Figure 5b, the luminescence from antioxidant-free pristine BioNT was initially brighter but faded faster than that from antioxidant-loaded BioNT (BioNT+AP). These *in vivo* luminescing behaviors were well expressed by following a simple pseudo-first-order kinetic profile (Figure 5c). BioNT+AP presented the rise and decay kinetic rates ($k_r = 7.8 \times 10^{-3} \text{ s}^{-1}$ and $k_d = 1.1 \times 10^{-4} \text{ s}^{-1}$) that were 65-fold slowed down compared to those of the antioxidant-free one ($k_r = 7.6 \times 10^{-4} \text{ s}^{-1}$ and $k_d = 7.2 \times 10^{-3} \text{ s}^{-1}$). As a result, antioxidant-loaded BioNT sustained imagable CL signaling *in vivo* even at 8 hours post-injection, as opposed to the short-lived antioxidant-free probe signal that became negligible as early as 2 hours after injection (Figure 5b).

After systemic accumulation of the probes, the tumor

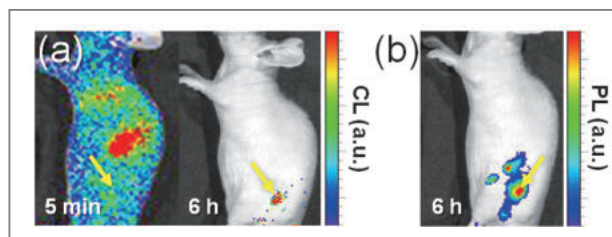


Figure 6. (a) CL images showing the temporal signal distribution of intravenously injected BioNT+AP into a mouse bearing a small SCC7 tumor ($\sim 45 \text{ mm}^3$), taken at the indicated time points after tail vein injection ($n = 4$). (b) PL image of the same mouse in (a), taken at 6 h postinjection ($n = 4$). Yellow arrows indicate the tumor location.

could barely be imaged with the short-lived CL from antioxidant-free pristine BioNT, whereas in the case of BioNT+AP, the H_2O_2 -overproducing tumoral condition was clearly visualized at 6 hours post-injection with the still-glowing torchlight (Figure 6a). Importantly, it should be noted that PL imaging yielded a number of off-target signals from other parts of the body (e.g., lymph nodes) due to less disease-specific tissue accumulation of the probes (Figure 6b). Such nonspecific false signals are typical of a PL modality that merely depends on the biodistribution of PL probes, which compromises the accuracy of image-based diagnosis. In sharp contrast, CL imaging at the same time point visualized only the location of an invisible early-stage tumor smaller than 50 mm^3 exclusively because tumoral tissue has a higher level of H_2O_2 than other nonspecifically accumulated parts of the body (Figure 6a). This result demonstrates the advantage of the long-lasting luminescent torchlight of BioNT that allows for precise diagnostic signaling with dual selectivity, i.e., selective probe enrichment in the pathological tissue by self-delivery and selective generation of prolonged SSF-CL by the pathological tissue-specific level of H_2O_2 .

Conclusion

We have developed a biologically lightable CL

nanotorch (BioNT) that is useful for systemically targeted imaging and precise identification of inflamed tissues *in vivo*. The construction of BioNT is based on the physical integration of reactants into a self-assembled nanoreactor system wherein the SSF-CL reaction is triggered even by a normal *in vivo* level of H_2O_2 . It has been demonstrated that the intensity of the concomitantly-generated CL torchlight well reflected the inflammatory H_2O_2 level in the background-rich biological tissues. Besides sensitive visualization of H_2O_2 , BioNT was shown to be capable of systemic self-delivery to the pathological tissues and elaborate control of luminescence kinetics. The combined merits allowed for systemically targeted diagnostic imaging with selectively enhanced dual contrasts between normal and inflamed tissues in terms of probe population and H_2O_2 concentration. Taking into account the low *in vivo* toxicity shown in our experiments, we believe that our BioNT probe holds great promise for diagnostic biomedical uses.

Note

This article and images are drawn from “Bio-Lighted Nanotorch Capable of Systemic Self-Delivery and Diagnostic Imaging” in *ACS Nano*, Vol.9, pp. 9906~9911.

References

- [1] Lim C-K, Lee Y-D, Na J, Oh JM, Her S, Kim K, Choi K, Kim S, Kwon IC. *Adv. Funct. Mater.* 2010; 20: 2644-2648.
- [2] Lee Y-D, Lim C-K, Singh A, Koh J, Kim J, Kwon IC, Kim S. *ACS Nano* 2012; 6: 6759-6766.



Feature Articles

Design of a Platform Technology for Systemic Delivery of siRNA to Tumors Using Rolling Circle Transcription



Mi Hue JANG

Center for Theragnosis
Biomedical Research Institute
mihue@kist.re.kr

Introduction

RNA interference (RNAi) is an endogenous regulatory pathway that is triggered by short interfering RNA (siRNA) or microRNA. Through the activated RNAi, siRNA can silence the expression of any genes with high efficiency [1]. Most notably, RNAi is a promising tool to suppress the expression of specific genes associated with certain human diseases such as cancers, viral infections and genetic disorders [2]. The approach that utilizes siRNA as a potential drug has attracted great attention, but there are still critical issues to be addressed before it can be used for therapeutic applications. For example, naked siRNA is rapidly cleared as it circulates through the body due to its low molecular weight and enzymatic degradation [3]. Also, siRNA has no functional moiety targeted to sites of interest and its negative charge leads to poor cellular uptake owing to the electrostatic repulsion between siRNA and cell membranes [3-5]. Therefore, an efficient delivery carrier for exogenous siRNA is a prerequisite for effective clinical applications.

One of the methods for RNA synthesis, enzymatic RNA polymerization via rolling circle transcription (RCT), has resulted in an effective RNA synthetic method for multimeric siRNA, and when rationally designed, the polymerized RNA self-assembles into microsponges 2 μm in diameter [6]. However, without the aid of a polycationic reagent such as PEI, these RNA microspunge-like particles show little cellular uptake in the cancer

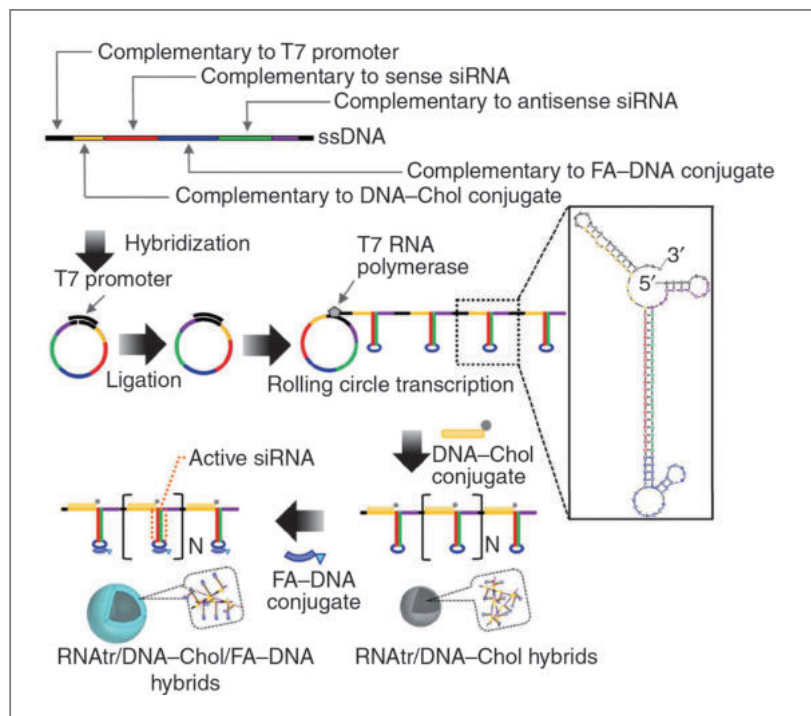


Figure 1. RNA transcripts enzymatically polymerized by rolling circle transcription are composed of multiple tandem copies of RNA hairpins containing sense and antisense sequences of target siRNA duplex. Through RNA/DNA base pairing, DNA-Chol conjugates are hybridized with the RNA transcripts, forming the amphiphilic RNAtr/DNA-Chol hybrids that can self-assemble into highly condensed nanoparticles. Sequential hybridization of FA-DNA conjugates with RNAtr/DNA-Chol nanoparticles results in RNAtr/DNA-Chol/FA-DNA hybrids with condensed nanostructures on which folates direct outwards. The box shows the simulated hairpin structure of a single repeated unit of RNA transcripts.

cell line due to their large size and high negative charge. Nonetheless, the enzymatic RCT is noteworthy for its ability to generate multiple copies of RNA polymers at low cost when compared to chemical synthesis of siRNA.

To systemically deliver siRNA in a tumor-specific manner while achieving high cargo loading, our research group in the Center for Theragagnosis at KIST has developed a method for the synthesis of RNA/DNA hybrids that self-assemble into nanoparticles without the aid of polycationic agents. The polymerized RNAs that contain multiple tandem copies of hairpins via rolling circle transcription are sequentially hybridized with DNA-cholesterol and folate-DNA conjugates through Watson-Crick base pairing, yielding self-assembled RNA transcripts/DNA-cholesterol/folate-DNA nanoparticles referred to as RNA transcripts nanoparticles or RNAtr NPs. RNAtr NPs play dual roles as both RNAi drug and carrier in our current studies; RNAtr NPs protect siRNA against nuclease attack and polyanion interference during transport to cytoplasm while generating siRNA with cytoplasmic Dicer enzymes after transfection. Thus, these

RNAtr NPs have great potential as a platform technology for siRNA therapeutics, including anticancer drugs.

Experimental results

To generate RNAtr NPs, we designed a linear ssDNA template to be complementary to each sequence of T7 promoter primer, sense anti-RFP siRNA, antisense anti-RFP siRNA, DNA-cholesterol (DNA-Chol) conjugate and folate-DNA (FA-DNA) conjugate, as shown in **Figure 1**. The linear ssDNA, of which both ends are complementary to T7 promoter, was annealed with T7 promoter primer, yielding circular DNA with a nick. After DNA ligase connected the nicked sequence, T7 RNA polymerase generated the polymerized RNA transcripts (i.e., RNAtr) from the closed circular DNA template via RCT.

Next, RNA transcripts were hybridized with DNA-Chol conjugates for self-assembly in an aqueous solution because cholesterol molecules become tightly packed

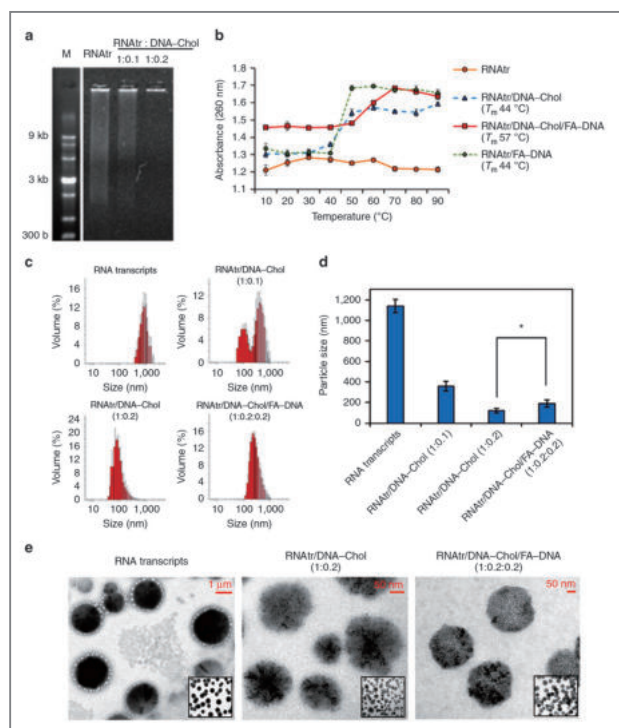


Figure 2. Characterization of RNA/DNA hybrids. (a) Gel retardation assay of RNA transcripts (RNAt) and RNAt/DNA-Chol hybrids at the indicated weight ratio. Nucleic acids were visible under ultraviolet irradiation after SYBR gold staining. (b) RNA/DNA thermal denaturation curves for RNA transcripts (RNAt), RNAt/DNA-Chol hybrids, RNAt/FA-DNA hybrids and RNAt NPs. T_m represents a transition from a RNA/DNA duplex to two strands. As temperature increased, each absorbance at 260nm was plotted. (c,d) Size distribution profiles and average size of RNA transcripts, RNAt/DNA-Chol hybrids, and RNAt/DNA-Chol/FA-DNA hybrids at the indicated weight ratio. (e) Transmission electron microscopy images showing size and shape of particles. Insets show low-magnification images of particles.

in a limited space due to hydrophobic interactions [7]. The smeared bands observed on the gel electrophoresis demonstrated that the polymerized RNA transcripts had a wide range of molecular weights, whereas the partially or fully hybridized RNAt/DNA-Chol showed different electrophoretic mobilities due to the self-assembled structures (Figure 2a). We examined the thermal stability of RNA/DNA hybrids. During thermal denaturation, RNAt/DNA-Chol and RNAt/FA-DNA hybrids had a melting temperature (T_m) at 44°C, corresponding to a transition from an RNA/DNA duplex to two single

strands (Figure 2b). When measured by dynamic light scattering, RNA transcripts had micro-sized hydrodynamic diameters ranging from 1.07 μm to 1.20 μm , but hybridization of RNA transcripts with DNA-Chol conjugates (1:0.2, w/w) significantly decreased their particle size to 119.3 ± 21.8 nm (Figures 2c and 2d). The final product, RNAt/DNA-Chol/FA-DNA hybrids (1:0.2:0.2, w/w/w), still showed nano-sized particle sizes (190.1 ± 37.2 nm). TEM images also showed that RNAt/DNA-Chol/FA-DNA hybrids, whose shapes were spherical, were significantly smaller than RNA transcripts and thus formed nano-sized particles (RNAt NPs) (Figure 2e).

To examine folate receptor-specific cellular uptake, the FAM-labeled RNAt NPs were transfected to FR-positive SKOV3 ovarian cancer cells and FR-negative A549 lung adenocarcinoma cells [8, 9]. At 3 h post treatment, the fluorescence microscopic images exhibited numerous punctate spots corresponding to RNAt NPs within the SKOV3 cells, whereas there was little or no FAM signal within the A549 cells due to lack of folate receptor (Figure 3a). Also, the flow cytometry showed that RNAt NPs had about an 80% cellular uptake efficiency in the SKOV3 cells 3 h post treatment, but were not transfected to the A549 cells (Figure 3b). Once the folate receptors present in SKOV3 cells were saturated with their ligands, the uptake efficiency of RNAt NPs decreased to 40%. On the other hand, RNA transcripts were not transfected to SKOV3 cells, possibly due to their strong negative charge and lack of folate.

The *in vitro* gene silencing of RNAt NPs was examined by measuring RFP signals in RFP-expressing SKOV3 cells after transfection. The fluorescence microscopic images of RNAt NPs-treated SKOV3-RFP cells showed that the RFP signals significantly decreased 48 h post treatment, whereas the control cells retained intense RFP signals (Figure 4a). The flow cytometry also demonstrated that the RFP signals of RNAt NPs-treated cells decreased to 48% compared with those of the control cells. The western blot consistently

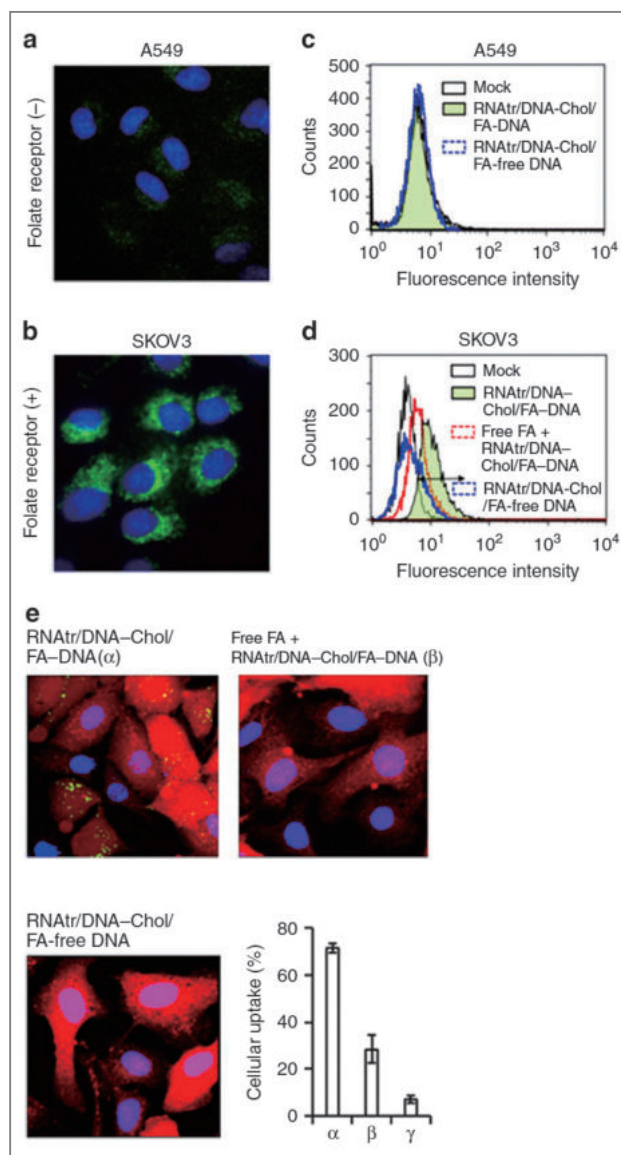


Figure 3. Cellular binding and uptake of RNAtr NPs. (a,b) Folate receptor-specific cell binding of RNAtr NPs in folate receptor-negative A549 lung adenocarcinoma cells and folate receptor-positive SKOV3 ovarian cancer cells. The fluorescence images were obtained by a fluorescence microscope with a CCD camera. Green and blue signals represent the fluorescence FAM-labelled RNAtr NPs and 4,6-diamidino-2-phenylindole (DAPI) dyes, respectively. (c,d) Flow cytometry studies of RNAtr NPs and folate-free RNAtr NPs. (e) Intracellular uptake studies using confocal microscopic images. For clarity, the FAM-labelled RNAtr NPs and FAM-labelled folate-free RNAtr NPs were treated to RFP-expressing SKOV3 (SKOV3-RFP) cells. Red, green and blue signals represent the fluorescence RFP, FAM-labelled RNAtr NPs and DAPI dyes, respectively.

showed that the RFP expression decreased to 55% 48 h post treatment (Figures 4b and 4c). Noticeably, RNA transcripts barely suppressed RFP expression in SKOV3-RFP cells because they could not be transfected to the cells. When the amounts of RFP mRNA remaining in RNAtr NPs-treated cells were measured by quantitative reverse transcription PCR (qRT-PCR), they significantly decreased to 25% 48 h post treatment (Figure 4d). Next, we compared the gene silencing efficiency of RNAtr NPs with that of Lipofectamine. qRT-PCR analysis, measured 48 h post treatment, demonstrated that RNAtr NPs had better silencing efficiency than monomeric siRNA/Lipofectamine complexes, and even at a low concentration of 1.93 $\mu\text{g}/\text{mL}$ (equivalent to 20 nM siRNA), they significantly decreased the amount of RFP mRNA (Figure 4e).

To verify *in vivo* tumor-targeting ability, Cy5-labeled RNAtr NPs (50 μg) were systemically administered via tail vein into mice bearing SKOV3 xenograft tumors, and their biodistribution was monitored by measuring NIRF images (Figures 5a and 5b). At 1 h post injection, a strong NIRF signal observed in tumors clearly distinguished tumor tissues from other organs. The NIRF signal in tumors reached its maximum intensity 2 h post injection and persisted for at least 48 h. *Ex vivo* fluorescence images obtained 48 h post injection also corresponded well with the biodistribution images and showed that RNAtr NPs accumulated primarily in tumors, compared with other dissected organs (Figure 5c).

The *in vivo* gene silencing of RNAtr NPs was evaluated by RFP fluorescence images in the SKOV3-RFP xenograft tumors after systemic administration. When the fluorescence signals of RFP-expressing tumors were strongly detected, RNAtr NPs were intravenously injected into a mouse once (day 0; 50 μg) or at an interval of one day (days 0, 1; 25 $\mu\text{g}/\text{injection}$), and then RFP signals at the tumor sites were measured (Figures 5d and 5e). In two days post injection, the RFP signals decreased to 45% and 80% in the RNAtr NPs-double-injected and RNAtr NPs-single-injected mice, respectively, when

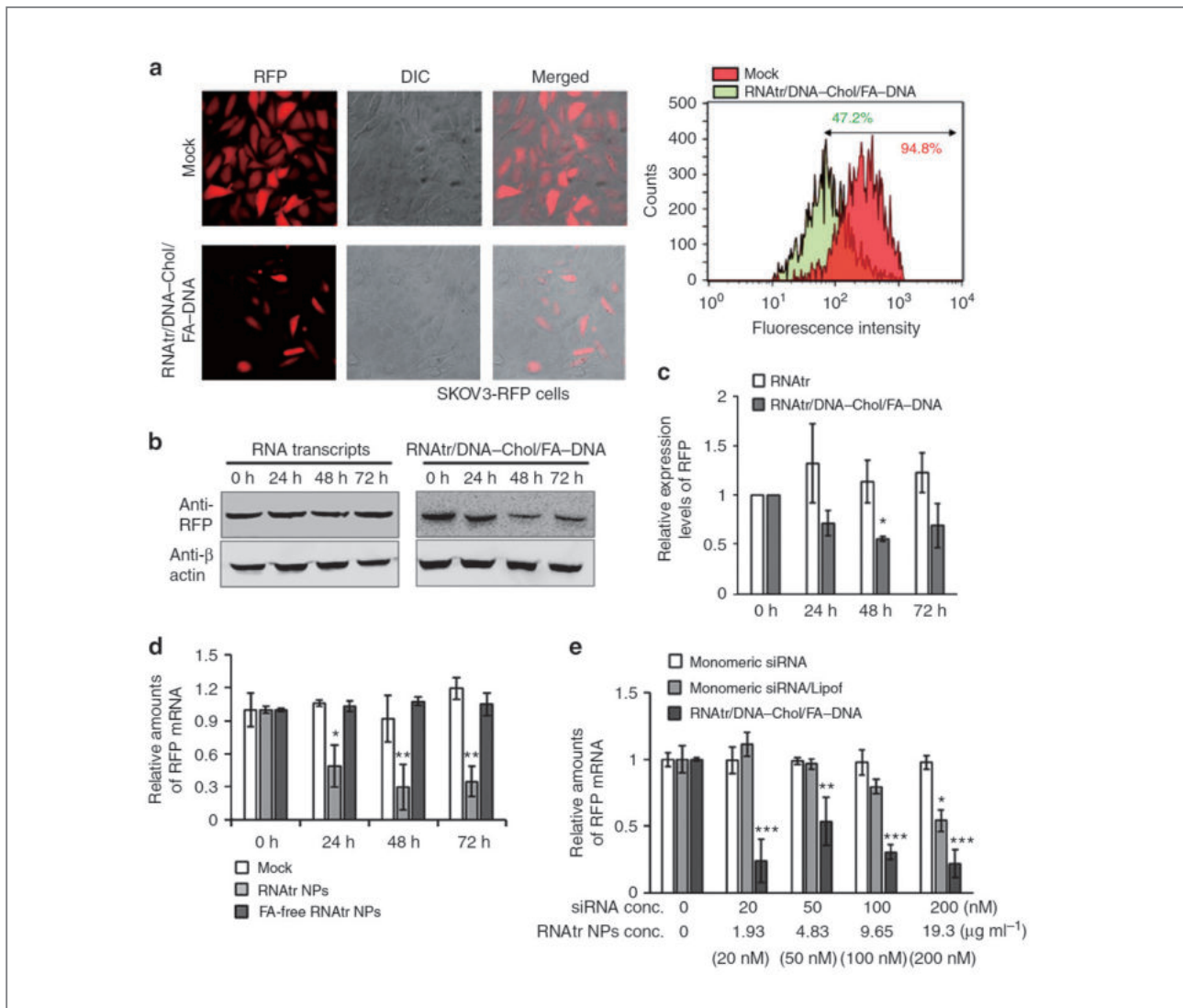


Figure 4. Silencing of target RFP gene in RFP-expressing SKOV3 cells. (a) Fluorescence microscopic images and flow cytometry analysis of RNAtr NPs-treated SKOV3-RFP cells. RNAtr nanoparticles were added to the cell culture media at the final concentration of 10 mg/ml (equivalent to 100nM siRNA) and their gene silencing effect was measured 48 h post treatment. (b,c) Suppressed RFP expression measured by western blotting. The amount of RFP protein was measured in SKOV3-RFP cells treated with RNA transcripts or RNAtr nanoparticles at the final concentration of 10 mg/ml for the indicated period. Relative expression levels of RFP were plotted versus incubation time (c). (d) RFP mRNA measured by qRT-PCR. After treating SKOV3-RFP cells with either RNAtr NPs or folate-free RNAtr NPs at the final concentration of 10 mg/ml for the indicated periods, amounts of mRNA present in each sample were measured by qRT-PCR. (e) Silencing effect comparison using qRT-PCR. Suppressed RFP mRNA after treatment with monomeric anti-RFP siRNA, monomeric anti-RFP siRNA/Lipofectamine complexes and RNAtr nanoparticles was measured 48 h post treatment by qRT-PCR.

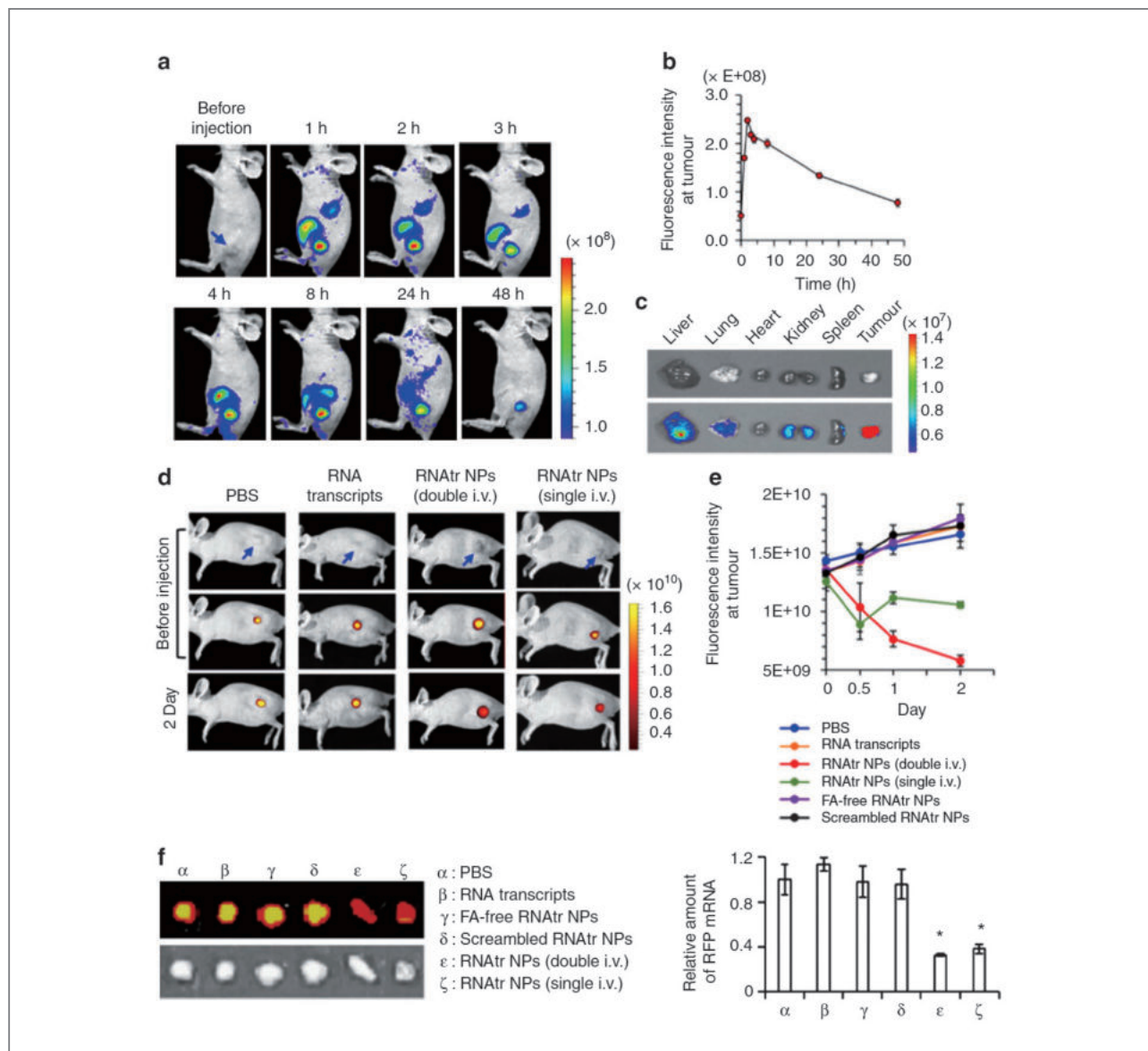


Figure 5. Biodistribution of RNAtR NPs and their RFP gene silencing in tumor model. (a,b) Whole-body NIRF imaging of SKOV3 tumor-bearing mice after intravenous injection of Cy5-labelled RNAtR NPs via tail veins. Blue arrow indicates the location of tumor xenograft. Fluorescence intensity of Cy5-labelled RNAtR NPs which accumulated at tumor sites was measured at the indicated time point (b). (c) *Ex vivo* NIRF images of the dissected organs and tumor tissues 48 h post injection. (d) Noninvasive NIRF imaging of *in vivo* RFP gene silencing from RNAtR NP-injected mice. Blue arrow represents site of tumor. (e) RFP fluorescence intensities at tumor sites measured before or after systemic administration were plotted versus day. (f) *Ex vivo* NIRF images of the dissected tumors from PBS-, RNA transcripts-, folate-free RNAtR NP-, scrambled RNAtR NP-, RNAtR NPs double-injected or RNAtR NPs single-injected mice. The tumors were excised two days post injection. Amount of RFP mRNA present in the dissected tumors was measured by qRT-PCR (right).

compared with those in the PBS-injected mice. However, the RNA transcripts-injected mice revealed increased rather than decreased RFP signals at the tumors, as shown in the PBS-injected mice. *Ex vivo* RFP signals of the tumors at two days post injection, as well as the levels of RFP mRNA at the tumors, corresponded well with the *in vivo* real-time fluorescence images (Figure 5f).

Conclusion

Our group has demonstrated that our design of RNATR NPs facilitates precise control over condensation of RNA polymers and the locations of folate ligands through a combination of RCT and Watson-Crick base pairing. It is particularly notable that RNATR NPs showed robust RFP gene silencing effects in tumor sites when intravenously injected into SKOV3-RFP tumor xenograft mice. Therefore, this platform-technology provides a novel method to systemically deliver siRNA to tumor sites and can be readily extended to therapeutic siRNA applications for broad cancer treatments.

Note

This article and its images are drawn from “Design of a platform technology for systemic delivery of siRNA to tumours using rolling circle transcription” in *Nature Communications*, 6:7930, 2015.

References

- [1] Pecot CV, Calin GA, Coleman RL, Lopez-Berestein G, Sood AK. *Nature Reviews Cancer* 2011; 11 (1): 59-67.
- [2] Miller VM, Xia H, Marrs GL, Gouvion CM, Lee G, Davidson BL, Paulson HL. *Proceedings of the National Academy of Sciences of the United States of America* 2003; 100 (12): 7195-200.
- [3] Wang J, Lu Z, Wientjes MG, Au JL. *The AAPS Journal* 2010; 12 (4): 492-503.
- [4] Dykxhoorn DM, Palliser D, Lieberman J. *Gene Therapy* 2006; 13 (6): 541-52.
- [5] Cheng Z, Al Zaki A, Hui JZ, Muzykantov VR, Tsourkas A. *Science* 2012; 338 (6109): 903-10.
- [6] Lee JB, Hong J, Bonner DK, Poon Z, Hammond PT. *Nature Materials* 2012; 11 (4): 316-22.
- [7] Daly TA, Wang M, Regen SL. *Langmuir: The ACS Journal of Surfaces and Colloids* 2011; 27 (6): 2159-61.
- [8] Jang B, Park S, Kang SH, Kim JK, Kim SK, Kim IH, Choi Y. *Quantitative Imaging in Medicine and Surgery* 2012; 2 (1): 1-11.
- [9] Hu X, Liu S, Huang Y, Chen X, Jing X. *Biomacromolecules* 2010; 11 (8): 2094-102.



- Bio / Medical
- Materials / Systems
- Energy / Environment
- Research Highlights
- KIST News
- A Sign of the Times
- Interview

Technical Review

Neuromorphic Engineering Based on a Spiking Neural Network



Doo Seok JEONG

Center for Electronic Materials
Post-Silicon Semiconductor Institute
dsjeong@kist.re.kr



Joon Yeon CHANG

Post-Silicon Semiconductor Institute
presto@kist.re.kr

Introduction

An important trend in current technology development involves reducing the time human beings spend working. “Work” in this sense applies not just to occupational activity, but to all activities within the human domain. Decision-making is one such example. It is a frequent requirement of daily life yet cannot be done by anything non-human. If something *could* accomplish this task, a person’s workload could be significantly reduced. This is why the concept of artificial intelligence (AI) has been attracting such attention, and methodologies for AI, such as deep learning [1], have been capturing the popular imagination. It should be noted that AI in this sense refers to decision-making ability on the basis of training or learning with training sets. Inspired by brains and their information processing pathways, an artificial neural network (ANN) underlies deep learning. An ANN, consisting of artificial neurons and synapses, takes after the brain with regard to its structure; however, the detailed behavior of an ANN compared to a brain is very different. Binary states are given to each artificial neuron in response to the sum of the inputs plus bias; the neuron is often expressed by the Heaviside step function or sigmoid function [1]. These artificial neuron models differ significantly from a biological neuron that represents analog information by means of spiking dynamics [2, 3].

A spiking neural network (SNN) is another class of network for AI. It is distinguished from an ANN by its neural representation on spiking

(dynamic) grounds [4-6]. Spiking neurons fire spikes when the membrane potential crosses a threshold for spiking. The membrane potential evolves in due course with incident synaptic current. In addition, activity that defines how often spiking occurs represents analog-type information in the SNN. The spiking neuron's real-time response to synaptic current makes it suitable for real-time information representation, which enables interaction with physical environments [4]. Given the spiking neuron's dynamic response, the physiological spatiotemporal learning rules, e.g., the Hebbian learning rules, may be directly applied to training an SNN. In this regard, an SNN shares more similarities with a biological neural network than an ANN does.

Both ANNs and SNNs are often developed on computers by emulation methods, popularly referred to as *in silico* networks. In supervised learning, *in silico* synapses are trained to minimize a disparity between the calculated and desired outputs (cost function) [1, 7]. The cost function minimization requires mathematical algorithms such as a gradient descent method and its variations. The calculation efficiency can be improved significantly by making use of a more efficient algorithm, such as a stochastic gradient descent method [8]; however, the calculation is still costly when associated with a large number of synapses, hidden layers, and training sets [1]. Calculating an SNN is even more daunting given the requirement of spiking and synaptic weight change calculations in a specified period of time. These calculations consume extensive computational resources and require long computation times, thus rendering the system essentially incapable of real-time interaction with environments.

A possible workaround solution to these inherent complexities is to implement such SNNs in physics-based hardware without the need for calculation of an *in silico* SNN. Building a hardware SNN using proper "unit blocks" is of vital importance since one of the most important building blocks is a spiking neuron. To date, several prototypical neuron models have been proposed,

mostly on the basis of integrate-and-fire behavior, and include the Axon-Hillock neuron [9, 10], neuristor-based leaky integrate-and-fire (LIF) neuron [11, 12], conductance-based neuron [13, 14], and Izhikevich neuron [15, 16]. Each model exhibits neuronal behaviors to differing degrees. What is most essential, however, is that they feature neuronal behaviors that play key roles in neuronal representation, such as LIF behavior, gain function, and autocorrelated (i.e., random) neuronal noise [12]. The review presented here focuses on a discussion of spiking neuron and SNN-compatible synapse circuits.

Spiking neuron circuit

To obtain real-time interaction with physical environments, it is desirable that a hardware neuron spike at a rate similar to that of a biological neuron (ca. <100 Hz). Given that each spike consumes a certain amount of power, it follows that the higher the activity in a given period of time, the more power a neuron consumes. To this end, the interspike interval (ISI) between neighboring spikes in time reaches a few tens of milliseconds, which requires a comparable R-C time constant within the framework of the LIF neuron. To put it precisely, a linear low-pass filter, i.e., integrator, in the LIF neuron needs to be endowed with a cutoff frequency below the minimum activity of a biological neuron. Signal integration can be realized in different integrators, e.g., the Tau-cell (Edwards and Cauwenberghs, 2000), the subthreshold log-domain integrator (Arthur and Boahen, 2004), and a differential pair integrator (Bartolozzi and Indiveri, 2007), but in all these cases, a capacitor causes a delay in the response to an input signal so that the capacitance significantly alters the time delay, partly akin to an R-C delay in a simple R-C circuit. An overview of these integrators has been clearly presented in a paper written by Indiveri et al. in 2007.

Floating gate-based leaky integrate-and-fire neuron

The FG-based metal-oxide-semiconductor field-effect transistor (MOSFET), FG-MOSFET for short, is one of the most successfully commercialized nonvolatile memory bits in flash memory [17]. The high maturity level of flash memory technology offers great opportunities for neuromorphic engineering; in particular, FG-MOSFETs show promise as programmable synapses that work as local memories within a neuromorphic circuit [18, 19]. To date, diverse FG-MOSFET-based synapse circuits have been proposed with different levels of precision. The simplest case is a single-transistor synapse device that can maintain the programmed synaptic weight for sufficiently long time periods and implement the spike-timing-dependent plasticity protocol. FG-MOSFETs have also been employed as the core part of a synapse circuit [20]. Although synapse circuits containing FG-MOSFETs are diverse, FG-MOSFETs themselves are generally responsible for the memory of a programmed synaptic weight.

Recently, Kornijcuk et al. have proposed an LIF neuron circuit based on a floating-gate (FG) integrator as a replacement for a capacitor integrator [21]. Compared with FGs in synapse circuits, the role of an FG in this type of integrator is counterintuitive given that the FG is deliberately designed to retain the charge on the FG for a few seconds, at most. This poor charge retention

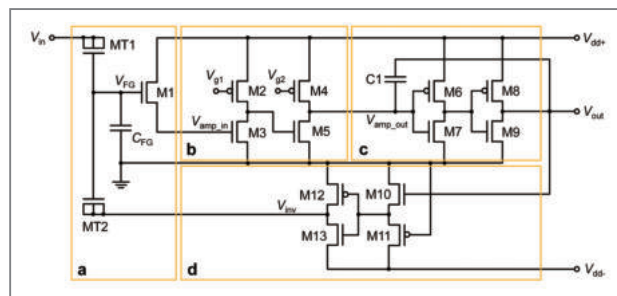


Figure 1. FGLIF neuron circuit. The circuit consists of four subcircuits: (a) FG integrator; (b) voltage amplifier; (c) voltage amplifier with positive feedback; and (d) polarity inverter.

is not acceptable in the FGs in synaptic circuits. The kinetics of filling the floating gate with charge (charging) and emptying it (discharging) resembles the charging and discharging of a capacitor. However, a significant difference lies in the mechanism for charging and discharging. Charge transfer into and out of the FG is mainly determined by area-independent properties of the tunnel barrier, e.g., barrier height and thickness. Thus, the characteristic time constant—corresponding to that in a capacitor-based integrator—can be tweaked irrespective of the area of the FG, unlike the capacitor-based integrator. As a result, the circuit has excellent potential for scalability and very low power consumption. The floating-gate-based leaky integrate-and-fire (FGLIF) neuron circuit is depicted in Figure 1. The circuit consists of 12 MOSFETs (M2–M13), a single FG transistor (M1 + C_{FG}), and a capacitor C1. The FG transistor has separate terminals MT1 and MT2 (tunnel junctions) for programming charge in the FG through quantum mechanical tunneling.

A spiking input mode realizes practical circumstances for the operation of an FGLIF neuron in an SNN. The

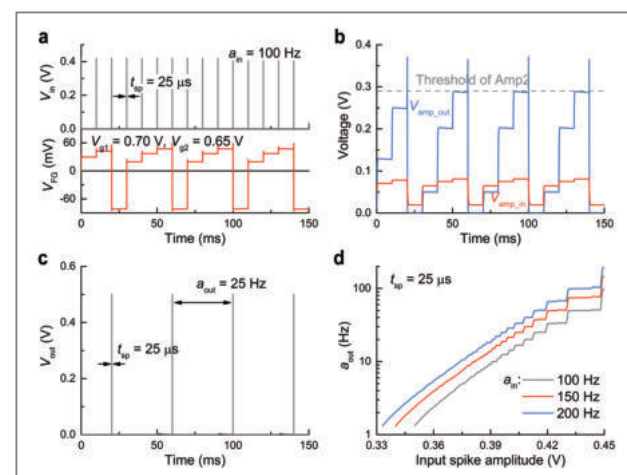


Figure 2. Spiking characteristics in spiking input mode. (a) Input signal profile ($V_{in} = 0.42$ V, $t_{sp} = 25$ μ s) (upper panel) and resulting V_{FG} evolution (bottom panel). The input activity (a_{in}) was set to 100 Hz. (b) Responses of $V_{amp,in}$ and $V_{amp,out}$ to the input spikes. (c) Output spikes ($t_{sp} = 25$ μ s, $a_{out} = 25$ Hz). (d) Neuronal gain function for three a_{in} values (100, 150, and 200 Hz).

subcircuit-wise responses to an input spike train (activity: 100 Hz; spike amplitude: 0.42 V; spike width: 25 μ s) are plotted in Figure 2. V_{amp_in} is amplified through Amp1 (Figure 2b), and a spike is elicited from V_{out} when V_{amp_out} crosses the threshold of Amp2 (Figure 2c). Likewise, the output activity differs for different spike amplitudes and activities, as shown in Figure 2d; the larger the amplitude and/or activity, the more frequently the neuron spikes. That is, when information transmission between pre- and postsynaptic neurons is invoked in an SNN, the postsynaptic FGLIF neuron is able to represent the presynaptic neuron's activity.

Relaxation oscillator-based leaky integrate-and-fire neuron

Another class of neuron circuitry within the framework of leaky integrate-and-fire has recently been proposed, one which is based on a relaxation oscillator in conjunction with a CMOS amplifier. This neuron is referred to as a relaxation oscillation-based leaky integrate-and-fire (ROLIF) neuron [22]. Figure 3 depicts the equivalent circuit of the ROLIF neuron. The input and output voltages are denoted by V_{in} and V_{out} , respectively, and V_{out} corresponds to the membrane potential of the neuron. The neuron consists of a non-ideal op-amp (grey dashed line) and PAO (orange dashed line). The op-amp enables active operation in light of gain G , where $G =$

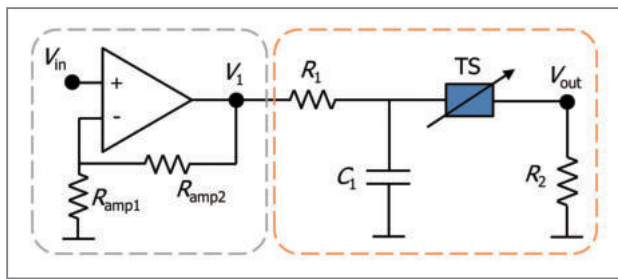


Figure 3. Equivalent circuit of a ROLIF neuron. The grey and orange boxes indicate a non-ideal op-amp and PAO encompassing the threshold switch (TS), respectively.

$1 + R_{amp2}/R_{amp1}$. Thus, attenuated spikes along *passive* synapses can be re-amplified through the op-amp.

Considering two ROLIF neurons in connection via a synapse, V_{out} of the presynaptic neuron is fed into V_{in} of the postsynaptic neuron through the synapse. However, reverse synaptic transmission should be banned inasmuch as it does not conform to the behavior of a biological chemical synapse [23].

The PAO is responsible for spiking in response to V_{in} , resulting in different spiking activities. That is, the PAO contributes to encoding the input voltage into spiking activity. Notably, the TS in the PAO exhibits switching event-driven variations in switching parameters and resulting neuronal noise.

The behavior of the ROLIF neuron was justified by synaptic transmission between a pair of neurons through a synaptic resistor R_{syn} (see Figure 4a). The presynaptic neuron is subject to a sufficiently high constant voltage

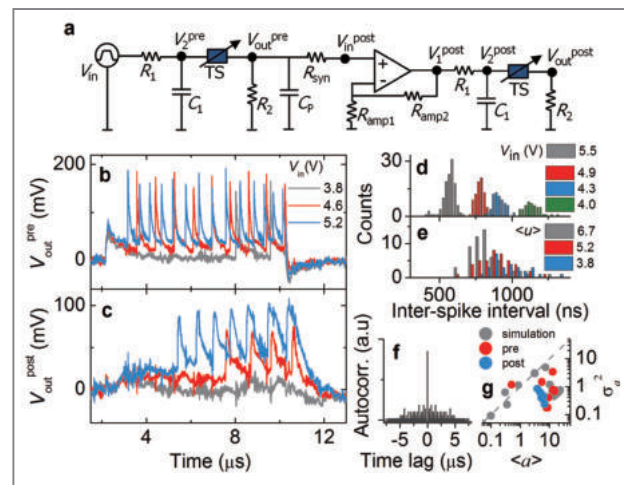


Figure 4. (a) Equivalent circuit of a pair of neurons that are connected through a synaptic resistor ($R_{syn} = 1$ k Ω and $R_{amp2} = 100$ k Ω). C_p indicates the parasitic capacitance originating from the wiring. (b) Spike bursts in presynaptic neurons at different constant voltages (3.8, 4.6, and 5.2 V) and (c) the consequent postsynaptic spike bursts. ISI distribution for the (d) presynaptic and (e) postsynaptic spike bursts. (f) Autocorrelogram of the presynaptic spikes in the burst at 5.2 V. (g) Relationship between the measured mean $\langle a \rangle$ and variance σ_a^2 of neuronal activity. The dashed line indicates a theoretical relation for a Poisson neuron.

for spiking, and the evoked spikes are translated into EPSP (V_1^{post}) for the postsynaptic neuron through the aforementioned $R_{\text{syn}}-C_{\text{in}}$ coupling. In this way, the postsynaptic neuron spikes in response to input spikes.

Three different voltages (3.8, 4.6, and 5.2 V) applied to the presynaptic neuron successfully evoked spikes, which then led the postsynaptic neuron to spike, as plotted in Figures 4b and 4c. $V_{\text{out}}^{\text{pre}}$ and $V_{\text{out}}^{\text{post}}$ were simultaneously acquired while applying a constant voltage V_{in} . Recalling that the number of spikes parameterizes neuronal activity a , such measurements are used to evaluate the activities of pre and postsynaptic neurons, u and v , respectively. The uncorrelated random variability in the threshold switching parameters is the direct cause of neuronal noise. Mapping such variability onto neuronal noise has recently been identified by theoretical means [12]. The histograms for the presynaptic neuron in Figure 4d evidence the gamma distribution of ISI, reflecting the distributional nature of the switching parameters [12]. With that said, it should be noted that such histograms do not necessarily justify the randomness of ISI variation; instead, a cross-correlation analysis on the ISI distribution provides clear evidence for randomness [2, 12]. For instance, the autocorrelogram in Figure 4f markedly visualizes no correlation within the spikes in the same burst other than self-correlation that is indicated by the peak at a time lag of zero. Unlike the presynaptic neuron, the postsynaptic neuron was directly subject to presynaptic spikes. The resulting ISI distributions of postsynaptic spiking at different mean presynaptic activities $\langle u \rangle$ are plotted in Figure 4e, which represent features akin to the presynaptic neuron.

Synapse circuit for online learning

There are two types of synapses: electrical synapse (also known as gap-junction) and chemical synapse [24]. The latter is regarded to be mainly involved in learning and memory in the hippocampus [25], while recent study suggests that electrical synapses play a key role in

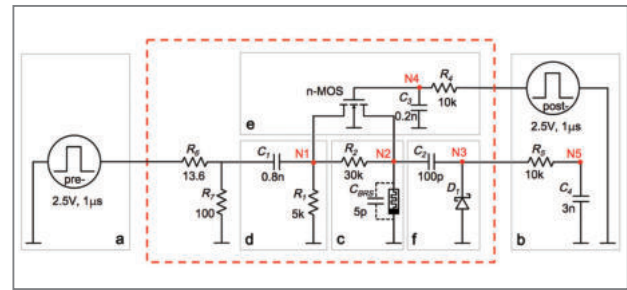


Figure 5. Electrical circuit for an artificial synapse (red dashed line) and a circuit for synaptic plasticity evaluation.

fear learning and memory [26]. Chemical synapses are plastic and involved in learning and memory. In other words, plasticity of their synaptic efficacy defines the connectivity between two associated neurons. Chemical synapses undergo such plastic change upon external electrical stimulation of their associated neurons. It should be noted that the synaptic transmission through a chemical synapse is unidirectional inasmuch as the transmission takes place by means of neurotransmitters (chemical messengers) that are released from the presynaptic neuron and arrive at receptors on the postsynaptic neuron [24]. Several plasticity-induction protocols are known, such as activity-dependent plasticity (ADP) and spike-timing-dependent plasticity (STDP), in which a chemical synapse encodes firing rate (activity) information conveyed by the presynaptic neuron and the spike-timing information.

To date, several candidates for artificial synapses have been proposed. These are mainly based on complementary metal-oxide-semiconductors (CMOSs) in conjunction with memory elements such as capacitors and flash memory [18, 19, 27]. An alternative to this mainstream approach is to deploy two-terminal resistive switching elements as memory [28, 29]. In general, most of the nanoionic candidates are two-terminal capacitor-shaped devices, thus pre and postsynaptic terminals can be mapped to the device's two electrodes.

Online learning needs synapse circuitry that implements both ADP and STDP in given circumstances.

The synapse circuit in Figure 5 is an example meeting the need for online learning [30]. Pre and postsynaptic spike-firing was simulated by invoking two voltage pulse generators, which are shown in Figures 5a and 5b, respectively. The RC integrator in Figure 5b was employed to evaluate the change of postsynaptic membrane potential upon the synaptic efficacy; the integrator corresponds to the membrane of the postsynaptic neuron. The function of this circuit was to encode presynaptic activity (firing rate) and the timing of pre and postsynaptic spikes for both excitatory and inhibitory synapse cases.

The essential features of long-term plasticity of a biological synapse, long-term potentiation (LTP) and long-term depression (LTD), were realized by using a bipolar resistance switch (BRS), which is illustrated in Figure 5c. An increase in R_{BRS} results in potentiation, since the resistance increase elevates the voltage at node N2, which consequently elevates the PSP, i.e. causes potentiation. A decrease in R_{BRS} results in a change in the opposite direction so that depression is achieved. It is therefore apparent that the role of a BRS in an artificial electronic synapse depends on the circuit configuration.

The subcircuit in Figure 5d plays an important role in realization of ADP. Employing the charging and discharging of capacitor C_1 enables the polarity of a voltage, applied to the BRS, i.e. V_{N2} , to be altered without changing the polarity of the presynaptic spikes. In addition, the contribution of each charging and discharging effect to the change of R_{BRS} varies upon charging and discharging time windows. Thus, changing the ISI, while using identical spike widths, brings about a change in their relative contributions, which implies ADP. The MOSFET shown in Figure 5e, crops a part of the RC output signal at node N1 and transmits it to the BRS; cropping is controlled by the gate to which postsynaptic connection is applied. Therefore, a voltage assigned to the BRS, i.e. V_{N2} , depends on the pre and postsynaptic spike-timing, hence, implementing STDP. The subcircuit in Figure 5f determines either excitatory or inhibitory

synaptic behavior depending on the polarity of diodes D_1 . Under the current configuration, the subcircuit in Figure 5f implements an excitatory synapse and an inhibitory configuration can be realized by simply flipping the polarity of the diode. The diode is employed to introduce an asymmetric V_{N3} profile when charging and discharging capacitor C_2 , which in turn leads to asymmetry in V_{N5} , i.e. PSP. This asymmetry is attributed to the asymmetric current-voltage relationship of the diode.

Conclusions

It has been almost three decades since neuromorphic computing was first proposed. Since then, the technology has advanced considerably such that applications are on the horizon that suggest real commercial market opportunities. The concepts inherent in neuromorphic computing or engineering have now been adapted to hardware systems, thus enabling neural processing or brain-inspired data processing whether it be digital, analogue or some hybrid of digital/analogue. Further research and development work must now proceed with an eye to specific items within the neuromorphic framework as they affect the learning scheme in order to expedite outcomes.

References

- [1] LeCun Y, Bengio Y, Hinton G. *Nature* 2015; 521 (7553): 436-444.
- [2] Dayan P, Abbott LF. *Theoretical Neuroscience* 2001; The MIT Press.
- [3] Gerstner W, Kistler WM. *Spiking Neuron Models: Single Neurons, Population, Plasticity* 2002; Cambridge University Press.
- [4] Eliasmith C. et al. *Science* 2012; 338 (6111): 1202-1205.
- [5] Goodman D, Brette R. *Frontiers in Neuroinformatics* 2008; 2: 5.

- [6] Ghosh-Dastidar S, Adeli H. *Neural Networks* 2009; 22 (10): 1419-1431.
- [7] LeCun, Y. Generalization and Network Design Strategies, in *Connectionism in Perspective*, ed. Pfeifer R et al. 1989; Elsevier: 143.
- [8] Bottou L, Bousquet O. The Tradeoffs of Large Scale Learning. *Advanced in Neural Information Processing Systems* 20, ed. J.C. Platt, et al. 2007, The MIT Press: Cambridge, MA, USA.
- [9] Indiveri G et al. *Frontiers in Neuroscience* 2011; 5: 73.
- [10] Mead C. *Analog VLSI and Neural Systems* 1989; Addison-Wesley.
- [11] Pickett MD, Medeiros-Ribeiro G, Williams RS. *Nature Materials* 2012; 12: 114-117.
- [12] Lim H et al. *Scientific Reports* 2015; 5: 9776.
- [13] Mahowald M, Douglas R. *Nature* 1991; 354 (6354): 515-518.
- [14] Farquhar E, Hasler P. *IEEE Transactions on Circuits and Systems I: Regular Papers* 2005; 52 (3): 477-488.
- [15] Izhikevich EM. *IEEE Transactions on Neural Networks* 2003; 14 (6): 1569-1572.
- [16] Izhikevich EM. *IEEE Transactions on Neural Networks* 2004; 15 (5): 1063-1070.
- [17] Jeong DS et al. *Reports on Progress in Physics* 2012; 75 (7): 076502.
- [18] Ramakrishnan S, Hasler PE, Gordon C. *IEEE Transactions on Biomedical Circuits and Systems* 2011; 5 (3): 244-252.
- [19] Hasler J, Marr HB. *Frontiers in Neuroscience* 2013; 7: 118.
- [20] Tenore F et al. *Proceedings of IEEE International Symposium on Circuits and Systems* 2006: 3157-3160.
- [21] Kornijcuk V et al. *Frontiers in Neuroscience* 2016; 10.
- [22] Lim H et al. *Nanoscale* 2016; 8 (18): 9629-9640.
- [23] Jeong DS et al. *RSC Advances* 2012; 3: 3169-3183.
- [24] Jeong DS et al. *RSC Advances* 2013; 3 (10): 3169-3183.
- [25] Malenka RC, Nicoll RA. *Science* 1999; 285 (5435): 1870-1874.
- [26] Bissiere S et al. *Science* 2011; 331 (6013): 87-91.
- [27] Indiveri G, Chicca E, Douglas R. *IEEE Transactions on Neural Networks* 2006; 17 (1): 211-221.
- [28] Pershin YV, Di Ventra M. *Physical Review E* 2013; 88 (1): 013305.
- [29] Pershin YV, Di Ventra M. *Physical Review E* 2011; 84 (4): 046703.
- [30] Kornijcuk V et al. *Nanoscale* 2014; 6 (24): 15151-15160.

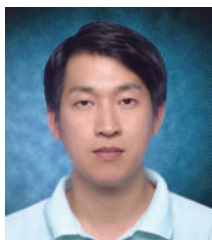
Feature Articles

Electrical Detection of Coherent Spin Precession Using the Ballistic Intrinsic Spin Hall Effect



Won Young CHOI

Center for Spintronics
Post-Silicon Semiconductor Institute
213341@kist.re.kr



Hyun Cheol KOO

Center for Spintronics
Post-Silicon Semiconductor Institute
hckoo@kist.re.kr

Introduction

In a semiconductor channel, the spin-orbit interaction provides an exceptionally fascinating area of research. The Rashba effective magnetic field [1, 2] in the channel of a spin field effect transistor [3, 4] and the spin Hall effect [5, 7] are the two most compelling topics in this area. In this research, we combine these effects to provide a direct demonstration of the ballistic intrinsic spin Hall effect [8] and demonstrate a technique for an all-electric measurement of the Datta–Das [3] conductance oscillation due to spin precession. These experiments show that the ballistic spin Hall effect can be used for efficient injection or detection of spin polarized electrons, thereby enabling the development of an integrated spin transistor.

Experiments

InAs quantum well structure

An InAs-based two dimensional electron gas structure was epitaxially grown in a molecular beam epitaxy system with a layered structure: InAs (2 nm)/In_{0.52}Al_{0.48}As (20 nm)/In_{0.53}Ga_{0.47}As (13.5 nm)/InAs quantum well (2 nm)/In_{0.53}Ga_{0.47}As (2.5 nm)/In_{0.52}Al_{0.48}As (6 nm)/n⁺In_{0.52}Al_{0.48}As (7 nm)/In_{0.52}Al_{0.48}As buffer (300 nm)/ semi-insulating InP(001) substrate. The In_{0.52}Al_{0.48}As and In_{0.53}Ga_{0.47}As double layers serve as barrier layers to

confine the electrons in the quantum well.

Transport measurements determined the following characteristics at 1.8 K: carrier density $n_s = 2.0 \times 10^{12} \text{ cm}^{-2}$ and mobility $\mu = 60,000 \text{ cm}^2 \text{ V}^{-1} \text{ s}^{-1}$. The mean free path, $l = 1.61 \text{ }\mu\text{m}$, was determined using resistivity and Hall measurements [4]. For calculation, we utilized $m^* = 0.05m_0$ ($m_0 = 9.1 \times 10^{-31} \text{ kg}$)⁴. The Rashba spin-orbit strength was determined to be $\alpha = 8.93 \times 10^{-12} \text{ eV}\text{m}$ at zero gate voltage ($V_G = 0$) from the beat frequency in Shubnikov–de Haas measurements [4].

Spin Hall effect

Figures 1a and 1b help illustrate the unique combination of direct spin Hall effect (DSHE) [6, 9] and inverse spin Hall effect (ISHE) mechanisms [10–12]. In Figure 1a, an unpolarized current \mathbf{J} flows with electron velocity along the $-x$ direction in a material with strong spin-orbit coupling. The spin Hall force \mathbf{F} has an opposite sign on electrons with opposite spin, creating nonequilibrium populations of spin polarized electrons along opposite

sides of the sample. An open circuit Hall voltage measurement would display $V_H = 0$, but a ferromagnetic electrode could be used to detect the spin population on either side. In Figure 1b, the electric current has more up-spins than down-spins ($\mathbf{J}_S \neq 0$). The force \mathbf{F} is the same, but the unequal number of spins results in unequal populations on opposite sides of the sample. Thus, a Hall measurement would result in a voltage, $V_H = V_{SH}$.

Our technique for measuring coherent spin precession is explained by Figure 1c. A ferromagnetic electrode (FM), with in-plane magnetization M_x , injects spin polarized electrons at $x = 0$. Using a nonlocal geometry [3, 13–15], the bias current I is drained at the far left end of the wire and the sample region $x > 0$ has zero net charge current. A portion of the injected electrons have ballistic trajectories along the x axis and travel with the Fermi velocity. The Rashba effective magnetic field, \mathbf{B}_R , is perpendicular to both the intrinsic electric field E_z and the carrier velocity v_x . An injected electron with initial spin angular momentum, S_x , precesses in the x - z plane under the influence of $-\mathbf{B}_{Ry}$, with wavelength λ . By the end of the ballistic trajectory, at $x \approx l$, the spin moment phase

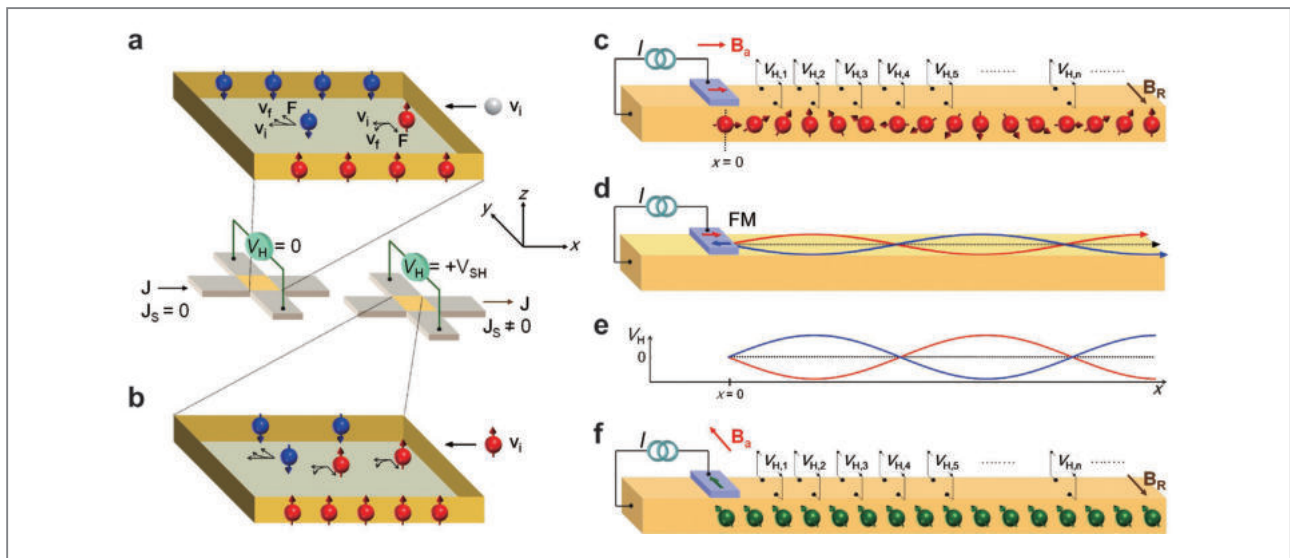


Figure 1. Illustration of spin Hall effect and experimental technique. a) Direct spin Hall effect. b) Inverse spin Hall effect. c) Experimental geometry. d) Deflection of ballistic trajectories caused by the intrinsic spin Hall effect. e) Hall voltage in region $x > 0$ as a result of inverse spin Hall effect. f) Perspective view where B_s sets the FM magnetization along the y axis.

accumulation $\Delta\theta$ is several multiples of 2π if $\lambda < l$.

In a heuristic model, the ballistic trajectories deflect along the positive or negative y direction in a sinusoidal way (Figure 1d, red trace). The nodes are at positions with \mathbf{S} along the x axis and the antinodes have \mathbf{S} along the z axis. A Hall cross at position x along the trajectory will record the ISHE voltage that is proportional to the trajectory deflection. A plot of voltages $V_{H,n}(x)$, recorded by a series of Hall crosses at variable position x , will show the Datta–Das voltage oscillation (Figure 1e, red and blue traces), with wavelength given by [3, 4]

$$\lambda = \pi\hbar^2 / \alpha m^*, \quad (1)$$

where \hbar is Planck's constant divided by 2π . Our model gives a prediction for $V_H(\Delta\theta(L))$ for each channel length L . Observing the Datta–Das oscillation in a plot of

$V_H(L)$ requires that the phase accumulation $\Delta\theta(x)$ must be exactly the same at a given gate voltage for every independent device.

Results

Using material parameters of InAs quantum well structure, we calculate the Datta–Das wavelength to be $\lambda = 0.54 \mu\text{m}$ ($\ll l$). Figure 2a is a sketch of an individual device. Describing the data in Figure 2b, in the absence of field, the FM shape anisotropy causes the magnetization to align along the y axis, $\pm M_y$. Injected electrons have \mathbf{S} along the y axis; there is no spin precession, $\mathbf{F} = 0$ and $V_H(B_a = 0) = 0$. Increasing B_a tips M_y towards the x axis and gives the injected spins an x -component. The

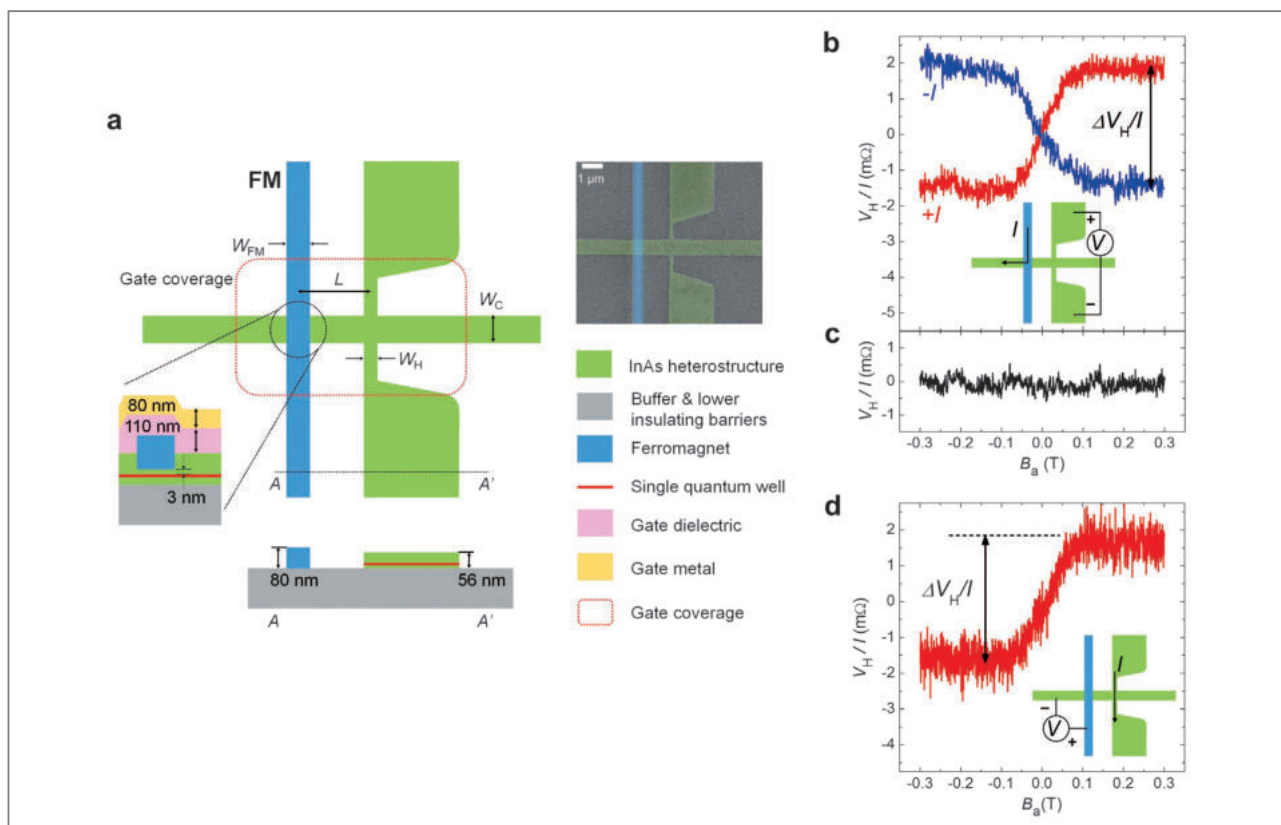


Figure 2. Spin precession induced spin Hall effect. a) Schematic top and cross-section views of geometry of each individual device. b) Inverse spin Hall signal with B_{ax} . c) Control experiment of b) with B_{ay} . d) Direct spin Hall signal with B_{ax} .

external field overcomes the shape anisotropy and the magnetization is saturated along the $+x$ ($-x$) axis for $B_a > 0.12$ T ($B_a < -0.12$ T). In these ranges of field, injected spins are oriented directly along the x axis. The spins now precess; \mathbf{S} has a component along z at $x = L$, and a nonzero spin Hall voltage is measured. In Figure 2b, Channel length $L = 2.83 \mu\text{m}$ corresponds to 5.25λ ($m = 21$) and the local spin orientation, \mathbf{S} , is along the z axis; both \mathbf{F} and V_H have maximal values (antinodes in Figure 1d).

Data for which the polarity of bias current is reversed (blue lines) are also shown in Figure 2b. The injected spins have opposite orientation and the sign of the intrinsic ISHE voltage is reversed. The data of Figure 2b show the magnitude of the intrinsic ISHE to be $\Delta R_H = \Delta V_H/I = 3.6 \text{ m}\Omega$. The results of a control experiment are shown in Figure 2c. When the applied field \mathbf{B}_a is swept along the y axis, \mathbf{M} is always parallel with the y axis. Injected spins are oriented along y ; there is no spin precession, $\mathbf{F} = 0$ for all x , and $V_H = 0$ for the entire range of B_a (Figures 1d and 1f).

Figure 2d shows the results of converse measurements on the same device to demonstrate the ballistic intrinsic DSHE. Driving a bias current along the vertical arms of the Hall cross creates spin-up electrons with velocity components along the $-x$ direction, near the left side of the Hall cross region. Some of these carriers have ballistic trajectories to the vicinity of FM, which now performs as a spin detector. This measurement with intrinsic SHE spin injection and FM spin detection gives the same result as the ISHE experiment, $\Delta R_H = 3.6 \text{ m}\Omega$.

We next describe the set of ballistic intrinsic ISHE experiments in which 14 individual devices have width $w_C = 0.75 \mu\text{m}$ but the distance L is systematically varied from 0.64 to $1.72 \mu\text{m}$. Examples of data are shown in Figure 3a and we note that the sign of ΔRH can be positive or negative. Values of ΔRH are plotted as a function of L in Figure 3b and two full wavelengths of the Datta–Das conductance oscillation are clearly seen. The dotted line is a fit to the Datta–Das wavelength,

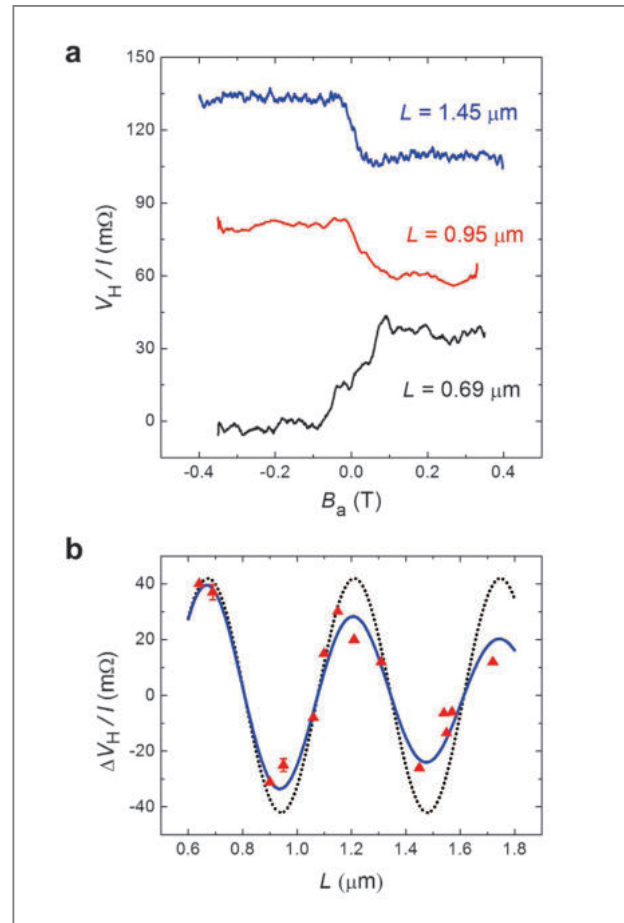


Figure 3. Channel length dependence of the inverse spin Hall voltages. a) Examples of inverse spin Hall voltages for several lengths, L . b) ΔR_H as a function of channel length L .

$$\frac{\Delta V_H}{I} = \Delta R_H = A \cos(\Delta\theta - 90^\circ) = A \cos(2\pi L/\lambda - 90^\circ), \quad (2)$$

where A is the measured amplitude and λ is from equation (1). The solid line fit includes an exponential decay $e^{-L/l}$ governed by the mean free path of ballistic trajectories, independently measured [4] to be $l = 1.61 \mu\text{m}$. The amplitude, determined by ΔRH for $L = 0.64 \mu\text{m}$, is the only free-fitting parameter. The fits in

Figure 3b are determined only by the distance L between injector and detector.

The observation of two full wavelengths of the Datta–Das oscillation is a graphical demonstration that

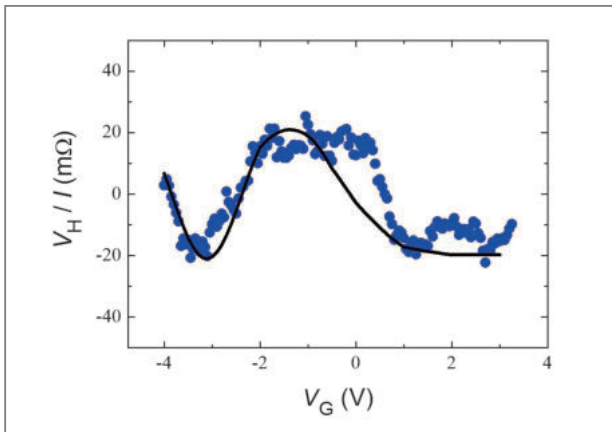


Figure 4. Gate control of coherent spin precession in spin injected transistor with inverse spin Hall effect.

the results of all devices fit our model. Because the oscillation requires ballistic transport, these data confirm the absence of scattering and therefore the detected ISHE must be *intrinsic*.

Having confirmed the presence of the intrinsic ISHE in our samples, we finally use the classic Datta–Das technique [3, 4] to observe gate voltage controlled spin precession in a spin-FET with intrinsic ISHE detector. A gated device is prepared ($w_c = 0.75 \mu\text{m}$, $L = 0.9 \mu\text{m}$) and an external field $B_a = -0.4 \text{ T}$ orients the FM injector magnetization to lie along the $-x$ direction. As V_G is varied through the range $-4 \text{ V} < V_G < +3.2 \text{ V}$, spin orbit parameter $\alpha(V_G)$ varies from [4] $1.46 \times 10^{-11} \text{ eVm}$ to $8.01 \times 10^{-12} \text{ eVm}$ and the voltage detected by the ballistic intrinsic ISHE oscillates as [3, 4]

$$V_H = A' \cos(2\alpha m^* L / \hbar^2 + \varphi), \quad (3)$$

where A' is the measured amplitude and φ is an arbitrary phase shift. The solid line fit is calculated from equation (3) using values $\alpha(V_G)$ that are experimentally determined from Shubnikov–de Haas measurements [4]. The detailed shape of the fit is not purely sinusoidal and has been explained by numerical calculations [16]. Comparing the peak-to-peak amplitude of the oscillation in Figure 4 ($L = 0.9 \mu\text{m}$) with the magnitude ΔR_H for a comparable ungated device ($L = 0.9 \mu\text{m}$, Figure 3b), the

SHE voltage in the former is larger by the ratio 4/3 ($40 \text{ m}\Omega/30 \text{ m}\Omega$). Since an intrinsic mechanism depends on band structure, this is consistent with the expectation that a gate voltage modulates the bands and V_H .

Conclusion

In this research, we measured both the ISHE and the DSHE using ballistic transport and therefore have directly demonstrated the existence of the *intrinsic* spin Hall effect. Our results show that the ballistic intrinsic spin Hall effect can be used as both spin injector and detector with good efficiency. Using the ballistic spin Hall effect may permit the fabrication of fully integrated spin-FET structures, and the Indium arsenide materials system has shown good properties for nanometer sized devices [17].

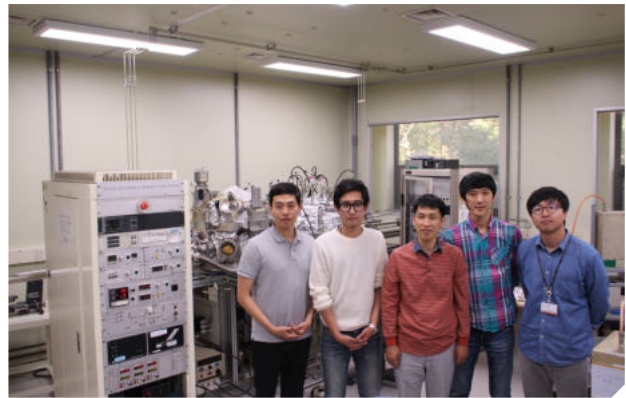
Note

This article and images are drawn from “Electrical detection of coherent spin precession using the ballistic intrinsic spin Hall effect” in *Nature Nanotechnology*, Vol. 10, P. 666, 2015.

References

- [1] Bychkov, Yu. A. & Rashba E. I. *JETP Lett.* 39, 78–81 (1984).
- [2] Vas’ko F. T. *JETP Lett.* 30, 541–544 (1979).
- [3] Datta S. & Das B. *Appl. Phys. Lett.* 56, 665–667 (1990).
- [4] Koo, H. C. *et al. Science* 325, 1515–1518 (2009).
- [5] Dyakonov, M. I. & Perel, V. I. *JETP Lett.* 13, 467–470 (1971).
- [6] Hirsch, J. E. *Phys. Rev. Lett.* 83, 1834–1837 (1999).
- [7] Zhang, S. *Phys. Rev. Lett.* 85, 393–396 (2000).
- [8] Wunderlich, J., Kaestner, B., Sinova, J. & Jungwirth, T. *Phys. Rev. Lett.* 94, 047204 (2005).

- [9] Dyakonov, M. I. & Khaetskii, A. V. in *Spin Physics in Semiconductors*. (ed. M. I. Dyakonov) 211-243 Springer-Verlag, Berlin, 2008).
- [10] Valenzuela, S. O. & Tinkham, M. *Nature* 442, 176–179 (2006).
- [11] Seki, T. *et al. Nature Mater.* 7, 125–129 (2008).
- [12] Wunderlich, J. *et al. Science* 330, 1801–1804 (2010).
- [13] Koo, H. C. *et al. Appl. Phys. Lett.* 90, 022101 (2007).
- [14] Johnson, M. & Silsbee, R. H. *Phys. Rev. Lett.* 55, 1790–1793 (1985).
- [15] Lou, X. *et al. Nature Phys.* 3, 197–202 (2007).
- [16] Zainuddin, A. N. M., Hong, S., Siddiqui, L., Srinivasan S. & Datta, S. *Phys. Rev. B* 84, 165306 (2011).
- [17] Ford, A. *et al. Nano Lett.* 9, 360 (2009).



Feature Articles

Thermal Spin Transfer Torque Driven by Spin-Dependent Seebeck Effect in Metallic Spin-Valve Structures



Gyung Min CHOI

Center for Spintronics
Post-Silicon Semiconductor Institute
gm_choi@kist.re.kr

Introduction

Spin transfer torque (STT), the transfer of the spin angular momentum of conduction electrons to the magnetization of a ferromagnet, enables the manipulation of nanomagnets with spin currents [1, 2]. STT is intensely studied because of its potential for applications in magnetic random access memories, programmable logics, and microwave oscillators, and has often been realized by passing electrical currents through magnetic layers [3, 4]

The coupling of heat and spin transport also offers a unique possibility for the generation of STT by passing heat currents through magnetic layers. Hatami et al. theoretically predicted thermally-driven STT in metallic spin valves [5]; Slonczewski suggested the initiation of thermally-driven STT in ferrite/metal structures and predicted a greatly enhanced quantum efficiency compared to current-driven STT [6]. These new “thermal STT” phenomena rely on the transport of thermal energy, in contrast to the transport of electrical charge, and provide a new way to manipulate magnetization.

Here we provide direct evidence of thermal STT in metallic spin-valves with the Pt/FM1/Cu/FM2 structure, where FM1 is the spin source layer of [Co/Pt] or [Co/Ni], and FM2 is the spin detection layer of CoFeB. Heating by an ultrafast pump optical pulse generates spin currents in the structure by two distinct mechanisms: i) volumetric spin generation in the FM1 layer by ultrafast demagnetization of FM1; and ii) interfacial spin generation at the Pt/FM1 and FM1/Cu interfaces by spin-dependent Seebeck effect (SDSE)

coefficient, where $\sigma_{\uparrow,\downarrow}$ is the electrical conductivity of spin up/down and $S_{\uparrow,\downarrow}$ is the Seebeck coefficient of spin up/down, L is the Lorenz number, T is the temperature of FM1, and J_Q is the heat current flowing through FM1.

Spin accumulation driven by heat current

Spin generated in FM1 diffuses into Cu and leads to a spin accumulation, which is observed as Kerr rotation probed at the Cu side of the Pt/FM1/Cu samples (Figure 3 (a)). The spin accumulation in Cu consists of two components: i) a component driven by demagnetization and ii) a component driven by SDSE. The demagnetization-driven spin generation ($g_s = -dM/dt$) of [Co/Pt] and [Co/Ni] has positive and negative peaks at 0 and ~ 1 ps, respectively, and approaches zero after ~ 3 ps (Figure 3 (b)).

In addition to the short response time response, and critical for the discussion that follows, we observe that the Kerr signal has a vertical offset at 10 ps. The offset is negative for [Co/Pt] and positive for [Co/Ni] (inset of Figure 3 (a)). The offset at 10 ps indicates that there is a spin generation mechanism on relatively long timescales which has an opposite sign for [Co/Pt] and [Co/Ni].

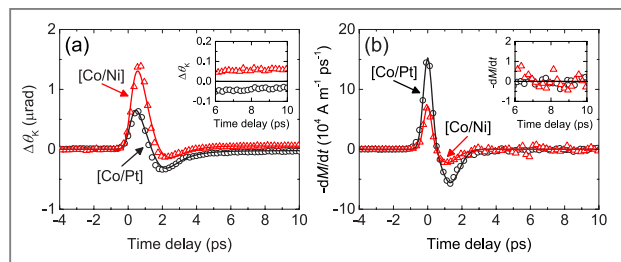


Figure 3. Spin accumulation in Cu. (a) Kerr rotation measured on the Cu side of the Pt/[Co/Pt]/Cu (black circles) and Pt/[Co/Ni]/Cu samples (red triangles). Solid lines are calculations with $\tau_s = 0.02$ and 0.1 ps, and $S_s = 6$ and -12 μV for [Co/Pt] and [Co/Ni], respectively. (b) The $-dM/dt$ obtained by numerical differentiation of demagnetization data. Insets of (a) and (b) are zoomed-in data around the y-axis at zero.

STT driven by heat current

An unequivocal demonstration of thermal STT requires an evidence of torque exerted on FM2. We demonstrate thermal STT through the magnetization dynamics of a CoFeB layer separated from the [Co/Pt] or [Co/Ni] layer by a Cu layer. The absorbed spin current produces STT and triggers precession of the CoFeB magnetization. Although the SDSE produces just a small offset in spin accumulation, its effect on STT is significant because it lasts much longer (~ 100 ps) than dM/dt (~ 3 ps).

We measure the CoFeB precession by probing on the CoFeB side of the [Co/Pt] or [Co/Ni]/Cu/CoFeB sample with an in-plane magnetic field of 0.05 T. The amplitude of the CoFeB precession is substantially different with [Co/Pt] and [Co/Ni] (Figures. 4). Such a large difference of amplitude suggests that SDSE-driven STT is more significant than the demagnetization-driven STT.

More direct evidence of the SDSE-driven STT can be seen in the initial slope of the CoFeB magnetization dynamics (Figure 5 (a)). Both [Co/Pt] and [Co/Ni] produce a sharp $+z$ tilting of the CoFeB magnetization at ≈ 1 ps as a result of a pulse-like demagnetization-driven STT. After 3 ps, the demagnetization-driven STT is insignificant and the more persistent SDSE-driven STT produces $-z$ and $+z$ slopes of the CoFeB dynamics with

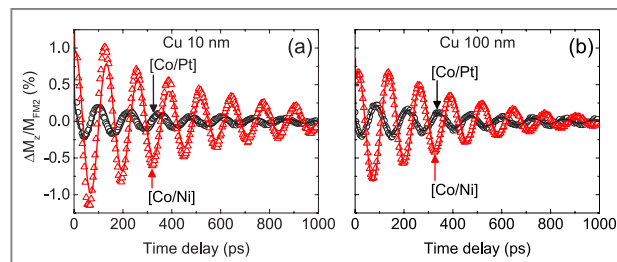


Figure 4. STT on CoFeB at long time scale. The magnetization dynamics of CoFeB of the Pt/[Co/Pt] or [Co/Ni]/Cu/CoFeB samples with Cu thickness of (a) 10 nm and (b) 100 nm. Solid lines are calculations with $\tau_s = 0.02$ and 0.1 ps, and $S_s = 6$ and -12 μV for [Co/Pt] and [Co/Ni], respectively.

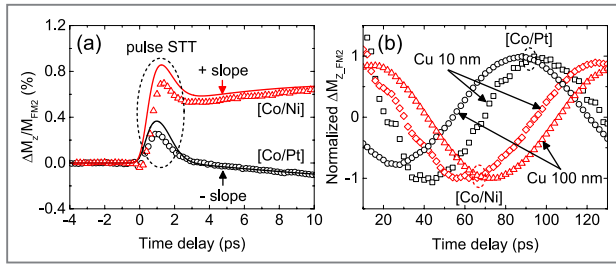


Figure 5. STT on CoFeB at short time scales. The magnetization dynamics of CoFeB of the Pt/[Co/Pt] or [Co/Ni]/Cu/CoFeB samples (a) from -4 to 10 ps and from (b) from 10 to 130 ps. Solid lines of (a) are the same as those of Fig. 4 (b). All data of (b) are normalized by their peak value.

[Co/Pt] and [Co/Ni], respectively. The different slopes at delay times between 3 and 10 ps clearly reveal the different sign of the SDSE-driven STT.

Lastly, the phase ϕ of the CoFeB precession depends on the composition of FM1 and the thickness of Cu. We define ϕ relative to a damped cosine function of $\cos(2\pi ft + \phi)\exp(-t/\tau)$. Since the pulse-like STT by demagnetization does not create a phase shift, the positive and negative phases are consequences of the SDSE-driven STT and proportional to the ratio between the SDSE-driven STT and demagnetization-driven STT. A large phase difference, $\Delta\phi$, between [Co/Pt] and [Co/Ni] of 130° with Cu 100 nm, suggests a significant role of SDSE. The $\Delta\phi$ decreases to 60° with Cu 10 nm because the heat current with Cu 10 nm is 2~3 times smaller than with Cu 100 nm (Fig. 2 (c)).

Analysis of thermal STT

Quantitative understanding of the STT results requires modeling of spin transport. We use the spin diffusion equation [8],

$$\frac{\partial \mu_s}{\partial t} = D \frac{\partial^2 \mu_s}{\partial^2 t} - \frac{\mu_s}{\tau_s} + \left(\frac{g_s}{N_s} \right), \quad (3)$$

where $\mu_s = \mu_\uparrow - \mu_\downarrow$ is the spin chemical potential, D is the spin diffusion constant, τ_s is the spin relaxation

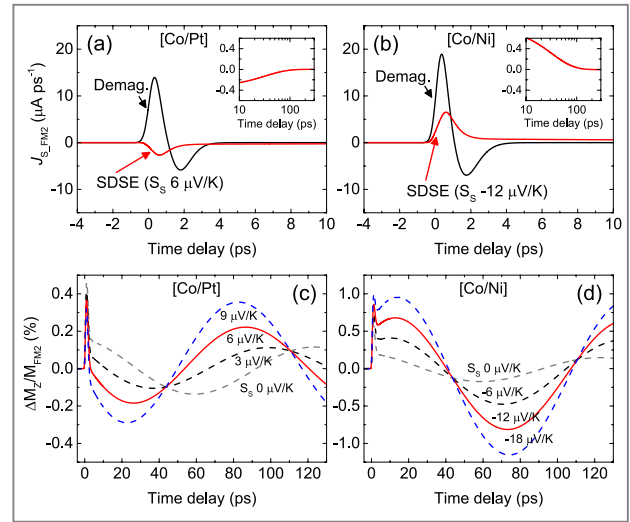


Figure 6. The effect of SDSE on STT. The calculated spin current absorbed by CoFeB in the Pt/[Co/Pt] or [Co/Ni]/Cu/CoFeB samples with τ_s of 0.02 and 0.1 ps, and S_s of 6 and -12 μV for [Co/Pt] and [Co/Ni], respectively: the black and red solid lines are driven by demagnetization and SDSE, respectively. Insets of (a) and (b) are the SDSE part at time scale of 10–300 ps. The calculation of the STT-driven magnetization dynamics of CoFeB with different S_s of (c) [Co/Pt] and (d) [Co/Ni].

time, g_s is the spin generation rate, and N_s is the spin density of states. The μ_s of adjacent layers are related by spin conductances at the interfaces. We incorporate two spin generation terms: i) the volumetric $g_s = -\frac{dM}{dt}$ in FM1; and ii) the interfacial $G_s = (-/+)\left(\frac{\mu_B}{e}\right)\left(\frac{S_s}{LT}\right)J_Q$ at FM1/Cu and Pt/FM1 interfaces. For g_s , we obtain $-dM/dt$ from the experimental demagnetization data (Figure. 3 (b)), and for G_s , we use S_s as a free parameter with J_Q from our models of thermal transport (Figure. 2 (c)).

The sign and magnitude of S_s determine the initial slope and phase of the CoFeB precession dynamics (Figures. 6). From the simultaneous fitting of calculations both to the spin accumulation (Figure. 3) and STT results (Figures. 4 and 5), we determine $\tau_s = 0.02$ and 0.1 ps, and $S_s = 6$ and -12 μV for [Co/Pt] and [Co/Ni], respectively.

For thermal STT, the input is an energy density rather than a charge current density as in more conventional spintronics. Using a [Co/Ni] layer as a spin source, an energy fluence of ≈ 4 J m^{-2} induces thermal STT

that generates a $\approx 1\%$ tilting of the 2 nm-thick CoFeB magnetization. One route to greater energy efficiency is to increase S_S by controlling the band structure of materials. A tunable band structure of half-metallic alloy raises prospects for an enhanced thermal STT.

Note

This article and images are drawn from “Thermal spin transfer torque driven by spin-dependent Seebeck effect in metallic spin-valve structures” in *Nature Physics*, Vol. 11, pg. 576.

References

- [1] Slonczewski JC. *J. Magn. Magn. Mater.* 1996; 159: L1-L7.
- [2] Berger L. *Phys. Rev. B.* 1996; 54: 9353-9358.
- [3] Tsoi M, Jansen AGM, Bass J, Chiang W-C, Seck M, Tsoi V, Wyder P. *Phys. Rev. Lett.* 1998; 80: 4281-4284.
- [4] Katine JA, Albert FJ, Buhrman RA, Myers EB, Ralph DC. *Phys. Rev. Lett.* 2000; 84: 3149-3152.
- [5] Hatami M, Bauer GEW, Zhang Q, Kelly PJ. *Phys. Rev. Lett.* 2007; 99: 066603.
- [6] Slonczewski JC. *Phys. Rev. B.* 2010; 82: 054403.
- [7] Slachter A, Bakker FL, Adam J-P, van Wees BJ. *Nature Phys.* 2010; 6: 879-882.
- [8] Valet T, Fert A. *Phys. Rev. B.* 1993; 48: 7099-7113.



Technical Review

Highly Efficient Ceria-Promoted Sb-V/ TiO₂ Catalyst for the Abatement of NO_x by NH₃ from the Exhaust of Stationary and Marine Engines

**Heon Phil HA**

Materials Architecturing
Research Center
Materials and Life
Science Research
Division
heonphil@kist.re.kr

**Pullur Anil Kumar**

Materials Architecturing
Research Center
Materials and Life Science
Research Division
f05793@kist.re.kr

**Eun Young JEONG**

Materials Architecturing
Research Center
Materials and Life
Science Research
Division
213012@kist.re.kr

Introduction

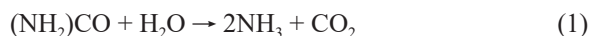
The emission of nitrogen oxides (NO_x, x = 1,2) from stationary and mobile exhaust is currently a major environmental pollution issue. These NO_x emissions contribute to environmental degradation in various ways: photochemical smog, acid rain, ozone depletion, and fine particle pollution. The major source of nitrogen oxides is the combustion of fossil fuels, especially petroleum and petroleum products in vehicular engines as well as coal in thermal power plants [1]. The abatement of NO_x from diesel engines has been a particularly tough challenge in environmental catalysis, but recently, research into selective catalytic reduction (SCR) of NO_x with NH₃ (NH₃-SCR) has led to a highly promising technology for the removal of NO_x from diesel engines at low temperatures. The main focus of this technical review is to describe KIST's efforts in developing SCR catalysts for the removal of NO_x by ammonia in the presence of excess SO₂ and H₂O at low temperatures.

Background

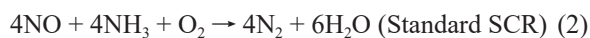
More than a half century ago, in the early 1960s, the development of SCR technology was initiated by Japan and the United States with research focusing on less expensive and more durable catalysts. The NH₃-SCR

process was commercially implemented in Japan in the 1970s and a decade later in the U.S., Germany, and Austria. In 1978, the first scale power plant installation with a SCR NO_x removal system was launched by the IHA Corporation. Since the 1980s, these installations have already become common in coal power plants with variable coal sulfur content in fuel. SCR is the only commercially proven method available for removing up to 95% of the NO_x emissions in power generation facilities. Commercial SCR systems, which are typically found in industrial boilers, large utility boilers, municipal solid waste incinerators, etc., have been shown to reduce NO_x by 70-95%. More recently, NH₃-SCR systems have been applied in diesel engines, such as those found on large ships, diesel locomotives, gas turbines, and automobiles.

A selective NO_x reduction system using NH₃ with V₂O₅-TiO₂ was developed in Japan around 40 years ago. Soon after, an NH₃ reduction system using urea, which is decomposed to NH₃ and CO₂ at temperatures higher than 170°C, was applied in passenger cars in Europe.



The SCR reaction is as follows:



Although vanadia-titania-based catalysts are highly active and quite resistant to SO₂, there are several drawbacks to their use, including: (a) poor N₂ selectivity at high temperatures; (b) higher levels of toxic V₂O₅; (c) high conversion of SO₂ to SO₃; (d) phase transformation of TiO₂ from anatase to rutile at high temperatures (above 500°C) reducing its activity; and (e) a narrow active temperature window of 300–400°C (although this temperature range does help prevent pore plugging from the deposition of ammonium sulfate salts such as NH₄HSO₄ and (NH₄)₂SO₄ on the catalyst surface) [2]. The addition of tungsten (W) or molybdenum (Mo) has

helped to overcome the phase transformation problem, and many other efforts have been made by researchers to further modify the V₂O₅-WO₃/TiO₂ catalyst system for NH₃ SCR.

Design and applications of DeNO_x catalyst developed at KIST

In the course of our study at KIST, we have designed catalysts for NH₃-SCR by the quantum chemical calculation (QCC) method to weaken the adsorption of ammonium bisulfate on the catalyst surface. Ultimately, we developed a highly active Sb promoted V₂O₅/TiO₂ catalyst [3, 4] for NH₃-SCR in the presence of excess H₂O and SO₂ at low-temperatures. The developed technologies were transferred to Daeyoung C&E Co. This company made corrugated type DeNO_x modules using KIST catalysts and successfully installed them at the sintering furnace of Pohang Iron and Steel Company of the Republic of Korea (POSCO) to treat NO_x in the flue gas (Figure 1). However, catalysts used for marine operation need to be effective in a wide range of temperatures, besides having an optimal activity at low temperatures, and must function effectively in the presence of fuels with



Figure 1. Installation of the KIST catalyst to the De NO_x system of POSCO sintering furnace.



Figure 2. The world 1st official shop test of the LP SCR catalyst system was carried out with a marine engine of Doosan Engine co.

a high sulfur content. Efforts are underway to develop these new catalysts. In our latest studies for NH_3 -SCR of NO_x , we have reported on a ceria-added $\text{Sb-V}_2\text{O}_5/\text{TiO}_2$ catalyst which showed high sulfur tolerance at 240°C [4-7]. This catalyst is expected to satisfy the urgently required catalytic properties for marine diesel application under abundant SO_2 conditions at low temperatures. The patented technology was transferred to a marine engine market and successfully installed and tested in a 13 MW marine engine (Figure 2).

Experimental

Preparation of the catalysts

A commercial TiO_2 (DT-51, Cristal Global) powder was used as a support for the preparation of all catalysts. The $\text{Sb-V}_2\text{O}_5/\text{TiO}_2$ catalyst was prepared by incipient wetness co-impregnation of vanadia and antimony on titania by using ammonium metavanadate (NH_4VO_3) (99%, Junsei chemicals) and antimony acetate (97%, Alfa Aesar) precursors, respectively. The required amount of ammonium metavanadate was added to an oxalic acid solution, followed by heating to dissolve the ammonium metavanadate. A calculated amount of titania (DT-51) powder was added to this solution and stirred for 1 h, followed by evaporation, drying, and calcination at 500°C for 5 h. Similarly, to understand the effect

of Ce-addition, $\text{V}_2\text{O}_5\text{-CeO}_2/\text{TiO}_2$ and $\text{Sb-V}_2\text{O}_5\text{-CeO}_2/\text{TiO}_2$ (Sb was chosen due to excellent sulfur tolerance at low temperatures) catalysts were prepared by incipient wetness co-impregnation of vanadia and antimony on a prepared $\text{CeO}_2/\text{TiO}_2$ support. The $\text{CeO}_2/\text{TiO}_2$ support was synthesized through a deposition precipitation method by hydrolysis with ammonium hydroxide (Aldrich, 25%). In a typical experiment, the required quantities of cerium (III) nitrate ($\text{Ce}(\text{NO}_3)_3 \cdot 6\text{H}_2\text{O}$, Alfa Aesar, 99.5%) and commercial TiO_2 (DT-51, Cristal Global) powder were mixed together in a beaker with de-ionized water. To this mixed solution, dilute aqueous ammonia was added as a precipitating agent and the resultant precipitate was filtered off. The obtained cake was oven dried at 120°C for 12 h and then calcined at 500°C for 5 h. The obtained $\text{V}_2\text{O}_5\text{-Ce}/\text{TiO}_2$ and $\text{Sb-V}_2\text{O}_5\text{-Ce}/\text{TiO}_2$ catalysts were denoted as VCe/TiO_2 and $\text{SbV}\chi\text{Ce}/\text{TiO}_2$ ($\chi = 0, 5, 10$ and 15 wt% of ceria). For sulfated catalysts, the $\text{Sb-V}_2\text{O}_5\text{-CeO}_2/\text{TiO}_2$ catalyst was treated with SO_2 (500 ppm) and O_2 (3%) with balance N_2 for 2 h at various temperatures (300, 400 and 500°C). The samples were then labeled as S300, S400 and S500, respectively.

Results and Discussion

Activity of the powdered catalysts

The addition of ceria enhanced catalytic activities both at low and high temperatures (Figure 3). This difference in catalytic activity was more apparent at higher temperatures, but the improvement in NO_x conversion was also observed at low temperatures between 175 to 250°C . As ceria loading increased from 5 to 10 wt%, a significant enhancement in the NO_x conversion was observed. However, a further increase in the ceria loading decreased the NO_x conversion, and displayed more or less similar activities for both 5 and 15 wt% ceria-loaded catalysts under given reaction conditions. Moreover, the $\text{SbV10Ce}/\text{TiO}_2$ catalyst demonstrated an NO_x conversion of nearly 99% at temperatures as low as 220°C , and

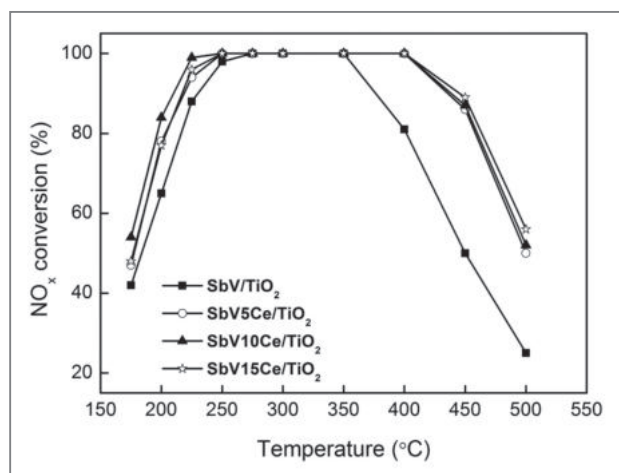


Figure 3. NO_x conversion of ceria added SbV/TiO₂ catalysts. (Reaction conditions: 800 ppm NO_x, 800 ppm NH₃, 3 vol% O₂, GHSV – 60,000 h⁻¹).

clearly widened the working temperature window from 250 – 400°C to 200 – 450°C. It is worth noting that the addition of ceria widened the SCR activity temperature window due to the positive synergetic effects of Ce, V, Sb on the surface of TiO₂.

In **Figure 4(a)**, the effect of H₂O and SO₂ on NO_x conversion over SbV/TiO₂, SbV10Ce/TiO₂ and V10Ce/TiO₂ catalysts are displayed. At operating temperatures below 250°C, it was observed that the addition of 6 vol% H₂O and 800 ppm SO₂ into the reaction stream reduced the catalytic activity, while above 350°C, higher NO_x conversions were noticed. These results implied that water vapor and SO₂ had inhibiting effects at lower temperatures. When temperatures were high, however, the catalysts showed strong resistance to H₂O and SO₂. It can be observed in **Figure 4(a)** that the SbV/TiO₂ catalyst showed lower NO_x conversions compared to the other two catalysts. However, the SbV10Ce/TiO₂ catalyst showed superior catalytic activity (higher than 87%) in a wide temperature window ranging from 220 to 500°C. These results revealed that the addition of ceria could enhance the SO₂ and H₂O resistance. The selectivities of N₂ and N₂O over SbV/TiO₂, SbV10Ce/TiO₂ and V10Ce/TiO₂ catalysts are shown in **Figures 4(b)**

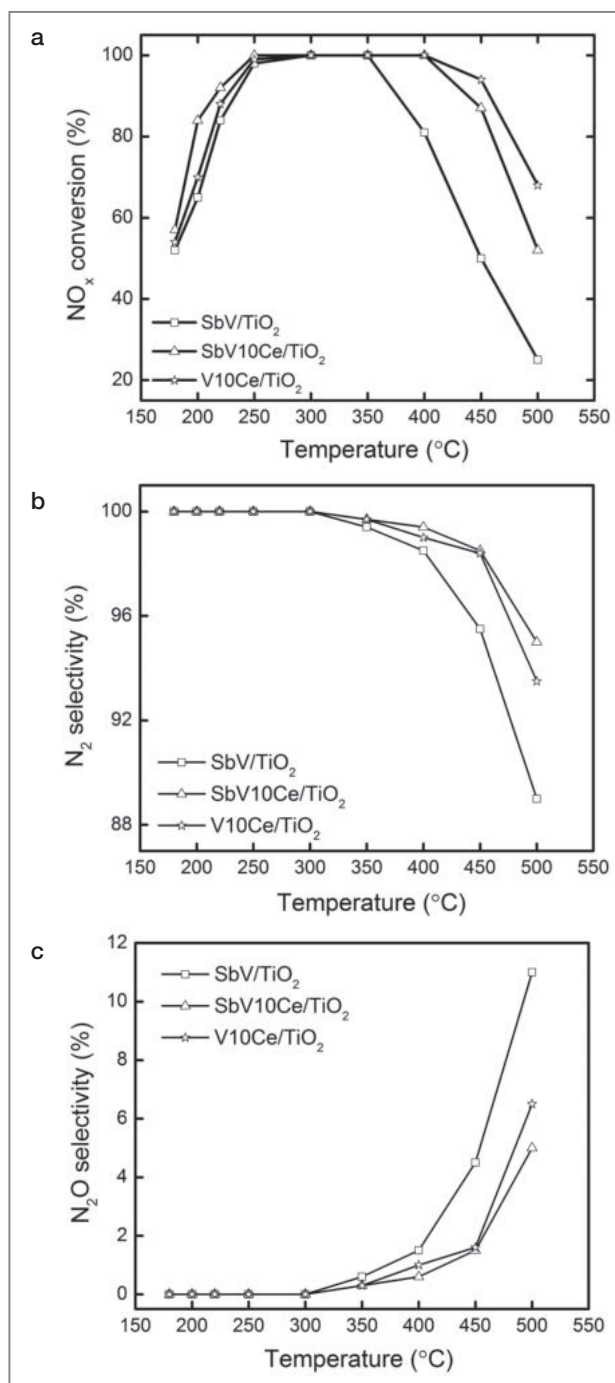


Figure 4. Activity of SbV/TiO₂, SbV10Ce/TiO₂ and V10Ce/TiO₂ samples under H₂O and SO₂ (A) NO_x conversion (B) N₂ selectivity and (C) N₂O selectivity. (Reaction conditions: 800 ppm NO_x, 800 ppm NH₃, 3 vol% O₂, 6 vol% H₂O, 800 ppm SO₂, GHSV – 60,000 h⁻¹).

and 4(c), respectively. We found that the formation of N_2O started above $300^\circ C$, consequently decreasing the formation of N_2 . The N_2O formation over the SbV/TiO_2 catalyst increased at temperatures higher than $350^\circ C$ and reached a maximum of 11% at $500^\circ C$. By contrast, a decrease of N_2O formation was observed with the addition of ceria to the SbV/TiO_2 catalyst, which showed an excellent N_2 selectivity over $SbV10Ce/TiO_2$ compared to SbV/TiO_2 and $V10Ce/TiO_2$ catalysts. It is worth noting that the $SbV10Ce/TiO_2$ catalyst showed N_2 selectivity higher than 95% up to temperatures as high as $500^\circ C$. Among all three catalysts, $SbV10Ce/TiO_2$ exhibited the best NO_x conversion and high N_2 selectivity over a wide temperature range between 220 to $500^\circ C$.

Activity of the catalysts sulfated at different temperatures

The effect of sulfation pretreatment in the oxidizing environment on low-temperature activity of the catalyst was observed in terms of NO_x conversion over a temperature range of $350 - 175^\circ C$ (Figure 5). All the samples showed 100% NO_x conversion (except 97% for S300) at temperatures $\geq 250^\circ C$ due to active redox species such as V_2O_5 and CeO_2 [11, 27]. However, the activity declined below $250^\circ C$, most likely due to the formation of both low-temperature sulfate species as well as ammonium bisulfate (ABS). Among all the samples, the S500 catalyst showed the highest activity in a low-temperature range, which suggests that the sulfates formed at $500^\circ C$ are the most favorable for NH_3 -SCR of NO_x . Contrastingly, the activity measurements at low temperatures ($\leq 250^\circ C$) for the other three samples was indistinguishable, possibly due to lower resistance against SO_2 -poisoning. However, SO_2 usage data suggests that the tendency of sulfate formation is lower on the pre-sulfated catalysts at higher temperatures ($\geq 250^\circ C$). This might be due to the repulsive interaction between SO_2 and the pre-formed sulfates. The as-prepared catalysts consumed more SO_2 during the course of the reaction. This could be due to the consumption of SO_2 by the catalyst itself as

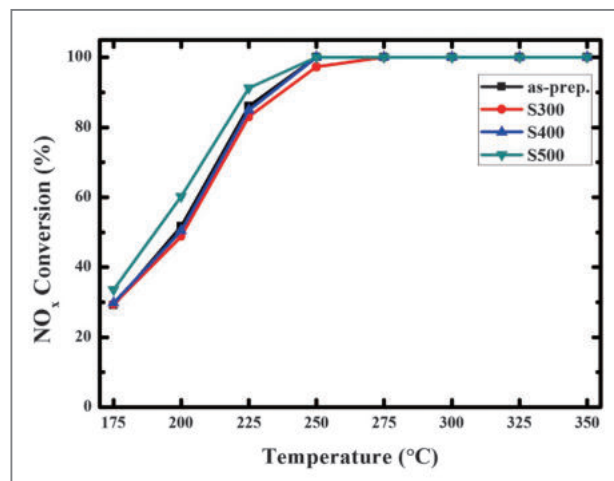


Figure 5. The effect of sulfation pretreatment temperature on NO_x conversion.

(Reaction Conditions: $[NO_x] = [NH_3] = 800$ ppm, $[O_2] = 3$ vol. %, $H_2O = 6$ vol. %, $SO_2 = 500$ ppm, N_2 balance, $GHSV = 60000$ h^{-1})

well as the formation of ammonium sulfates. However, because the initially formed sulfate species on the as-prepared catalysts are beneficial for the NH_3 -SCR, the as-prepared catalyst exhibited a slightly higher activity than that of the S300 catalyst at low temperatures. Meanwhile, when the sulfate species on the as-prepared catalyst were formed at temperatures lower than $400^\circ C$, it resulted in the as-prepared catalyst showing a lower activity than the S500 catalyst, which suggests that the sulfates formed at $500^\circ C$ are the most favorable for NH_3 -SCR.

SO_2 on-off long-term stability study

Long-term durability studies with SO_2 on-off cycles were performed under isothermal conditions at $240^\circ C$. In the presence of SO_2 and H_2O , SO_2 can be oxidized to SO_3 by O_2 and these SO_x ($SO_2 + SO_3$) compounds eventually form ammonium sulfate ($(NH_4)_2SO_4$) and/or ammonium bisulfate (NH_4HSO_4) by reacting with slipped NH_3 and H_2O [16]. This may result in the blocking of the catalytic pores and occupation of the catalytic active sites, decreasing the efficiency of the catalysts. As illustrated in Figure 6, when 6 vol% H_2O and 800 ppm SO_2 were simultaneously added to the gas reaction mixture, a

gradual decrease and recovery of NO_x conversion, which occurred every 5 h during the SO_2 on-off cycle, was observed over a 38 h continuous run. However, the NO_x removal efficiency declined at different rates for the three catalytic systems. Among all catalysts, the SbV10Ce/TiO_2 catalyst experienced the smallest decrease in NO_x conversion, from 98% to 91%. Meanwhile, the NO_x conversion of V10Ce/TiO_2 and SbV/TiO_2 catalysts decreased significantly from 91% to 75% and 93% to 60%, respectively. These results express a clear difference in the deactivation behavior of the catalysts by H_2O vapors and SO_2 . It is possible that the salt formation over the SbV/TiO_2 and V10Ce/TiO_2 catalysts occurred faster than over SbV10Ce/TiO_2 . Moreover, the SbV10Ce/TiO_2 catalyst showed higher resistance to SO_2 and water during the 38 h of continuous study. During the course of the reaction over the SbV10Ce/TiO_2 catalyst, a small amount of ammonium sulfates were formed and then removed by water in the absence of SO_2 (SO_2 off cycle), after which a gradual increase in the NO_x conversion efficiency was observed. On the other hand, larger amounts of ammonium sulfates formed over the SbV/TiO_2 and V10Ce/TiO_2 catalysts, but these deposits were

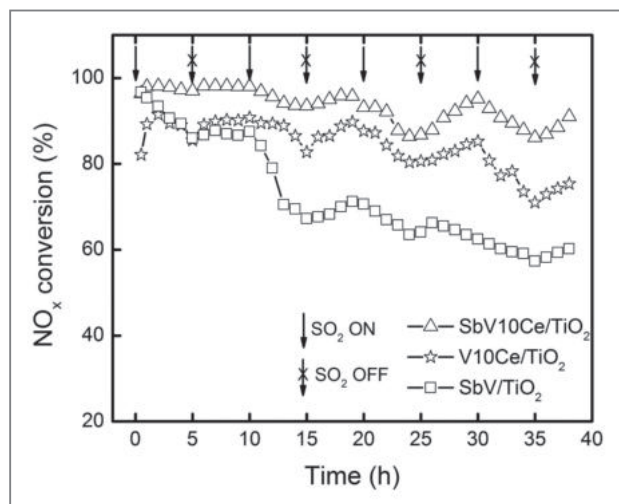


Figure 6. SO_2 on-off studies on SbV10Ce/TiO_2 , V10Ce/TiO_2 and SbV/TiO_2 samples: with SO_2 and H_2O at 240°C . (Reaction conditions: 800 ppm NO_x , 800 ppm NH_3 , 3 vol% O_2 , 6 vol% H_2O , 800 ppm SO_2 , GHSV = $60,000 \text{ h}^{-1}$).

inadequately removed by water in the absence of SO_2 , leading to the continuous deactivation of those catalysts. The SO_2 -TPD analysis of the SbV10Ce/TiO_2 catalyst is in good agreement with the results above, indicating that less SO_2 adsorption associated with the SbV10Ce/TiO_2 catalyst is a reflection of its strong resistance to SO_2 and subsequent salt formation. Consequently, it appears that a SbV10Ce/TiO_2 catalyst offers increased resistance against SO_2 and H_2O during a SO_2 on-off long-term stability test.

Activity of the extruded monolithic catalyst

The activity of the V-Sb-Ce/TiO_2 monolithic catalyst (Mono-VSCT, full scale image shown in Figure 7, was investigated for NO_x reduction with ammonia at a temperature range of 150 to 500°C . Figure 8(a) shows the NO_x conversion with temperature over Mono-VSCT, and this was compared with the conversion of V-W-TiO_2 commercial monolithic catalyst (Mono-VWT) (supplied by ESKO Co., Ltd., Republic of Korea). In the case of Mono-VSCT, NO_x reduction activity under a gas stream of 1300 ppm NO_x , 1300 ppm NH_3 , 15 vol. % O_2 , 4 vol. % H_2O and 20 ppm SO_2 was indicated over a wide temperature range. An NO_x conversion of higher than 80% was attained for the Mono-VSCT in the temperature range of 180 to 500°C . In comparison to the Mono-VWT sample (chemical composition determined by XRF is as follows: 2 wt.% V_2O_5 , 5 wt.% WO_3 , 80 wt.% TiO_2 , binders), higher NO_x conversions were observed for the Mono-VSCT sample at temperatures below 300°C . The selectivity of NO_x to N_2 and N_2O is displayed in Figure 8(b). One can see that the Mono-VSCT showed almost 100% N_2 selectivity from 150 to 350°C . However, there is a slight increase of N_2O formation at temperatures above 400°C , which is a typical behavior of vanadia containing catalysts. A maximum of 19% N_2O selectivity was observed for the Mono-VSCT at 500°C . Based on the results above, the NO_x reduction activity of the Mono-VSCT was considerably higher than that of the commercial Mono-VWT over a wide temperature range between 150 and 450°C .

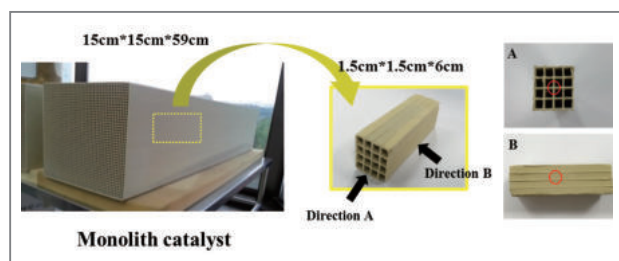


Figure 7. A full scale view photograph of the Mono-VSCT catalyst.

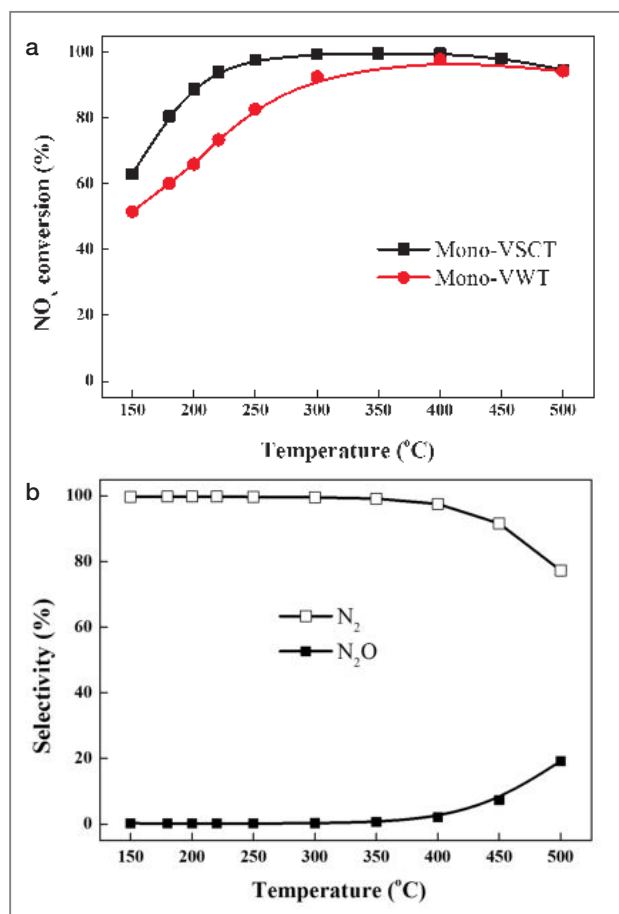


Figure 8. (a) NO_x conversion of Mono-VSCT vs. Mono-VWT catalysts calcined at 500°C for 5 h and (b) N₂ and N₂O selectivity of Mono-VSCT catalyst.

(Reaction conditions: [NO_x]=[NH₃]=1300 ppm, [O₂]=15 vol.%, H₂O = 4 vol.%, [SO₂]=20 ppm and N₂ balance, GHSV : 10,000 h⁻¹).

Regeneration cycles of the extruded monolithic catalyst

In order to examine the stability of the Mono-VSCT, deactivation-regeneration experiments were carried out for 20 successive deactivation and regeneration cycles at 220°C with a feed gas stream consisting of NO_x/NH₃ = 1 (1300 ppm of each gas), 15 vol.% O₂, 4 vol.% H₂O, 800 ppm SO₂ and N₂ balance. In each cycle, the Mono-VSCT catalyst was deactivated to 75% NO_x conversion and then regenerated by water and N₂ at 400°C for 2 h. The result, represented in Figure 9, indicates a series of successive deactivation and regeneration cycles of the Mono-VSCT sample. In the process of deactivation, each cycle indicated a decrease of NO_x conversion from 90 to 75% in a span of around 10 h. This loss was due to the deposition of ammonium sulfates/bisulfates on the active sites of the catalyst leading to the blocking of the catalyst pores, eventually decreasing the NO_x conversion. However, after regenerating the catalyst with water vapor and N₂ gas at 400°C for 2 h, the activity of the catalyst completely recovered to its initial NO_x conversion. This gives clear evidence that this catalyst was only

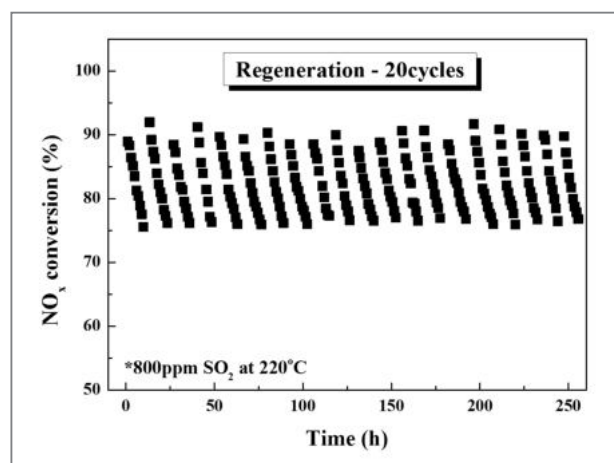


Figure 9. Deactivation and Regeneration cycles of Mono-VSCT catalyst.

(Deactivation reaction Conditions: [NO_x] = [NH₃] = 1300 ppm, [O₂] = 15 vol.%, H₂O = 4 vol.%, SO₂ = 800 ppm and N₂ balance and GHSV = 10,000 h⁻¹ at 220°C;

Regeneration Conditions : 15% O₂, 4 vol.% of H₂O and N₂ balance and GHSV = 10,000 h⁻¹ at 400°C during 2 h).

temporarily deactivated under a high amount of sulfur and water, not poisoned permanently. This may also suggest that the formed ammonium sulfates/bisulfates are easily decomposed at 400°C and the catalysts can be fully recovered to the initial state. 20 successive deactivation and regeneration cycles signify the stability of the catalyst. The long-term durability and regenerative properties of this catalyst are favorable for realistic application for the reduction of NO_x from exhaust containing a high amount of SO₂.

Specific characterization of the catalysts by XRD, XANES, and TEM-tomography

Figure 10 illustrates the XRD patterns for the fresh and sulfated catalysts along with the possible cerium sulfates. The as-prepared catalyst exhibited characteristic CeO₂ [PDF-ICDD 81-0792] and TiO₂-anatase [PDF-ICDD 86-1157] peaks. The peaks corresponding to Sb₂O₃ and V₂O₅, could not be detected, possibly due to the nominal addition and good dispersion of the oxides. Furthermore, no CeO₂ peak could be observed in any of the sulfated catalysts, which could suggest preferential sulfation of ceria lessening its crystallinity [8]. It is also important to note that none of the possible cerium sulfates could be observed in the sulfated samples. This implies

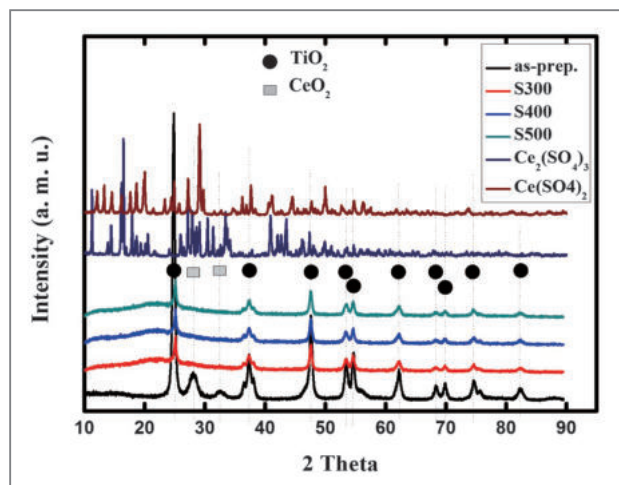


Figure 10. XRD patterns of the catalysts, as-prepared and sulfated at different temperatures along with commercial Ce₂(SO₄)₃, and Ce(SO₄)₂

that the formed sulfates were either too low in quantity to be detected by XRD or amorphous in nature.

XANES spectra of the Ce L₃ edge for CeVO₄, CeO₂ pure compounds, and SbV10Ce/TiO₂ catalyst are displayed in Figure 11. The oxidation state of cerium ions can be deduced from the shape of the edge and the position of the inflection point. The Ce L₃ edge spectra for Ce³⁺ compounds (CeVO₄ used as reference) exhibited a strong absorption line at the absorption edge (WL: white line) due to a 2p_{3/2} → (4f^l)5d* electron transition (d* represents an excited electron in the d orbital). CeO₂, used as a reference compound for Ce⁴⁺, presented a double white line. These two peaks correspond to the 2p_{3/2} → (4f^lL)5d* and (4f⁰)5d* transitions (L represents that an electron from an O 2p orbital is transferred to a Ce 4f orbital). The reference CeO₂ compound Ce L₃ edge spectra absorption main edges showed two white line peaks located at 5732 and 5738 eV (Figure 11), which corresponds to the Ce⁴⁺ oxidation state. However, the CeVO₄ absorption main edge showed one white line observed at 5727 eV, which corresponds to the Ce³⁺ oxidation state [9]. Moreover, a weak absorption pre-edge feature at 5719 eV was observed for all the catalysts. Figure 9 reveals that the freshly prepared SbV10Ce/TiO₂ catalyst shows more Ce⁴⁺ species than Ce³⁺ species. As the SO₂ treatment temperatures increased, the intensity of the absorption edge peak at low energy increased. This corresponds to the white line of the Ce³⁺ oxidation state. Consequently, the formation of more active Ce (III) sulfate species on the surface of SbV10Ce/TiO₂ catalysts was observed for the SO₂ treated catalysts, where high NO_x conversions appeared at low temperatures below 220°C. From this result, it was speculated that the S500 catalyst showed highest catalytic activity for NH₃-SCR at low temperatures due to the abundant presence of active and beneficial Ce (III) sulfate species. The XANES spectra confirm the speculation that the Ce (III) sulfate species in the S500 catalyst promote NH₃-SCR activity at low temperatures by improving the active oxygen species and acidic sites [10].

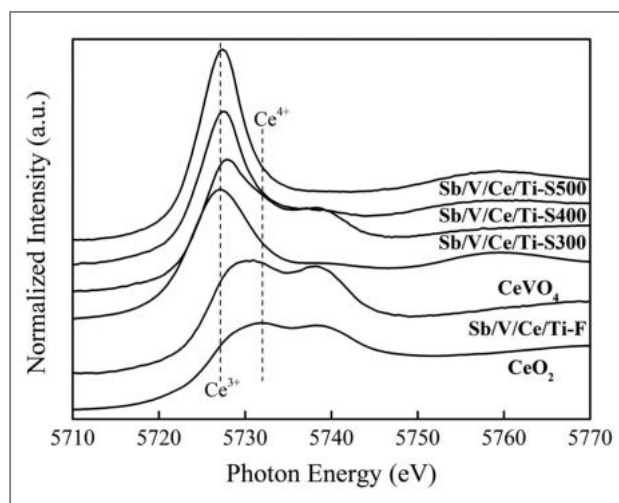


Figure 11. Ce L_{3} edge XANES spectra of sulfated SbV10Ce/TiO₂ catalysts at different temperatures, fresh SbV10Ce/TiO₂, CeVO₄ and CeO₂ samples.

Figure 12 demonstrates the TEM-tomography images of the fresh SbV10Ce/TiO₂ catalyst. The fine dispersion of the CeO₂ nano-crystallites onto the TiO₂ support is indicated in the 3D image of tomography. It is also important to note that the CeO₂ nano-crystallites observed were between the sizes of 5 to 10 nm. As the sulfation treatment temperature of the SbV10Ce/TiO₂ catalyst increased to 500°C, the transformation of crystalline CeO₂ into non-crystalline phase of cerium sulfate species was observed and confirmed by selective area electron diffraction (SAED) patterns of the fresh and sulfated catalysts as shown in Figure 12. This could be the result of the formation of beneficial Ce (III) sulfate species on the catalyst surface.

Based on our characterization and activity results at low temperature (225°C), catalytic performance of the sulfated samples can be summarized as shown in Figure 13. Excess ammonia adsorption onto low-temperature sulfated catalysts can inhibit direct contact of gaseous NO with the activated NH₃ and/or block the active redox species. However, its activity might be the result of the reaction between adsorbed or gaseous NO and activated NH₃, as it showed the highest NO desorption compared to the other sulfated samples. Moreover, since all the CeO₂

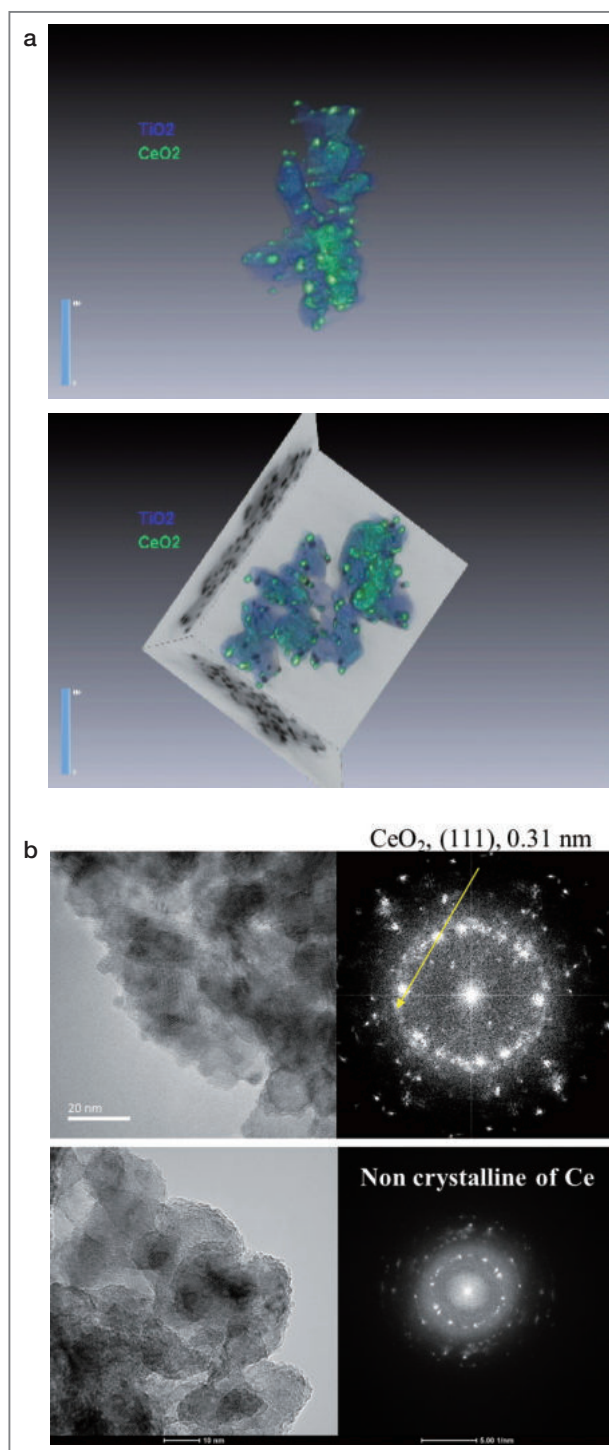


Figure 12. TEM images of fresh and sulfated SbV10Ce/TiO₂ (500°C) catalyst
(a) TEM-tomography (b) SAED patterns.

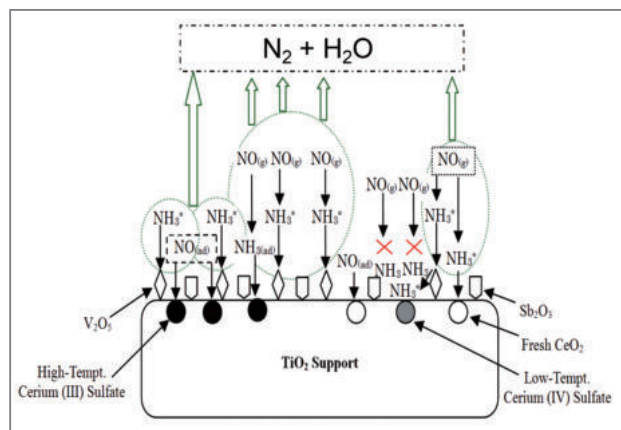


Figure 13. Proposed NH_3 -SCR mechanism on the $\text{SbV}_{10}\text{Ce}/\text{TiO}_2$ catalyst.

could not be sulfated at low temperature by sulfation pretreatment, NO reduction could also occur through the reaction between gaseous NO and NH_3 activated by CeO_2 and/or V_2O_5 species. In the case of the high-temperature sulfated sample, a sufficiently high amount of NH_3 and NO adsorption along with more reducible species resulted in the highest achievable activity among the fresh and other sulfated catalysts.

Conclusions

Various ceria-loaded $\text{Sb-V}_2\text{O}_5/\text{TiO}_2$ catalysts were developed for the reduction of NO_x with NH_3 , especially in the temperature region between 180–500°C. The addition of 10% ceria to a $\text{Sb-V}_2\text{O}_5/\text{TiO}_2$ catalyst showed excellent NO_x conversion with 80% in a wide temperature window of 200–450°C. This catalyst exhibited superior N_2 selectivity compared to a $\text{Sb-V}_2\text{O}_5/\text{TiO}_2$ or $\text{V}_2\text{O}_5\text{-10Ce}/\text{TiO}_2$ catalyst. The 10% ceria-loaded $\text{Sb-V}_2\text{O}_5/\text{TiO}_2$ catalyst also exhibited strong resistance to 6% H_2O and 800 ppm SO_2 at low temperatures around 220°C and possessed high NO_x conversion (90%) and N_2 selectivity (100%). The $\text{Sb-V}_2\text{O}_5/\text{TiO}_2$ sulfated catalysts showed superior low temperature NH_3 -SCR activity by SO_2 treatment at high temperatures. Higher than 90%

of NO_x conversion was achieved at low temperatures around 200°C for the catalyst sulfated at 500°C (S500). The XANES spectra of Ce L₃ and M_{4,5} edge showed the formation of a more active Ce (III) sulfate species on the S500 catalyst, which resulted in the increase of the surface active oxygen species and acid sites. The $\text{SO}_2 + \text{O}_2$ DRIFTS spectra of the S500 catalyst showed a more bulk-like sulfate species attributed to the Ce (III) sulfates. In addition, the $\text{SO}_2 + \text{O}_2$ treatment of $\text{Sb-V}_2\text{O}_5/\text{TiO}_2$ catalysts at high temperatures facilitated the formation of more acid sites. Consequently, the enhancement of Lewis and Brønsted acid sites for S500 was confirmed by *in situ* DRIFTS spectra. Moreover, the oxidation of NO to NO_2 was favored on S500 catalysts. As a result, formed NO_2 species on S500 catalysts could react with the adsorbed NH_3 to enhance the low temperature NH_3 -SCR activity.

Note

This article and images are cited from our published articles in: *Appl. Catal. B* 2013; 142-143: 705–717; *Appl. Catal. B* 2014; 152-153: 28–37; and *Chem. Eng. J.* 2015; 275: 142-151.

References

- [1] Bosch H, Jassen F. *Catal. Today* 1988; 2: 369–379.
- [2] Busca G et al. *Appl. Catal. B* 1998; 18: 1–36.
- [3] Ha HP et al. *Appl. Catal. B* 2008; 78: 301–308
- [4] Ha HP et al. EP1904227
- [5] Lee KJ et al. *Appl. Catal. B* 2013; 142-143: 705–717
- [6] Maqbool MS et al. *Appl. Catal. B* 2014; 152-153: 28–37
- [7] Kumar PA et al. *Chem. Eng. J.* 2015; 275: 142-151
- [8] Gu T et al. *Catal. Commun* 2010; 12: 310–313
- [9] Padežnik JG et al. *Thin Solid Films* 2004; 446: 117-123
- [10] Chang H et al. *Environ. Sci. Technol.* 2013; 47: 5294-5301

Feature Articles

Heavy Metal-Free Copper-Indium-Selenide Quantum Dot Solar Cells



Min Jae KO

Photo-Electronic Hybrids Research Center
National Agenda Research Division
mjko@kist.re.kr

Introduction

Over the last two decades, the synthesis of colloidal quantum dots (QDs) [1, 2] and their potential applications in third-generation photovoltaic devices [3, 4] have received significant attention due to their unique optoelectronic properties, such as their band gap tunability, high absorption coefficient, slow hot electron cooling, and potential for multiple exciton generation. Furthermore, colloidal QDs can be easily solution-processed, allowing for inexpensive device fabrication. These properties have led to the recent development of highly efficient QD solar cells, including depleted heterojunction solar cells using PbS QDs [5] and QD-sensitized solar cells (QDSCs) using $\text{CdSe}_x\text{Te}_{1-x}$ [6], which have achieved conversion efficiencies of 9.2 and 8.55%, respectively. However, these devices, like many others, contain toxic cadmium- or lead-chalcogenides, which may limit commercial applications, particularly for portable devices. Environmentally friendly Cu-In-S and Cu-In-Se (CISe) QDs have been under development as alternatives to these toxic materials [7-9]. However, there is still a gap between the performance of these QDSCs and that of conventional cadmium- and lead-chalcogenide QD-based devices, which might be due to a lack of understanding about the control of the carriers in these I-III-VI materials-based QDSCs.

The focus of this article is on KIST's efforts in developing highly efficient heavy metal-free QD solar cells based on CISe nanocrystals. We

have introduced a new synthetic process to produce NIR-absorbing CISE QDs for use in applications requiring completely heavy metal-free QDSCs [10]. Our facile and scalable method allows control over the size and composition of the QDs, which are critical parameters for tuning the optoelectronic properties of CISE QDs. The effect of quantum-confinement on the optical and electronic properties of CISE QDs and the resulting PV performance were systematically investigated. In addition, we optimized the photovoltaic performances of CISE QDSCs with controlled ZnS overlayers [11]. The physical and chemical nature of the overlayers was determined and its influence on the optical, energetic, and kinetic characteristics of the photoanode was investigated, in particular, by focusing on the interfacial and non-radiative recombination in the QDSCs.

Results and Discussion

CISE QDs were synthesized by the reaction between metal iodides and oleylammonium selenocarbamate in oleylamine as a coordinating solvent. Notably, oleylammonium selenocarbamate, produced by the addition of a carbonyl group to form an amide bond between selenium and oleylamine, was selected as the selenium precursor. Because of the high basicity of selenocarbamate, the Lewis acid-base reaction between the precursors was so effective that the nucleation of QDs occurred at a very low temperature. When the growth temperature was elevated from 80°C to 270°C, the size of the QDs increased from 2.5 nm to 10 nm and the composition changed from $\text{CuIn}_{2.5}\text{Se}_4$ to $\text{CuIn}_{1.1}\text{Se}_{2.1}$ simultaneously. Transmission electron microscopy (TEM) images (Figure 1) of CISE QDs show the narrow size distribution with a standard deviation of 5–10%, with the exception of the largest-sized ones.

The X-ray diffraction (XRD) pattern of the QDs indicated that their crystal structure was identical to a tetragonal chalcopyrite structure (JCPDS #40-1487).

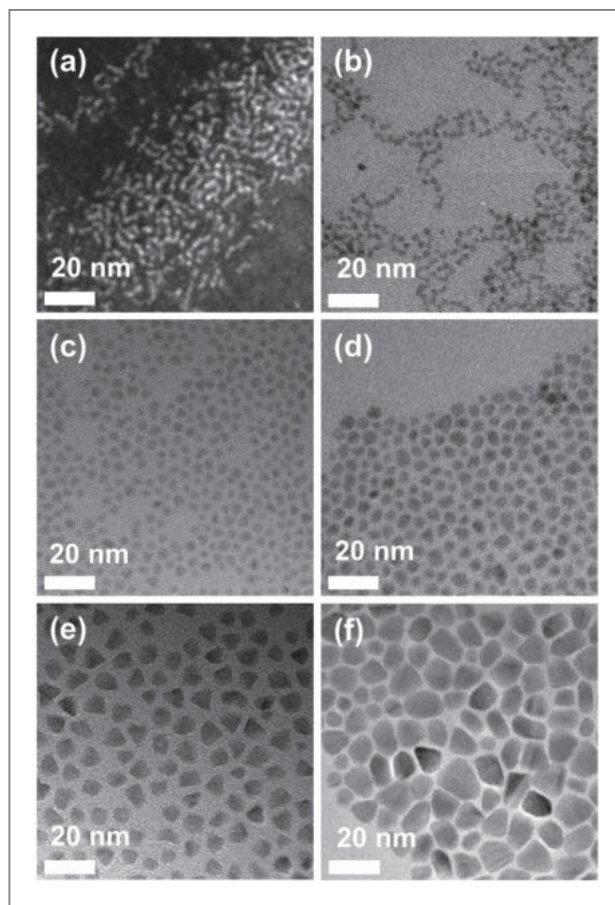


Figure 1. (a) Scanning transmission electron microscope (STEM) image of 2.5 nm CISE QDs, and TEM images of (b) 3 nm, (c) 4 nm, (d) 5 nm, (e) 7 nm, and (f) 10 nm CISE QDs.

Absorption by the CISE QDs covered the whole visible wavelength range (Figure 2), suggesting the possibility for utilization of the entire solar spectrum for PV device applications. The distinct shoulder in the absorption spectrum is also indicative of the uniform size distribution of the QDs. The band gap could be widely tuned in the NIR region by varying the size and composition of the QDs. The optical band gap was blue-shifted from the band gaps of bulk $\alpha\text{-CuInSe}_2$ (1.04 eV) and $\beta\text{-CuIn}_3\text{Se}_5$ (1.2 eV) owing to the quantum-confinement effect (Figure 3a).

In addition, the calculation using a simple particle in a sphere with a finite potential barrier model shows that

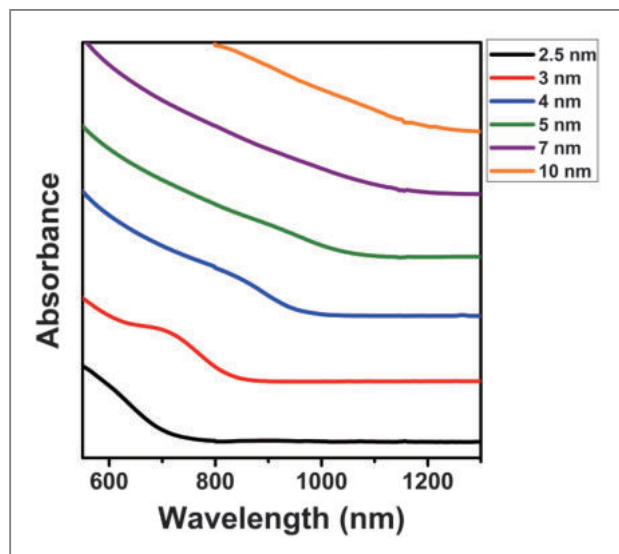


Figure 2. Absorption spectra of the CISE QDs.

although the band gap of bulk CuIn_3Se_5 is higher than that of bulk CuInSe_2 , the small effective mass of electrons and holes in CuInSe_2 crystal allows for more size-dependent band gap and band alignment tunability (Figures 3a and 3b). These results imply that the quantum-confinement effect plays a more significant role in determining the band energy level variation than does composition in this strong quantum-confinement regime.

Figure 3b shows the size-dependent band edge alignment of QDs. The conduction band minimum (CBM) of the QDs was taken by the first reduction peak position in the CV, and the valence band maximum (VBM) was determined from the CBM and the optical band gap. The experimentally measured energy alignment of a CISE QD was finely controlled with respect to its size and matched well with the theoretical value. Compared to the CBM of TiO_2 (-4.3 eV vs. vacuum), that of bulk CISE or QDs larger than ~ 5 nm is positioned in the lower electron energy level. Consequently, the injection of photo-generated electrons from CISE to TiO_2 is not thermodynamically favorable in bulk, which is the main reason why efficient QDSCs employing CISE QDs have not been realized yet. However, with a decrease in

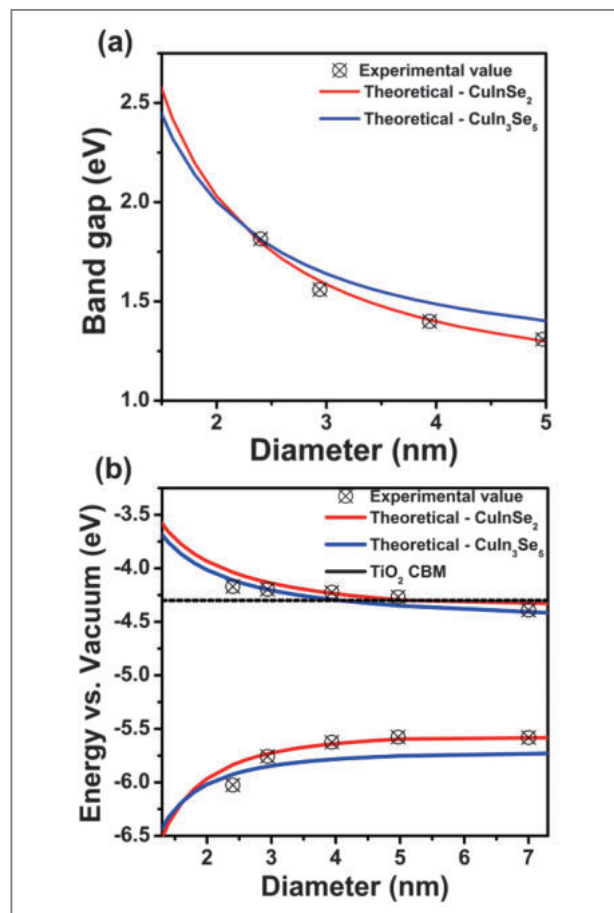


Figure 3. (a) The comparison of the band gaps obtained from the absorption spectra (black dots) with the calculated band gaps (lines). (b) The band edge alignment of CISE QDs obtained from the absorption spectroscopy and cyclic voltammetry (black dots). Experimental values matched well with the theoretical calculation for CuInSe_2 (red line) and CuIn_3Se_5 (blue line). The black line represents the CBM of TiO_2 .

the size of the CISE QDs, the CBM shifted toward the vacuum level, owing to the quantum-confinement effect.

We employed the CISE QDs as the photosensitizer in QDSCs. Figure 4a shows the dependence of the IPCE spectra of the CISE QDSCs on QD size. The absorption range in the IPCE spectra clearly shows the quantum-confinement effect. The QDSC with 2.5 nm QDs exhibited an onset wavelength of 750–800 nm and could not absorb photons in the NIR region. However, the absorption range was greatly extended even by a small increase in the QD size. QDSCs with 3, 4, and

5 nm QDs exhibited onset wavelengths of about 920, 1080, and 1170 nm, respectively. The onset wavelength increased to about 1200 nm for the 7 and 10 nm QDs. However, the corresponding QDSCs showed very low IPCE values, which may be due to unfavorable energetics for electron injection. In addition, the relatively large size of the QDs could have led to the sparse adsorption onto the mesoporous TiO₂ film, resulting in increased electron recombination with the electrolyte.

The photocurrent density–voltage (J – V) characteristics of the QDSCs under illumination are shown in Figure 4b. The trends in the short-circuit current (J_{sc}) matched well with the IPCE data. As mentioned above, larger QDs show a wider range of light absorption; however, they are unfavorable for electron

injection into the TiO₂ CB. Due to this trade-off, the performance of QDSCs was optimized with 4 nm QDs, yielding a conversion efficiency of 4.30%. The highest open-circuit voltage (V_{oc}) observed for the 4 nm QDs can be attributed to the large amount of injected electrons resulting from the suitable energetics toward light absorption and injection of electrons into the TiO₂ CB. It is noteworthy that the 4 nm QDs exhibited the highest J_{sc} as well as the highest V_{oc} , although the energy difference between their CBM and that of TiO₂ was relatively small.

In general, the surface of QD-sensitized TiO₂ films is treated with a standard successive ionic layer adsorption and reaction ZnS (SILAR) process in order to suppress the electron recombination between the photoanode and the redox couple in the electrolytes. Firstly, we repeated the ZnS SILAR cycles 3 times according to the conventional method [12]. In addition, the number of SILAR cycles was increased 6–10 times to study the resulting photovoltaic properties. The J – V curves of the QDSCs with respect to the number of SILAR cycles are shown in Figure 5a. Notably, all photovoltaic parameters were greatly enhanced after 3 SILAR cycles, with a conversion efficiency roughly 2.3 times greater than the untreated sample. This effect was even more pronounced as the number of cycles increased further; the positive effects reached a maximum of 7 cycles, yielding an enhancement of conversion efficiency of about 40% over the control sample (i.e., 3 cycles). Figure 5b shows the external quantum efficiency (EQE, η_{Q}) spectra of the QDSCs as a function of wavelength. The QDSCs treated with 7 SILAR cycles exhibited the highest η_{Q} values and the broadest spectrum, with coverage including the NIR region due to the low optical band-gap of the CISE QDs. A conversion efficiency of 8.10% was achieved for the best device in this study. This is a remarkable value for a heavy metal-free QD solar cell and is, in fact, comparable to the best conversion efficiency ever observed for QDSCs.^[14] Again, this effect is likely due to a combination of both the low optical band gap that allows for effective light absorption over a broad range of

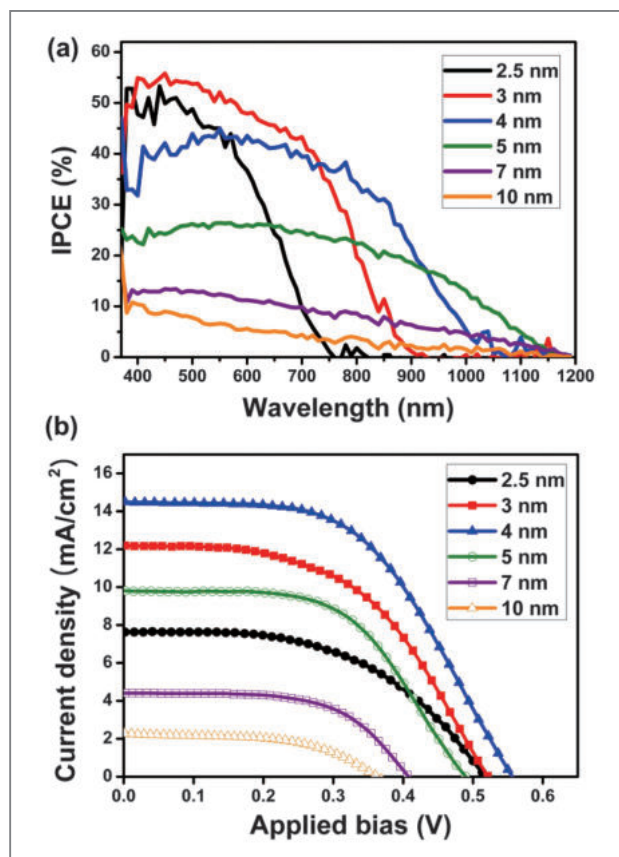


Figure 4. (a) IPCE spectra and (b) J – V characteristics under illumination (one sun light intensity with AM 1.5 G filter) of the CISE QDSCs with various-sized QDs.

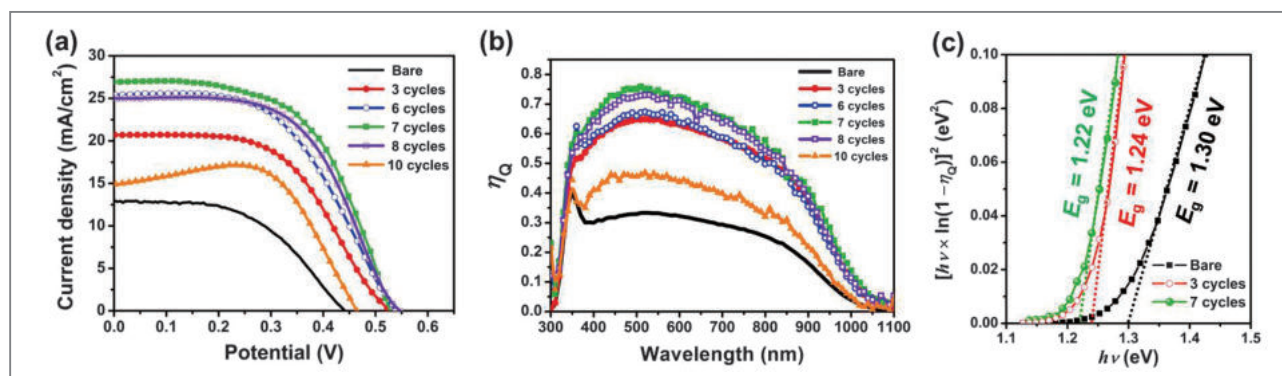


Figure 5. (a) J - V characteristics under illumination (one sun light intensity with AM 1.5G filter) and (b) EQE values (η_{EQ}) for CISE QDSCs with respect to the number of ZnS SILAR cycles.

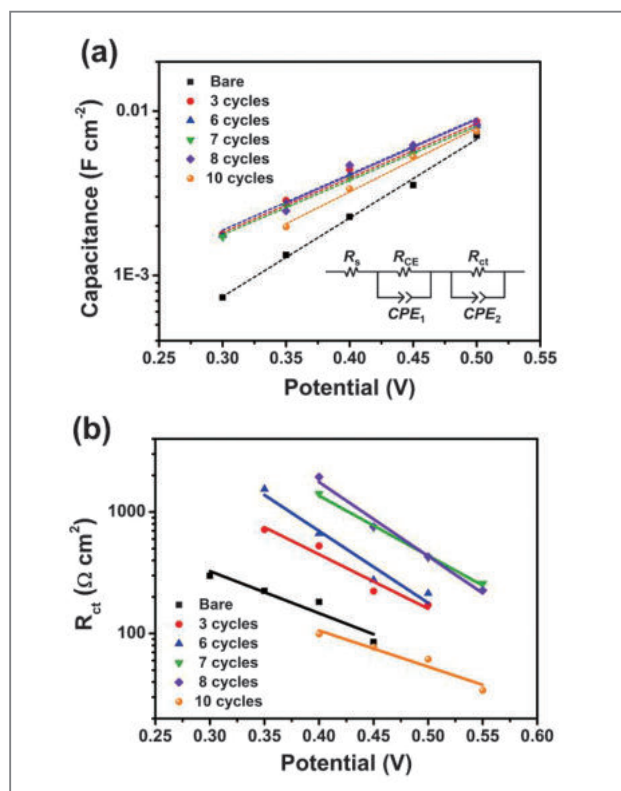


Figure 6. (a) Chemical capacitance and (b) recombination resistance of the CISE-sensitized TiO₂ electrodes with respect to the number of ZnS SILAR cycles, evaluated from impedance spectra taken in the dark state. The inset of (a) shows the equivalent circuit model.

wavelengths as well as the optimized surface passivation of the ZnS overlayers.

The influence of thick ZnS overlayers on energetic and kinetic characteristics of the produced electrodes was investigated through electrochemical impedance analysis in a dark state at bias potentials from -0.30 to -0.55 V (Figure 6). As shown in Figure 6a, the electrodes with ZnS overlayers exhibited higher C_{μ} values than the bare electrode at the same bias potential, meaning that the conduction band (CB) potential of the electrode became more positive. However, the actual number of SILAR cycles seemed to make little difference. A positive shift in the CB potential of the photoanode generally led to a decrease in the V_{OC} of the resulting solar cells. However, the V_{OC} in the J - V characteristics increased after the overlayers were added. In addition, this effect increased with overlayer thickness, even though the CB potential of the photoanode was not affected. Therefore, this is likely the result of other factors, such as the flux of injected electrons and changes in electron recombination between the photoanode and the redox couple in the polysulfide electrolyte. Indeed, R_{ct} clearly increased with the number of SILAR cycles up to a maximum of 7, as shown in Figure 6b, indicating a reduced electron recombination rate. Apparently, the thick ZnS overlayers do not affect the energetics of the system, but do enhance the kinetics, which accounts for the improved efficiency compared to the control sample.

Conclusions

Our new synthetic method produced composition- and size-controlled CISE QDs with a narrow size distribution. Depending on the QD size, the band energy alignment and light absorption range of the CISE QDSCs could be fine-tuned in the quantum-confinement regime. The best PV performance was achieved for 4 nm-sized CISE QDSCs by optimizing the energetics of the QDs toward effective light absorption and injection of electrons. In addition, a highly efficient heavy metal-free CISE QDSC was developed with precisely controlled ZnS overlayers. The conversion efficiency of the produced QDSC was enhanced by about 40% when the thickness of the overlayer was increased to twice that of a conventional one. The impedance data revealed that interfacial electron recombination with the electrolyte was significantly reduced by introducing a thick ZnS overlayer, explaining the significant enhancement in photovoltaic performance. This yielded a remarkable conversion efficiency of 8.10% under one sun illumination. The results exhibit a great advancement in technology and facilitate important insight into the development of highly efficient heavy metal-free QD solar cells.

Note

This article and images are drawn from “Copper-indium-selenide quantum dot-sensitized solar cells” in *Phys. Chem. Chem. Phys.* (2013), Vol. 15, pp. 20517-20525, and “Highly Efficient Copper-Indium-Selenide Quantum Dot Solar Cells: Suppression of Carrier Recombination by Controlled ZnS Overlayers” in *ACS Nano* (2015), Vol. 9, pp. 11286-11295.

References

- [1] Murray CB, Norris DJ, Bawendi MG. *J. Am. Chem. Soc.* 1993; 115: 8706-8715.
- [2] Peng X, Manna L, Yang W, Wickham J, Scher E, Kadavanich A, Alivisatos AP. *Nature* 2000; 404: 59-61.
- [3] Robel I, Subramanian V, Kuno M, Kamat PV. *J. Am. Chem. Soc.* 2006; 128: 2385-2393.
- [4] Nozik AJ, Beard MC, Luther JM, Law M, Ellingson RJ, Johnson JC. *Chem. Rev.* 2010; 110: 6873-6890.
- [5] Labelle AJ, Thon SM, Masala S, Adachi MM, Dong H, Farahani M, Ip AH, Sargent EH. *Nano Lett.* 2015; 15: 1101-1108.
- [6] Zhao K, Pan Z, Mora-Seró I, Cánovas E, Wang H, Song Y, Gong X, Wang J, Bonn M, Bisquert J. *J. Am. Chem. Soc.* 2015; 137: 5602-5609.
- [7] Panthani MG, Stolle CJ, Reid DK, Rhee DJ, Harvey TB, Akhavan VA, Yu Y, Korgel BA. *J. Phys. Chem. Lett.* 2013; 4: 2030-2034.
- [8] McDaniel H, Fuke N, Makarov NS, Pietryga JM, Klimov VI. *Nat. Commun.* 2013; 4: 2887.
- [9] Li W, Pan Z, Zhong X. *J. Mater. Chem. A* 2015; 3: 1649-1655.
- [10] Yang J, Kim JY, Yu JH, Ahn TY, Lee H, Choi TS, Kim YW, Joo J, Ko MJ, Hyeon T. *Phys. Chem. Chem. Phys.* 2013; 15: 20517-20525.
- [11] Kim JY, Yang J, Yu JH, Baek W, Lee CH, Son HJ, Hyeon T, Ko MJ. *ACS Nano* 2015; 9: 11286-11295.
- [12] Pan Z, Mora-Seró I, Shen Q, Zhang H, Li Y, Zhao K, Wang J, Zhong X, Bisquert J. *J. Am. Chem. Soc.* 2014; 136: 9203-9210.



Feature Articles

Achieving Selective and Efficient Electrocatalytic Activity for CO₂ Reduction Using Immobilized Silver Nanoparticles



Byoung Koun MIN

Clean Energy Research Center
National Agenda Research Division
bkmin@kist.re.kr



Yun Jeong HWANG

Clean Energy Research Center
National Agenda Research Division
yjhwang@kist.re.kr

Introduction

Atmospheric concentrations of carbon dioxide, a greenhouse gas, are ever increasing due to the continued use of traditional fossil fuels, leading to adverse changes to the global climate [1, 2]. In an effort to mitigate world-wide dependence on fossil fuels, and thus, CO₂ emissions, there is an increasing emphasis on the development of renewable energy sources. One such approach is the conversion of carbon dioxide to a reusable carbon form, in other words, a sustainable carbon recycling system [3, 4]. Among various methods proposed for CO₂ conversion, electrochemical CO₂ reduction in aqueous solutions has attracted considerable attention since it is environmentally clean and can be combined with renewable energy sources, such as solar and wind energies, to store these resources in the form of chemical energy [5]. However, electrochemical CO₂ reduction reaction suffers from poor efficiency for several reasons, including the requirement of a large overpotential, difficulty in controlling selectivity, and competition with hydrogen evolution reaction in aqueous environments [6]. Therefore, it is necessary and important to design a new catalyst with high efficiency and selectivity.

Gold, silver, and copper have been identified as promising CO₂ reduction reaction electrocatalysts [7]. To improve reactivity, the surfaces of bulk polycrystalline metal catalysts have been modified to form nanostructures in order to improve catalytic activity for CO₂ reduction reaction. For example,

oxide-derived Au nanoparticles or Ag nanoporous materials have demonstrated low overpotentials and high stability for CO production, where high activity appears to relate to the high-index facets of the curved surfaces [8, 9].

In this study, in order to synthesize highly efficient nanostructured electrocatalysts for CO₂ conversion to CO, we developed a wet chemistry-based direct one-pot synthesis of Ag nanoparticles on a carbon support using an anchoring agent (cysteamine) and successfully controlled uniform particle sizes. Three different sized silver particles (3, 5, and 10 nm) supported on carbon (nano-sized Ag/C) were evaluated for electrochemical CO₂ reduction reaction in an aqueous environment, and the influence of the anchoring agent on the CO₂ reduction activity was investigated. We found that particles with a diameter of 5 nm had a high activity, enhanced durability, and maximum Faradaic efficiency (84.4%) for the CO₂ to CO electrochemical conversion. We propose that the anchoring agent modifies the spatial spin density of the Ag nanoparticles, which decreases the overpotential for CO₂ to CO reduction by DFT calculations.

Immobilized Ag nanoparticle synthesis with an anchoring agent

Ag nanoparticles of three different sizes were easily synthesized by using an Ag precursor, carbon black, and cysteamine. The size of the Ag nanoparticles was 3.4 ± 0.6 nm when synthesized at 160°C for 1 hour (denoted as 3 nm Ag/C), 5.0 ± 0.9 nm at 160°C for 3 hours (denoted as 5 nm Ag/C) and 10.6 ± 2.8 nm at 200°C for 1 hour (denoted as 10 nm Ag/C), as shown in Figure 1. Without cysteamine, Ag particles cannot be directly grown on the carbon support and nanoparticle size cannot be controlled because cysteamine molecules help to anchor nanoparticles in the initial nucleation step [10, 11].

To investigate the role of cysteamine, X-ray photoelectron spectroscopy (XPS) was conducted on

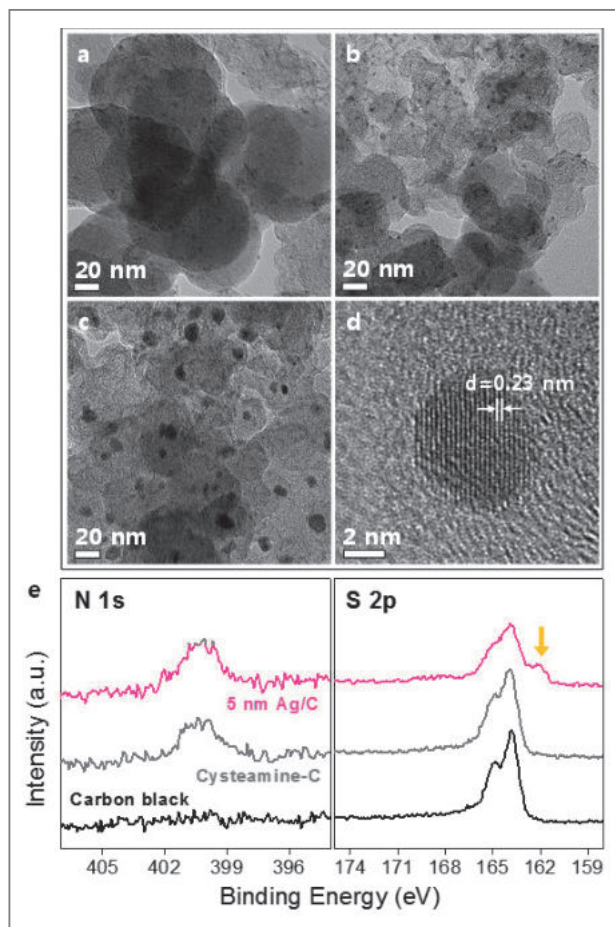


Figure 1. TEM image of: a) 3 nm, b) 5 nm and c) 10 nm sized Ag nano-particles directly synthesized on carbon support. d) HR-TEM image of 5 nm Ag/C. e) XPS spectra of 5 nm Ag/C, Cysteamine-C and carbon black for N 1s and S 2p.

the carbon black, cysteamine-treated carbon (denoted as Cysteamine-C) and prepared Ag nanoparticles/C (Figure 1e). This figure shows a clear N 1s peak for the Cysteamine-C and 5 nm Ag/C while its absence for carbon black indicates that cysteamine was immobilized on the carbon support. On the other hand, Ag/C particles commonly showed additional S 2p peaks (see arrow in Figure 1e) unlike those of carbon black and Cysteamine-C. The additional S 2p_{3/2} peak possessed binding energy at 162.1 eV, associated with an Ag-S bond [12] resulting from the interaction of the cysteamine with the Ag surface. The carbon black as purchased also

showed S 2p peaks remnant from its production process [13].

Electrochemical CO₂ reduction with nanoparticulated Ag/C and Ag foil

The electrochemical CO₂ reduction reaction was performed using the prepared 3, 5, and 10 nm Ag/C samples, and all showed enhanced catalytic activity for CO production compared with the polycrystalline Ag foil (Figure 2a). This figure shows the *iR*-corrected potential-dependent CO partial current densities, which were measured at the steady-state current density by chronoamperometry. The CO partial current density of 5 nm Ag/C showed the highest values at the low cathodic potential region (-0.3 ~ -0.9 V vs. RHE). Meanwhile, the 3 nm and 10 nm Ag/C started to show CO partial current density at a higher biased potential region than 5 nm Ag/C, while Ag foil had an even larger cathodic onset potential meaning a larger required overpotential for CO₂ reduction reaction.

In order to compare the required overpotentials further, we obtained overpotentials at a fixed current density and overpotentials-dependent CO partial current density (Figure 2b). The thermodynamic reduction potential for CO₂ to CO was -0.11 V vs. RHE. All of the prepared Ag/C samples showed a noticeable decrease in overpotential and 5 nm Ag/C showed the largest diminishment. To be specific, 5 nm Ag/C showed about a 300 mV anodic shift of overpotential at 1 mA/cm² when compared with Ag foil. Furthermore, as seen in Figure 2c, mass activity of the three different nanoparticle Ag/C electrodes at various potentials followed a similar trend with CO current density normalized with an electrode area since the amount of Ag metal content was controlled using inductively coupled plasma (ICP) results in all fabricated electrodes.

The selectivity of CO₂ reduction reaction to CO was

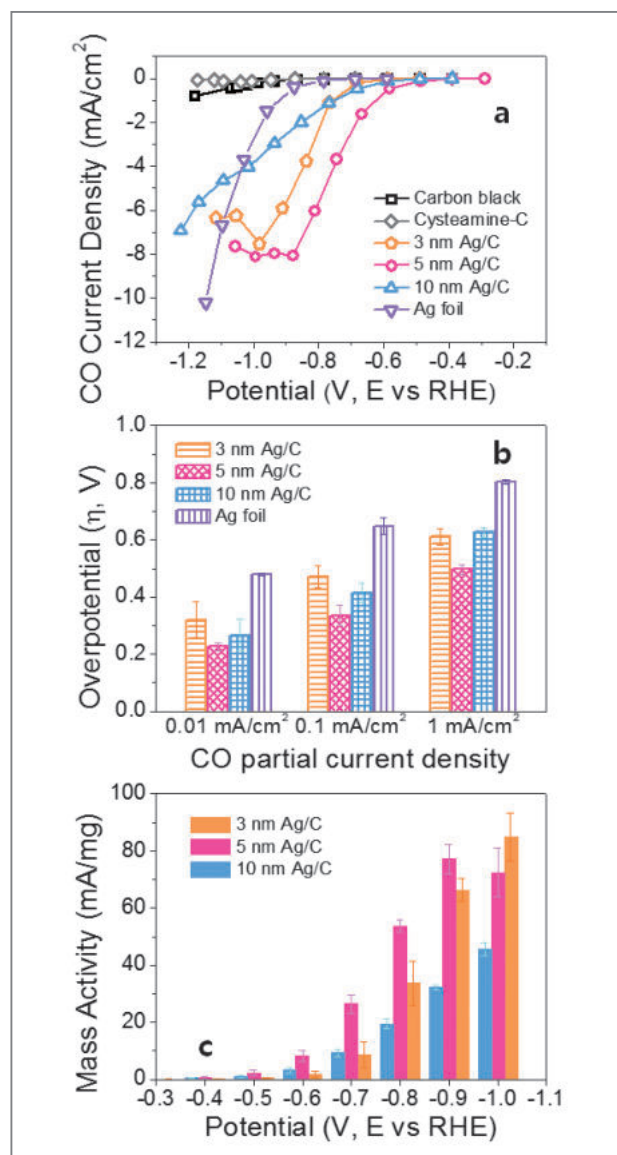


Figure 2. a) CO partial current density depending on applied potential. b) Overpotentials at fixed current densities. c) Mass activity depending on applied potential. CO₂ electrochemical reduction was performed in CO₂-saturated 0.5 M KHCO₃. The thermodynamic reduction potential for CO₂ to CO was -0.11 V vs. RHE.

also studied with the prepared Ag electrodes by varying the applied potentials (Figure 3a). The enhanced CO production selectivity was commonly notable at less cathodically biased regions with the synthesized Ag/C of three different sizes compared to that of Ag foil. Again,

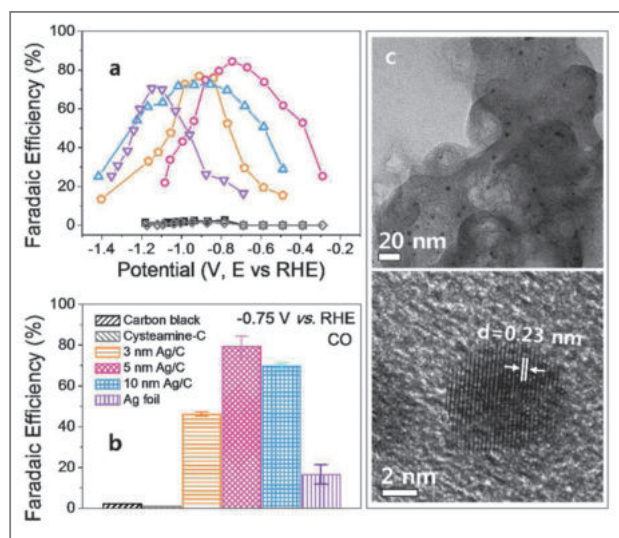


Figure 3. CO Faradaic efficiency a) depending on applied potential and b) fixed potential at -0.75 V (vs. RHE). CO₂ electrochemical reduction was performed in CO₂-saturated 0.5 M KHCO₃. c) TEM image and HR-TEM image of 5 nm Ag/C after CO₂ reduction.

the 5 nm Ag/C showed the best CO₂ reduction reaction performance, reaching its maximum CO Faradaic efficiency with the smallest overpotential (635 mV), with 10 nm, 3 nm Ag/C, and Ag foil following sequentially. In addition, the maximum CO Faradaic efficiencies were 76.8, 84.4, 72.6, and 70.5% for 3, 5, 10 nm Ag/C, and Ag foil, respectively, with 5 nm Ag/C achieving the highest CO Faradaic efficiency. When CO Faradaic efficiencies of all samples were compared at a fixed potential of -0.75 V vs. RHE, the maximum selectivity potential for 5 nm Ag/C (Figure 3b), Faradic efficiency of the 5 nm Ag/C (average F.E.CO = 79.2%) showed 4.8 times the enhancement of Ag foil (average F.E.CO = 16.5%). In our study, mass activity, overpotentials, and CO Faradaic efficiency demonstrated that 5 nm was the optimal Ag nanoparticle size for CO₂ reduction reaction application in an aqueous solution. Additionally, the TEM and HR-TEM images after CO₂ reduction reaction showed that the 5 nm Ag/C exhibited no size change and had an average size of 5.0 ± 1.0 nm (Figure 3c).

Understanding decrease of the overpotential: the role of cysteamine anchoring agent

Using DFT calculations, we examined the origin of enhanced catalytic activity of Ag/C. Previous theoretical study on the CO₂ reduction reaction mechanism has suggested that the binding energy of the COOH intermediate (ΔE_B^{COOH}) primarily determines the overpotential; higher COOH binding yields lower overpotential [14,15].

We thus calculated ΔE_B^{COOH} to particles of various sizes: 1.0 nm, 1.6 nm, 2.2 nm, and 2.7 nm cuboctahedral Ag nanoparticles (i.e., Wulff shape of Ag), which were Ag₁₃, Ag₅₅, Ag₁₄₇, and Ag₃₀₉, respectively (Figure 4a). Unsurprisingly, low coordination number (CN) sites exposed at the corners (CN=5) or edges (CN=7) strongly bound to COOH. However, the tunability of ΔE_B^{COOH} (that is directly related to the tunability of the overpotential) decreased as the nanoparticle size increased, and became only within 126 meV (the difference of ΔE_B^{COOH} for CN=5 and CN=8) even when the nanoparticle size was 2.7 nm (the largest size available within our limited computational cost). This suggests that size effects alone cannot explain the strong overpotential modulation observed from experiments varying the nanoparticle size from 3 nm to 10 nm. Notably, the previous Ag or Au nanoparticle reports only showed the changes of the CO₂ reduction current densities depending on the particle size, and the onset overpotentials for CO₂ reduction reaction were almost the same regardless of the particle size [14, 16].

We suspected that the low overpotentials with our Ag/C samples were associated with the anchoring agent, the end group of -SH in cysteamine, that could change the electronic structure in an Ag surface, as confirmed by XPS. To investigate this possibility, we performed DFT calculations of 2.2 nm Ag nanoparticles anchored with n number of cysteamine (Cys); Ag_(147-n)Cys_n (n=0, 1, 2, 4) through Ag-S bonds. As shown in Figure 4b, we

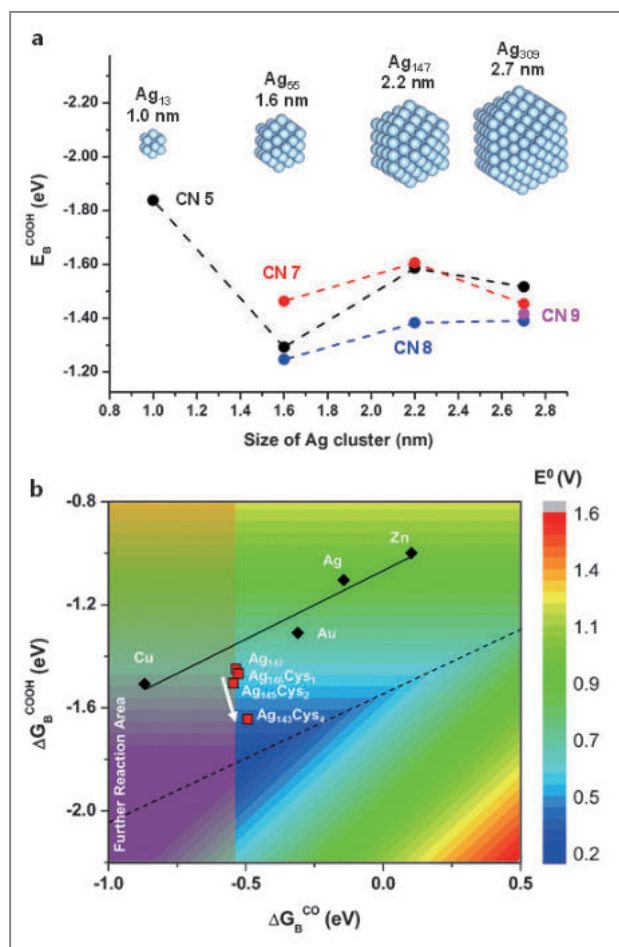


Figure 4. a) DFT results on the binding energies of the COOH intermediate (ΔE_B^{COOH}) as a function of Ag nanoparticle size. Ag_{13} (1.0 nm), Ag_{55} (1.6 nm), Ag_{147} (2.2 nm), and Ag_{309} (2.7 nm) models with cuboctahedral geometry were examined. b) Effect of anchoring agents on COOH and CO binding energies examined using $\text{Ag}_{(147-n)}\text{Cys}_n$ ($n=0, 1, 2, 4$) models.

found that ΔE_B^{COOH} showed a monotonic increase as the cysteamine coverage increased up to 261 meV as the cysteamine/Ag ratio increased up to 2.7%. Although it is difficult to experimentally quantify and/or control the cysteamine coverage of the Ag nanoparticles, we believe that our 5 nm sized Ag/C sample had optimal activity due to suitable coverage of anchoring agent, which was responsible for the remarkable reduction of overpotential. More interestingly, we found that the binding energy

of the CO showed marginal changes with respect to the effect of anchoring agent. We note that modifying the catalyst surface to preferentially stabilize the intermediate (COOH) over the final product (CO) has its own importance in enhancing the catalytic activity [18, 19].

Conclusion

In summary, silver nanoparticles with three different sizes were directly synthesized on a carbon support by a facile one-pot method using cysteamine as an anchoring agent, which initiated nucleation on the carbon support. These novel nanoparticulate Ag/C samples were effective as electrocatalysts for the CO_2 reduction reaction in an aqueous system. Catalysts using a 5 nm Ag/C sample exhibited the highest CO_2 reduction reaction activity in terms of low overpotential, high mass activity, high CO Faradaic efficiency, and high exchange current density with enhanced durability. Significant reduction of the overpotential with directly grown Ag nanoparticles on carbon supports was associated with the cysteamine anchoring agent, which developed Ag-S interaction. Our DFT studies elucidated that the Ag-S interaction induced surface localization of the unpaired electron, resulting in an enhanced intermediate stabilization, and thus, improved catalytic activity. These studies demonstrate the potential for using supported Ag nanoparticles synthesized by simple wet chemistry methods as CO_2 reduction catalysts with high mass activities and low overpotential for CO production and also suggest that anchoring groups such as cysteamine can be used to control their material properties.

Note

This article and images are drawn from “Achieving selective and efficient electrocatalytic activity for CO_2 reduction using immobilized silver nanoparticles” in

Journal of the American Chemical Society, Vol.137, pp. 13844.

References

- [1] Turner JA. *Science* 1999; 285 (5428): 687-689.
- [2] Goepfert A, Czaun M, May RB, Prakash GKS, Olah GA, Narayanan SR. *J. Am. Chem. Soc.* 2011; 133 (50): 20164-20167.
- [3] Graves C, Ebbesen SD, Mogensen M, Lackner KS. *Renew. Sustainable Energy Rev.* 2011 (1); 15: 1-23.
- [4] Centi G, Quadrelli EA, Perathoner S. *Energy Environ. Sci.* 2013; 6 (6): 1711-1731.
- [5] Mikkelsen M, Jorgensen M, Krebs FC. *Energy Environ. Sci.* 2010; 3 (1): 43-81.
- [6] Whipple DT, Kenis PJA. *J. Phys. Chem. Lett.* 2010; 1 (24): 3451-3458.
- [7] Hori Y. *In Modern Aspects of Electrochemistry*. Springer New York. 2008; Vol. 42: p 89-189.
- [8] Chen Y, Li CW, Kanan MW. *J. Am. Chem. Soc.* 2012; 134 (49): 19969-19972.
- [9] Lu Q, Rosen J, Zhou Y, Hutchings GS, Kimmel YC, Chen JG, Jiao F. *Nat. Commun.* 2014; 5: 3242.
- [10] Kim C, Kim SS, Yang S, Han JW, Lee H. *Chem. Commun.* 2012; 48 (51): 6396-6398.
- [11] Kim C, Kim J, Yang S, Lee H. *RSC Advances* 2014; 4 (109): 63677-63680.
- [12] Battocchio C, Fratoddi I, Fontana L, Bodo E, Porca-ro F, Meneghini C, Pis I, Nappini S, Mobilio S, Russo MV, Polzonetti G. *Phys. Chem. Chem. Phys.* 2014; 16 (23): 11719-11728.
- [13] Lee JS, Park GS, Kim ST, Liu M, Cho J. *Angew. Chem. Int. Ed.* 2013; 52 (3): 1026-1030.
- [14] Zhu W, Michalsky R, Metin Ö, Lv H, Guo S, Wright CJ, Sun X, Peterson AA, Sun S. *J. Am. Chem. Soc.* 2013; 135 (45): 16833-16836.
- [15] Gao D, Zhou H, Wang J, Miao S, Yang F, Wang G, Wang J, Bao X. *J. Am. Chem. Soc.* 2015; 137 (13): 4288-4291.
- [16] Salehi-Khojin A, Jhong HRM, Rosen BA, Zhu W, Ma S, Kenis PJA, Masel RJ. *Phys. Chem. C* 2012; 117 (4): 1627-1632.
- [17] Lim HK, Shin H, Goddard WA, Hwang YJ, Min BK, Kim H. *J. Am. Chem. Soc.* 2014; 136 (32): 11355-11361.
- [18] Hansen HA, Varley JB, Peterson AA, Nørskov JK. *J. Phys. Chem. Lett.* 2013; 4 (3): 388-392.



Amyloid- β Oligomers May Impair SNARE-Mediated Exocytosis by Direct Binding to Syntaxin 1a

Cell Reports

2015 Aug. / Vol. 12 No. 8 / 1244–1251

Yoo Soo YANG, Jae Wook KIM, Hye Yun KIM, Na Yeon RYOO, Se Jin LEE, Young Soo KIM, Hye Whon RHIM(hrhim@kist.re.kr), Yeon Kyun SHIN

Alzheimer's disease (AD) is closely associated with synaptic dysfunction, and thus current treatments often aim to stimulate neurotransmission to improve cognitive impairment. Whereas the formation of the soluble N-ethylmaleimide-sensitive factor attachment protein receptor (SNARE) complex is essential for synaptic transmission, the correlation between SNAREs and AD neuropathology is unknown. Here, we report that intracellular amyloid- β (Ab) oligomers directly inhibit SNARE-mediated exocytosis by impairing SNARE complex formation. We observe abnormal reduction of SNARE complex levels in the brains of APP/PS1 transgenic (TG) mice compared to age-matched wild-types. We demonstrate that Ab oligomers block SNARE complex assembly through the direct interaction with a target membrane (t)-SNARE syntaxin 1a in vitro. Furthermore, the results of the in vitro single-vesicle content-mixing assay reveal that Ab oligomers inhibit SNARE-mediated fusion pores. Thus, our study identifies a potential molecular mechanism by which intracellular Ab oligomers hamper SNARE-mediated exocytosis, likely leading to AD-associated synaptic dysfunctions.

Sustained BMP-2 Delivery and Injectable Bone Regeneration Using Thermosensitive Polymeric Nanoparticle Hydrogel Bearing Dual Interactions with BMP-2

Journal of Controlled Release

2015 Jul. / Vol. 209 / 67–76

Bo Bae SEO, Hyuck CHOI(h11502@kist.re.kr), Jeong Tae KOH, Soo Chang SONG

Localized and continuous osteogenic stimulation to defected sites is required for effective bone regeneration. Here, we suggest an injectable and sustained bone morphogenetic protein-2 (BMP-2) release system using thermosensitive polymeric nanoparticles bearing dual interacting forces with BMP-2. For sustained BMP-2 release, hydrophobic and ionic interactions were introduced to thermosensitive poly(phosphazene). Hydrophobic isoleucine ethyl ester and hydrophilic poly-ethylene glycol were mainly substituted to the poly(phosphazene) back bone for amphiphilicity and hydrophobic interaction with BMP-2. Carboxylic acid moiety was additionally substituted to the back bone for ionic interaction with BMP-2. These dual interacting polymeric nanoparticles (D-NPs) formed compact nanocomplexes with BMP-2. The aqueous solution of BMP-2/D-NP nanocomplexes was transformed to hydrogel when the temperature of the solution increased. Loaded BMP-2 was sustain-released for three weeks from the BMP-2/D-NP nanocomplex hydrogel. The extended BMP-2 exposure caused higher osteocalcin secretion in C2C12 cells. Significant bone generations were observed at the target site by single injection of BMP-2/D-NP nanocomplexes in vivo.

Remarkable Conversion Between n- and p-Type Reduced Graphene Oxide on Varying the Thermal Annealing Temperature

Chem. Mater.

2015 / 7362-7369

Nguyen Dien Kha Tu(nguyendktu@gmail.com), Jae Yoo CHOI, Chong Rae PARK, Hee Suk KIM

To allow for the use of graphene in various nanoelectronic applications, the methods for the large-scale production of graphene with controllable electrical properties need to be developed. Here, we report the results of a fundamental study on the remarkable conversion between n- and p-type reduced graphene oxide (rGO) with changes in the thermal annealing temperature. It was found that the charge carriers in rGO for temperatures of 300–450 °C and 800–1000 °C are electrons (n-type), whereas for temperatures of 450–800 °C, they are holes (p-type). This is because the individual oxygen functional groups present on rGO are determined by the annealing temperature. We found that the predominance of electron-withdrawing groups (i.e., carboxyl, carbonyl, and sp³-bonded hydroxyl, ether, and epoxide groups) resulted in p-type rGO, although that of electron-donating groups (sp²-bonded hydroxyl, ether and epoxide groups) lead to n-type rGO. In addition, as a proof of concept, a flexible thermoelectric device consisting of GO-700 and GO-1000 as p-type and n-type components, respectively, was fabricated. This device, which contained eight pairs of the two components, exhibited an output voltage of 4.1 mV and an output power of 41 nW for $\Delta T = 80$ K. These results demonstrate that the carrier characteristics of rGO can be altered significantly by changing the functional groups present on it, thus allowing it to be used in various applications including flexible thermoelectrics.

High Mobility, Large Linear Magnetoresistance and Quantum Transport Phenomena in Bi₂Te₃ Films Grown by Metallo-Organic Chemical Vapor Deposition (MOCVD)

Nanoscale

2015 Jul. / 17359-17365

Hyun Woo JIN, Kwang Chon KIM(kwang@kist.re.kr), Ju Hee SEO, Seong Keun KIM, Byung Ki CHEONG, Jin Sang KIM, Su Youn LEE

We investigated the magnetotransport properties of Bi₂Te₃ films grown on GaAs (001) substrate by a cost-effective metallo-organic chemical vapor deposition (MOCVD). We observed the remarkably high carrier mobility and the giant linear magnetoresistance (carrier mobility $\sim 22\,000$ cm² V⁻¹ s⁻¹, magnetoresistance $\sim 750\%$ at 1.8 K and 9 T for a 100 nm thick film) that depends on the film thickness. In addition, the Shubnikov–de Haas oscillation was observed, from which the effective mass was calculated to be consistent with the known value. From the thickness dependence of the Shubnikov–de Haas oscillation, it was found that a two-dimensional electron gas with the conventional electron nature coexists with the topological Dirac fermion states and dominates the carrier transport in the Bi₂Te₃ film with thickness higher than 300 nm. These results are attributed to the intrinsic nature of Bi₂Te₃ in the high-mobility transport regime obtained by a deliberate choice of the substrate and the growth conditions.

Herbal Extract Incorporated Nanofiber Fabricated by an Electrospinning Technique and its Application to Antimicrobial Air Filtration

ACS Appl. Mater. Interfaces

2015 Jul. / 25313–25320

Jeong An CHOI, Byeong Joon YANG, Gwi Nam BAE, and Jae Hee JUNG(090784@kist.re.kr)

Recently, with the increased attention to indoor air quality, antimicrobial air filtration techniques have been studied widely to inactivate hazardous airborne microorganisms effectively. In this study, we demonstrate herbal extract incorporated (HEI) nanofibers synthesized by an electrospinning technique and their application to antimicrobial air filtration. As an antimicrobial herbal material, an ethanolic extract of *Sophora flavescens*, which exhibits great antibacterial activity against pathogens, was mixed with the polymer solution for the electrospinning process. We measured various characteristics of the synthesized HEI nanofibers, such as fiber morphology, fiber size distribution, and thermal stability. For application of the electrospun HEI nanofibers, we made highly effective air filters with 99.99% filtration efficiency and 99.98% antimicrobial activity against *Staphylococcus epidermidis*. The pressure drop across the HEI nanofiber air filter was 4.75 mmH₂O at a face air velocity of 1.79 cm/s. These results will facilitate the implementation of electrospun HEI nanofiber techniques to control air quality and protect against hazardous airborne microorganisms.

Janus Pt Surfaces Derivatized with Zwitterionic Molecules for Oxygen Reduction Reactions in Alkaline and Acid Electrolytes

Nano Energy

2015 Oct. / Vol. 17 / 152-159

Nam Gee JUNG, Hye Young SHIN, Man Su KIM, In Joon JANG, Hyoung Juhn KIM, Jong Hyun JANG, Hyung Jun KIM, Sung Jong YOO(ysj@kist.re.kr)

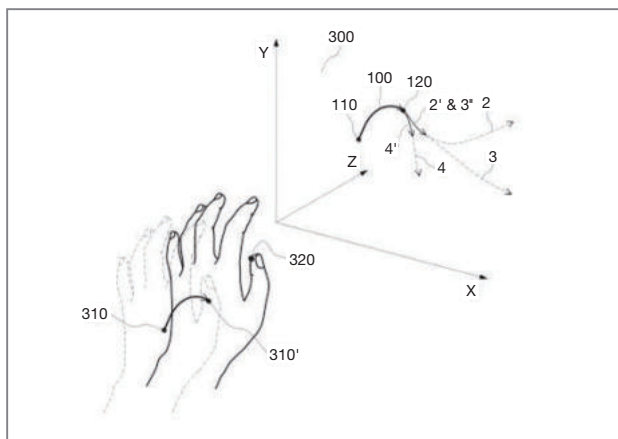
Direct electrostatic interactions between a charged Pt surface and oppositely charged spectator ions are utilized for the enhancement of oxygen reduction reaction (ORR) activity in both KOH and H₃PO₄ solutions. Zwitterionic L-cysteine molecules functionalized on a Pt surface are turned outwards to afford differing surface charges in either alkaline(-) or acid solutions(+). In KOH solution, this leads to the selective impediment of interactions between OH and K⁺ with the Pt surface through repulsive and attractive interactions of the negatively charged -COO group of L-cysteine, respectively. In H₃PO₄ solution, the phosphoric acid molecule and its anion are effectively captured by the positively charged -NH₃⁺ moieties of L-cysteine. Behaviors of the spectator species hindering the ORR are systematically controlled through direct electrostatic interactions with the functional groups of L-cysteine in each electrolyte, resulting in a Janus Pt catalyst for superior ORR in both alkaline and acid electrolytes.

System and Method for Implementing User Interface

US 9075445 (2015-07-07)

Myoung Soo PARK / meister@kist.re.kr

A system has an input device for collecting gesture information of a user, a computing device for processing the gesture information collected by the input device, a memory for storing information of executive trajectories for executing various functions, and an output device for displaying the information processed by the computing device, wherein each executive trajectory is defined as an executive input for each function, if a gesture performed by the user completes one of the executive trajectories, a function corresponding to the corresponding executive trajectory is executed, wherein, if the user starts a gesture, the computing device compares a path of a trajectory of a gesture performed by the user with start paths of the executive trajectories and selects candidate trajectories having similarity higher than a preset criterion, and wherein the candidate trajectories are displayed by the output device to suggest path information of the candidate trajectories to the user.

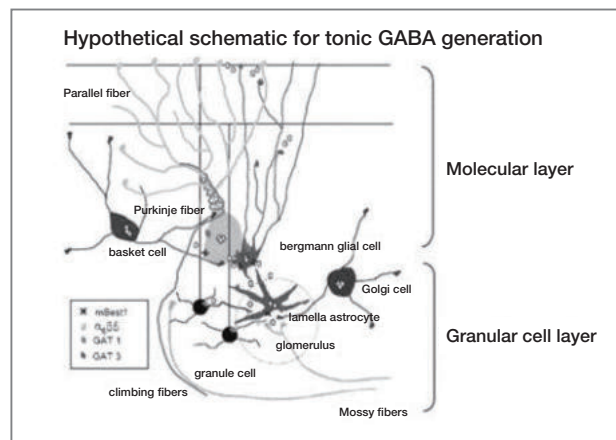


GABA Release-Regulating Agent in Cerebellum

US 9095535 (2015-08-04)

Changjoon Justin LEE / cjl@kist.re.kr

A GABA (gamma-aminobutyric acid) release-inhibiting agent in the cerebellum and a composition for treating pathological symptoms caused by over-release of GABA in the cerebellum, each comprising a Bestrophin 1 (Best1) channel inhibitor as an active ingredient; a GABA release-promoting agent in the cerebellum and a composition for treating pathological symptoms caused by the deficit of GABA in the cerebellum, each comprising a Best1 channel activator as an active ingredient; and a method for screening a GABA release-regulating agent in the cerebellum, which uses Best1 channel as target, are provided.

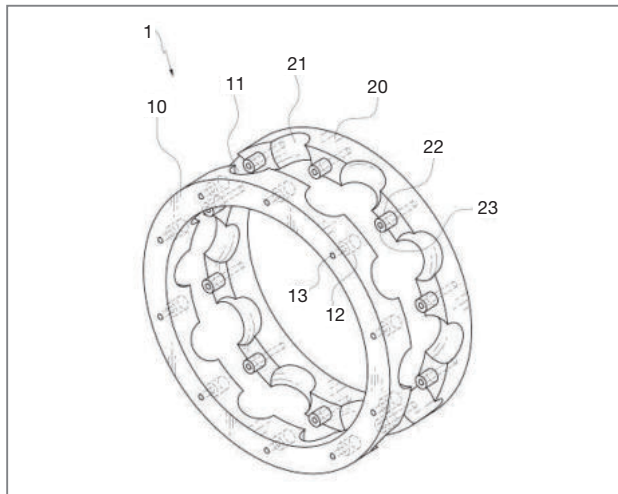


Cage for Rolling Bearing

US 9121450 (2015-09-01)

Yong Bok LEE / lyb@kist.re.kr

A cage for a rolling bearing is coupled to a rolling bearing including an inner ring, an outer ring and a plurality of rolling elements rolling between the inner ring and the outer ring to keep intervals of the plurality of rolling elements, wherein the plurality of rolling elements include bodies coupled along a circumference thereof at predetermined intervals, wherein each of the bodies includes a first piece and a second piece which are attachable to each other and detachable from each other. A first coupler and a second coupler configured to be capable of being coupled to each other are respectively formed at the first piece and the second piece, and the first piece and the second piece are primarily coupled by means of a coupling force of the first coupler and the second coupler.

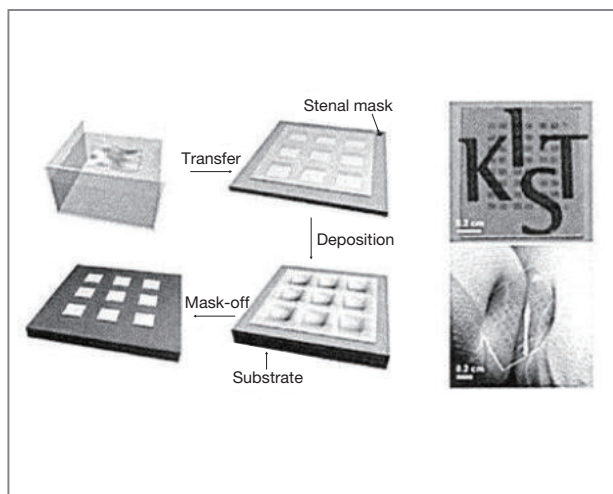


Hybrid Electronic Sheets

US 9226403 (2015-12-29)

Hyun Jung YI / hjungyi@kist.re.kr

In accordance with the present disclosure, a hybrid electronic sheet which exhibits superior electrical property and allows biomaterial functionalization and flexible device patterning may be provided by binding a graphitic material in colloidal state to a biomaterial capable of binding thereto specifically and nondestructively. Since the electronic sheet is an electronic sheet wherein a biomaterial and an electrical material (graphitic material) are hybridized, it exhibits good compatibility with biomaterials and can be further functionalized with, for example, an enzyme that selectively reacts with a biochemical substance. Accordingly, an electrical material and a chemical or biological material may be effectively nanostructured and it can be realized as a multi-functional, high-performance electronic sheet.

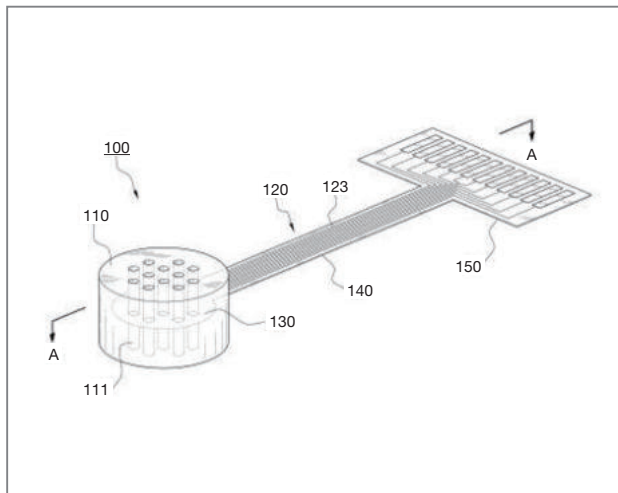


Neural Tube for Recovering Function of Injured Nerve

US 9220426 (2015-12-29)

Jin Seok KIM / jinseok@kist.re.kr

A neural tube capable of complexly playing roles of a support for regenerating a nerve and a nerve electrode has a support connected to a terminal of an injured nerve, and a sieve electrode having an electrode hole formed in a body thereof and a circular electrode formed around the electrode hole, wherein the body of the sieve electrode is buried in the support, wherein a cavity-type channel is formed at the support to extend to the inside of the support, wherein the electrode hole is aligned with the channel, and wherein a nerve cell growing along the channel at the terminal of the injured nerve is capable of contacting the circular electrode.

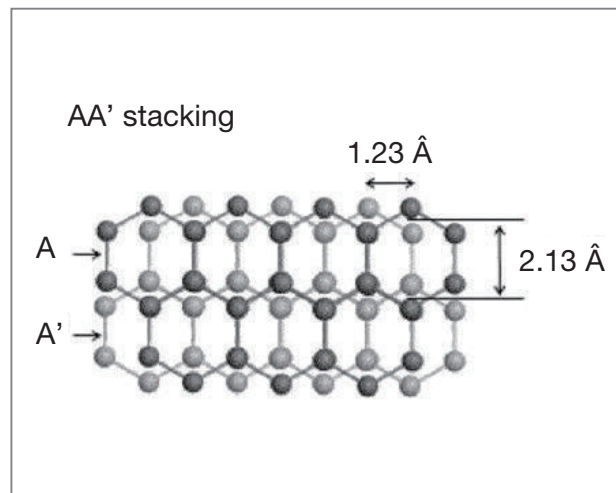


AA' Stacked Graphite and Fabrication Method Thereof

US 9200363 (2015-12-01)

Jae Kap LEE / jklee@kist.re.kr

Disclosed is AA' graphite with a new stacking feature of graphene, and a fabrication method thereof. Graphene is stacked in the sequence of AA' where alternate graphene layers exhibiting the AA' stacking are translated by a half hexagon (1.23 Å). AA' graphite has an interplanar spacing of about 3.44 Å larger than that of the conventional AB stacked graphite (3.35 Å) that has been known as the only crystal of pure graphite. This may allow the AA' stacked graphite to have unique physical and chemical characteristics.

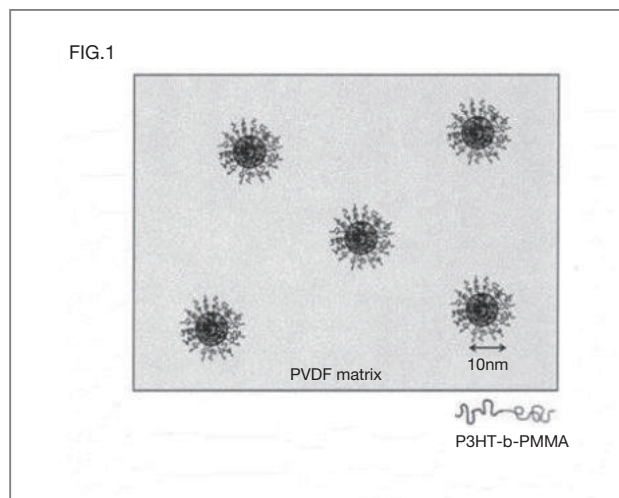


Polymer Blend Composition and Actuators Using the Same

US 9123892 (2015-09-01)

Chong Min KOO / koo@kist.re.kr

The present invention relates to a polymer blend composition comprising a dielectric elastomer, an actuator film manufactured using the same, and an actuator comprising the film. The polymer blend composition according to the present invention comprises a block copolymer having excellent compatibility with the dielectric elastomer and excellent dielectric properties, and thus displacement values suitable for the purpose can be obtained by a simple method of adjusting a composition of the polymer blend. Moreover, the film manufactured using the same has high dielectric constant, low dielectric loss and high electromechanical displacement, and thus the film exhibits excellent dielectric properties when it is applied in a dielectric layer for an actuator.



1. Ceremony Commemorating the 50th Anniversary of KIST

February 4, 2016

To mark the 50th anniversary of KIST's foundation, a ceremony was held on February 4th at KIST's main campus in Seoul. More than 450 guests, staff and faculty attended, including South Korea's prime minister, Kyo Ahn Hwang, the 1st vice minister of Science, ICT and Future Planning, Yang Hee Choi, the US ambassador to Korea, Mark Lippert, and many other special guests.

In his congratulatory remarks, Prime Minister Hwang said that the institute's past achievements were testament to its ability to develop the core technologies needed to bring about a better future for everyone. These efforts would enable the creation of new growth engines through commercial development of these technologies.

KIST's president, Byung Gwon Lee, announced the institute's new slogan, *KIST 2066, Beyond the MIRACLE*, introducing the institute's new vision and renewing its commitment to surpass the accolades and research achievements of the past half century and reach beyond the boundaries of Korea by becoming a truly global institute, exploring new frontiers of research while serving as the R&D center of the nation.

After the ceremony, a time capsule was buried in the 50th Anniversary Park. The time capsule was filled with many photos of memorable moments as well as books, souvenirs and letters to be opened in 50 years, a message to connect the past, present and future of KIST.



2. KIST Transferred the Technology of Early Diagnosis of Alzheimer's to Iljin Group and Doosan Engine Co. Granted KRW 5 Billion to Support Field Lab

February 1 & February 23, 2016

KIST recently succeeded in developing a technology for the early detection of Alzheimer's disease and then successfully transferred this technology to Alpnion Medical Systems Company, a subsidiary of ILJIN Group, for commercialization. This transfer was formalized in an agreement signed by Dr. Byung Gwon Lee, president of KIST, and Seok Bin Go, CEO of ILJIN Group, on February 1st.

With funding provided by the Ministry of Science, ICT and Future Planning, the KIST research team of Dr. Tae Song Kim, Young Sun Kim, and Kyo Sun Hwang developed a technology for a general blood test to detect the possible presence of Alzheimer's disease in its early stages. A seminar was held last November for around 40 medical equipment and pharmaceutical companies to introduce the technology.

The detection of Alzheimer's disease has been dependent on functional testing or brain MRIs, methods which are costly and can produce inaccurate diagnoses. By contrast, KIST's newly developed innovative technology enables low-cost and efficient detection of the disease before symptom onset with a simple blood test.

Korea's Ministry of Science, ICT and Future Planning is prepared to provide ongoing support for early commercialization efforts, follow-up research and overseas marketing to realize the full potential of the technology and secure global markets. According to a source within the ministry, "By organizing a team of experts to provide extensive support, from medical equipment approval and new medical technology evaluation, we will make an all-out effort to complete the process of evaluation and approval by the first half of next year. Also, with inter-departmental cooperation, we will make sure to provide support for follow-up



researchers to refine early detection technology for mild cognitive impairment as well as leverage overseas networks for global marketing.”

Chairman Jin Gyu Hur of ILJIN Group said “We will focus our entire organization on rapid commercialization of the technology and have no doubt that the technology will make a great contribution to reducing the national and social costs associated with Alzheimer’s by improving public health.” President Byung Gwon Lee of KIST added, “Even after the technology transfer, the institute will continue to refine the early detection technology and make an effort to include it as an essential item in the national health check-up program.”

According to the National Assembly Budget Office, the social expense attributable to Alzheimer’s in Korea was estimated to be KRW 12 trillion in 2015. By 2025, 1 million out of an estimated population of 11 million elderly are expected to suffer from dementia, and more than 70% of them are expected to be Alzheimer’s patients. Given the prevalence of this disease not only in Korea but on an international scale as well, the economic potential of an easy, accurate diagnostic test is immense. The total value of the technology transfer is estimated to be more than KRW 330 billion, including advance payments and ongoing royalties.

KIST and Doosan Engine Co., a subsidiary of the Doosan Group, signed an agreement on February 23rd for the provision of KRW 5 billion to establish a lab in the field and facilitate research cooperation to develop a next-generation eco-friendly catalyst. This agreement grew out of research by a KIST team led by Dr. Heon

Phil Ha to develop a denitrogenation catalyst for ship fuel gas processing. For the first time in the world, the team succeeded in developing a low-temperature denitrogenation catalyst for fuel gas. In the past, international research had focused on installing a catalyst on the front section of a supercharger, but in 2015, KIST and the Doosan Engine Co. became the first to develop and demonstrate the technology to process fuel gas in low temperatures in the rear section of the supercharger of a ship.

Anxious to build on their success, KIST and Doosan Engine agreed to a longer-term relationship for the development of eco-friendly catalyst technology based on their experience that the convergence of materials technology researched at government-funded institutes and system development by industry can speed up the development process. With this renewed commitment, the parties will continue efforts to improve competitiveness, secure a technology base and build a growth engine for the shipbuilding industry of Korea.

To this end, Doosan Engine has agreed to provide KRW 5 billion in research funds (annual funding of KRW 500 million for 10 years) and cooperate for early commercialization of the technology with support of existing engine models and demonstration technologies. The catalyst technology developed in 2015 has already been applied and a dozen ship engines are being manufactured with this technology. This represents a prime example of the benefits of cooperation among small/medium sized businesses, who are manufacturing the catalyst modules and materials, large-scale industry, and a government-funded institute.

President Byung Gwon Lee of KIST stressed the importance of such arrangements by saying, “KIST will not stop at just developing original technologies. It will make an all-out effort for commercialization to ensure that these technologies lead to national growth engine development and job creation in these industries.” Confirming the importance of working together, Dong



Chul Kim, CEO of Doosan Engine, said, “Following the global trend of interdisciplinary technology cooperation, Doosan has experienced great success by converging technologies developed by government-funded institutes with industrial technologies. I expect that *Open Innovation* cooperation with KIST will lead to even greater success.”

The market for eco-friendly materials technology in the shipbuilding industry, which is estimated by industry sources to reach KRW 900 billion by 2019, is still growing. In addition, the International Maritime Organization is toughening regulations on fuel gas from vessels. Both of these factors are expected to create significant demand for improved fuel gas catalyst technologies.

3. President Geun Hye Park Attends Special Celebrations at KIST

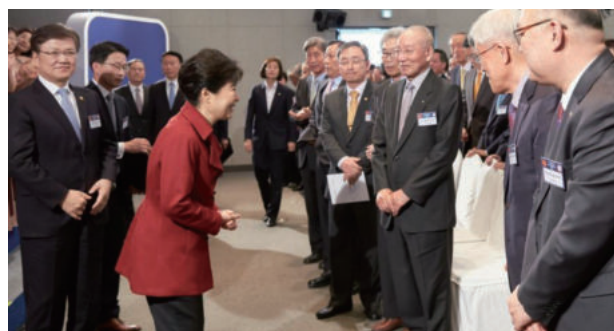
April 21, 2016

Korean president Geun Hye Park attended a ceremony at KIST on April 21st celebrating the 49th Science Day and 61st Information and Communication Day.

Before the ceremony, President Park met with six senior scientists who are members of the first generation of science and technology pioneers in Korea. The scientists included five from KIST, Drs. Eun Young Kim, Hoon Cheol Kim, Tak Jin Moon, Young Ok Ahn and Yeo Kyeong Yoon, and one from the Korea Atomic Energy Research Institute (KAERI), Dr. In Soon Jang.

During the meeting, President Park described how meaningful it was to meet with senior scientists on such a special occasion and emphatically stated that Korea owed its remarkable development to the many scientists who sacrificed personal opportunities for research in advanced countries to help Korea at a time when it was struggling economically. They did so even though they had to conduct their research in Korea under primitive conditions. President Park acknowledged that KIST was built on the pride and patriotism of these scientists.

The senior scientists shared a number of memories and insights with President Park. Dr. Young-ok Ahn brought a letter to the meeting from then President Jung Hee Park to Donald F. Hornig, the U.S. presidential science advisor in 1965. Upon seeing the letter, President Park harked back to the time when Korea had to receive international aid from advanced nations, but how thanks to the senior scientists’ continuous efforts, Korea was transformed from the world’s poorest country into one of its most advanced nations. Dr. In Soon Jang described building a nuclear reactor designed by Korean scientists in the U.S. President Park commented that now Korean nuclear engineers are designing SMART (Small and Modular Reactor) for export to Saudi Arabia. Dr. Tak Jin Moon shared an anecdote about President Jung Hee Park, who assigned all important scientific research projects to KIST at that time. Dr. Hoon Cheol Kim explained the process for technological transfer to President Park. Dr. Yeo Kyeong Yoon reiterated how researchers and scientists in the early days of KIST were focused on



ways to advance S & T in Korea. Unlike today, they did not have the option of choosing projects on the basis of personal interests, but only thought of ways to benefit the nation and chose projects accordingly. Dr. Yoon also described a meeting he had had with President Jung Hee Park while working on an integrated iron and steel project. When the retired Dr. Eun Young Kim mentioned how he spent his entire professional career at KIST, President Park thanked him for his contribution in advancing the nation.

4. POCOG Signs KIST as Institute for Doping Sample Analysis at 2018 Olympics

January 25, 2016

The Organizing Committee for the 2018 Pyeongchang Olympic & Paralympic Winter Games (POCOG) and KIST have agreed that KIST will be the agency responsible for doping testing during the 2018 Pyeongchang Winter Olympic games. This agreement was formalized in an MOU signed on January 25th. POCOG Secretary General Hyung Koo Yeo, KIST President Dr. Byung Gwon Lee and other officials attended the signing ceremony.

The KIST Doping Control Center was established in 1984 and is one of 34 labs in the world accredited by the World Anti-Doping Agency (WADA). The center is renowned for its accuracy in testing for prohibited substances in sports.

POCOG Secretary General Hyung Koo Yeo marked the agreement by saying, “It is my pleasure to see POCOG and KIST join forces together to keep performance enhancing drugs away at the 2018 Pyeongchang Winter Olympic Games. I hope our two organizations’ partnership protects athletes and keeps them healthy and makes the 2018 Winter Olympic Games a success.” During the signing ceremony, KIST President Byung Gwon Lee expressed his confidence that KIST would provide the highest standard of service. “The



KIST Doping Control Center has an impressive record of detecting prohibited drug use as evidenced by the detection of doping by Ben Johnson, a former Canadian sprinter, during the 1988 Seoul Olympic Games. For the 2018 Pyeongchang Winter Olympic Games, the KIST Doping Control Center will utilize its accumulated technological expertise and know-how to provide the best possible support for the event.”

5. MSIP Minister Yang Hee Choi delivers a lecture at KIST

February 15, 2016

On February 15th, Minister Yang Hee Choi of the Ministry of Science, ICT and Future Planning (MSIP) delivered a lecture at KIST entitled “Challenges for the Future of Science and Technology Development.” After the lecture, he held a discussion session with KIST researchers.

Minister Choi praised the hard work of KIST researchers who have contributed to Korea’s economic growth over the past five decades. The minister encouraged researchers to challenge themselves and develop creative and innovative technologies that will change the world for the better.

After delivering his lecture, Minister Choi toured a number of research centers and labs at KIST, including the Robotics and Media Institute and the Brain Science Institute. During his visit, Minister Choi stated that “MSIP supports a researcher-oriented R&D environment



where researchers can focus on their work without being distracted by other problems.”

6. KIST Europe Celebrates its 20th Anniversary

May 6, 2016

On May 6th, KIST Europe, the European branch of KIST located in Saarbrücken, Germany, held a ceremony to celebrate its 20th anniversary. Approximately 200 distinguished guests attended, including the Korean ambassador to Germany, Kyung Soo Lee, the minister-president of Saarland, Annegret Kramp-Karrenbauer, National Research Council of Science & Technology (NST) chairman, Sang Chun Lee, and KIST president, Byung Gwon Lee.

In her congratulatory remarks, Minister-President Kramp-Karrenbauer expressed her appreciation to KIST Europe for its role in improving the Saarland state's economy, while wishing the institute continued success in the future. The chairman of the NST, Sang Chun Lee, commended KIST Europe's achievement over the past 20 years and emphasized how important its role has been as a bridge between Korea and Europe.

Following the 20th anniversary ceremony, KIST Europe announced its new vision statement as expressed by KIST Europe's current director, Kui Won Choi, who described the organization as an “open research hub supporting Korean research institutes and the business sector.” Dr. Choi renewed his commitment to strengthen KIST Europe's position as a global research institute

through open research programs. His remarks were followed by the unveiling of a statue of Chun Sik Lee, the first director of KIST Europe. During his tenure, Director Lee set up the branch's operations while working hard to promote Korean-German scientific and technological collaboration. In recognition of his contribution, the German federal government awarded the Officer's Cross of the Order of Merit of the Federal Republic of Germany to Dr. Lee in 2007.

Established as Korea's only overseas government-funded research institute, KIST Europe acquires advanced and source technologies from Germany and EU member countries, promotes technical exchange and joint research projects with EU member countries, and supports Korean businesses entering the European market. KIST Europe is gearing up to strengthen its position in the European scientific field and to increase the number of joint research projects. KIST Europe operates joint labs with Lotte Fine Chemical, Saarland University, the Advanced Technology Center Association (ATCA) and the Korea Research Institute of Standards and Science (KRISS).

In conjunction with KIST Europe's 20th anniversary, several new collaborations have recently taken place, including the signing of a letter of intent with Helmholtz Centre for Infection Research (HZI) to establish a joint research institute and the signing of an agreement with the Korea Research Institute of Chemical Technology (KRICT) to establish a joint lab. In addition, KIST Europe hosted a variety of academic events in May, including the Bio Korea in Europe Symposium, Environmental Safety Technology Symposium and Energy Workshop.



KIST Chronicle

After the Korea Institute of Science & Technology was established in 1966 with the aid of the Korean and U.S. governments, Philip M. Boffey wrote an article which appeared in the March 1970 issue of the influential American scientific journal *Science*. In that article, he questioned whether KIST would be successful in the long run. He went on to make the following recommendations: 1) improve the science and technology capability of Korea; 2) encourage economic growth by developing technologies that are in line with demand from the industrial sector; and 3) attract competent scientists from abroad to work at the institute. He voiced his concern that KIST would face many obstacles along the way, likening KIST to “an infant starting to crawl” a comment first made by Richard F. Goodrich of USAID.

Fifty years later, President Byung Gwon Lee wrote an editorial for *Science* which appeared in the



February 2016 issue. In it, he answered the question originally posed by Mr. Boffey with an unequivocal “YES.”

“This month marks the 50th anniversary of Remarkably, half a century ago, South Korea was one of the poorest countries in the world, recovering from the Korean War and facing serious economic difficulties. Today, it is a member of the G20 major global economies with a market value that ranks 11th in the world.

Investment in science and technology as a development strategy is what made South Korea one of the world’s fastest-growing economies.

Now, as the nation promotes its new Creative Economy plan, KIST moves into its next 50 years, ensuring that science and technology remain the foundation of this new era of innovation.”

(See <http://science.sciencemag.org/content/351/6276/895.full>)

KIST’s success over the last half century can be summarized as follows.

1. Brief History of Korea’s S&T Development

Right after the Korean War, there was almost no governmental support

for the R&D sector in Korea. Most scientific research was conducted by private entities. Starting in the 1960s, the Korean government established a governmental department for S&T, and soon, government-funded institutes such as KIST were built. During this period, most research in Korea was focused on agricultural technology. In the next decade, heavy industry in the automobile, steel and shipbuilding sectors was promoted through new government policies to bring about economic growth and modernization of the nation. In the 1980s, the Korean government increased the budget for funding science and technology, and the private sector began to realize the importance of R & D. This increased the national focus on science and technology capped by Korea’s successful hosting of the 1988 Olympic Games. Bio/medical advances, nuclear energy, ICT, and space technology were the focus of development in the 1990s, and now, in the 21st century, Korea and KIST are increasingly investing in convergence research.

2. KIST’s Contribution to Korean Development

To commemorate the 70th anniversary of Korean liberation, the Ministry of



Science, ICT and Future Planning selected 70 of the most important S&T research achievements in Korea's post-liberation history based on their level of contribution to the nation and its economy. 10% of the selected research achievements were attributable to KIST, the highest portion of any single institute. The seven notable research achievements were the development of: ① the first computer in Korea ② polyester film ③ high strength aramid fiber ④ optical fiber for optical communication ⑤ doping control technology ⑥ fluoride manufacturing technology ⑦ industrial diamonds.

3. The 6th Most Innovative Government-Funded Research Institute in the World

In March 2016, Reuters published their rankings for the most innovative research institutions in the world, in which KIST placed 6th. Each year, Reuters prepares its rankings based on publication and patent filing data collected by its sister company, Thompson Reuters Intellectual Property and Science. (<http://www.reuters.com/article/us-innovation->

rankings-idUSKCN0WA2A5)

The 2016 ranking criteria were determined as follows.

1. The process was initiated by identifying government-operated or -funded research organizations and then determining their number of publications from 2008 to 2013 as indexed in the Thomson Reuters Web of Science database.

2. The results of publication research were cross-referenced to an organization's number of patents filed during the same time period in the Derwent World Patents Index and the Derwent Innovations Index.

3. Only the publications and patent filings completed by July 2015 were included in the ranking calculations.

4. Only organizations with 70 or more World Intellectual Property Organization (WIPO) patent filings were considered as candidates for ranking.

France's Alternative Energies and Atomic Energy Commission (CEA)

placed first in the ranking. Germany's Fraunhofer Society and Japan's Science and Technology Agency ranked 2nd and 3rd, respectively. KIST ranked 6th in the world and 2nd in Asia. KIST is the only organization in Korea that made the top 25 list and was ranked higher than many world-renowned institutions such as the National Institute of Advanced Industrial Science & Technology of Japan (7th), the Helmholtz Association of Germany (11th), RIKEN of Japan (13th), and the Max Planck Society of Germany (15th).

Philip M. Boffey concluded his March 1970 article by musing, "[. . .] if KIST eventually learns to stand and walk, it may indeed prove to be a prototype for bringing science to the service of developing nations."(Science 1970; vol.167, p.1357) Now, after successfully learning to stand and walk, KIST is ready to sprint into the future.



KIST CENTER FOR FUNCTIONAL
CONNECTOMICS (CFC)

Jin Hyun KIM

Dr. / Director



A small Asian girl went to visit an advanced research institute in Germany. Despite not speaking a word of German, she was determined to get her doctoral degree there. She was stopped at the gate, but a chance encounter with one of the researchers on staff opened the doors of the institute for her, where she ultimately earned her degree. This is how Dr. Jin Hyun Kim, director of KIST's Center for Functional Connectomics (CFC), began her journey to become a leader in the field of brain science.

Dr. Kim recalls "Back then, Korean researchers who studied abroad only considered going to the U.S., and as a result, were only familiar with U.S. research culture. I wanted to have a different research experience. That's why I decided to study in Germany, where the focus is on traditional technology. I have always had a strong interest in cancer and brain-related matters. So in Germany, I started concentrating on studying the brain. I was in my

early 20s when I flew to Germany right after graduating from a domestic university. I was young."

Dr. Kim worked as a researcher in the U.S. after earning her doctorate in Germany. She returned to Korea in 2011 through an invitation from KIST through the World Class Institute (WCI) program. KIST CFC is now developing target identification methods using brain circuit map analysis to investigate causes of brain diseases and come up with treatments. Dr. Kim has successfully developed a technology displaying the nerve network of a mouse brain in 3D images and has also identified what makes certain people have an excellent memory.

Recently, Dr. Kim's team was selected as the winner of a 2016 Human Frontier Science Program (HFSP) grant in the life science field. Out of 675 applicants, only 25 teams were selected as grant winners. Dr. Kim's team is

only the second team ever to win this grant in Korea.

What is HFSP?

The Human Frontier Science Program (HFSP) is a pan-government international program that awards research funds to outstanding research teams. It was launched in 1989. 14 member nations including Korea, the U.S., Japan and the U.K, collectively provide research grants to scientists in the fields of life science, mathematics, physics, chemistry, etc. So far, 5,500 scientists in 60 nations have been awarded grants. HFSP is also known as the “Nobel Prize Fund,” as 26 scientists financially supported by this program went on to win the Nobel Prize. In 2009, three out of six Nobel Prize winners in medicine and chemistry were former HFSP grant recipients.

Building a map of the mouse lemur brain neural network - Applying research results to uncover the mystery of the human brain

After the project prep period, Dr. Kim and her team will work on building a map of a mouse lemur brain neural network. The process will encompass researching art molecular anatomy, neuronal activity monitoring, and optogenetics. In the course of building the map, the team will investigate the causes of neurological disorders and potential treatments.

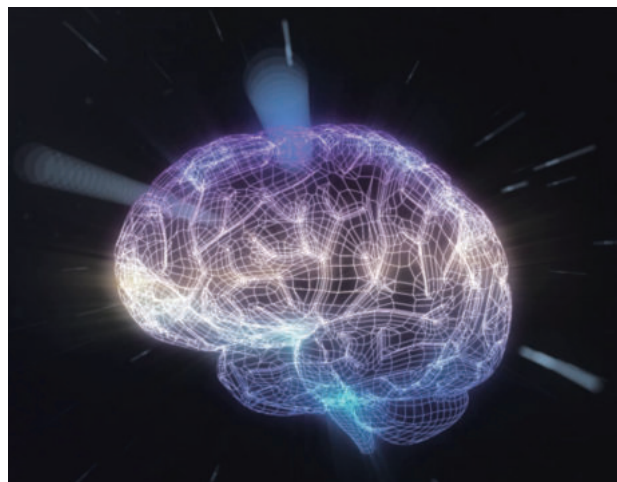
Dr. Kim will team up with two overseas research teams, one led by Professor Daniel Huber at the University of Geneva and the other by Dr. Fabien Pifferi from the French National Center for Scientific Research in Paris. This fulfills a requirement of the HFSP grant which is given only if a project involves collaboration between three or more research teams from different nations.

Each of the team participants brings an important component to the project. Professor Daniel Huber specializes in neuronal activity monitoring in living bodies based on behavioral paradigms. Dr. Fabien Pifferi has expertise in neuroethology and access to more than

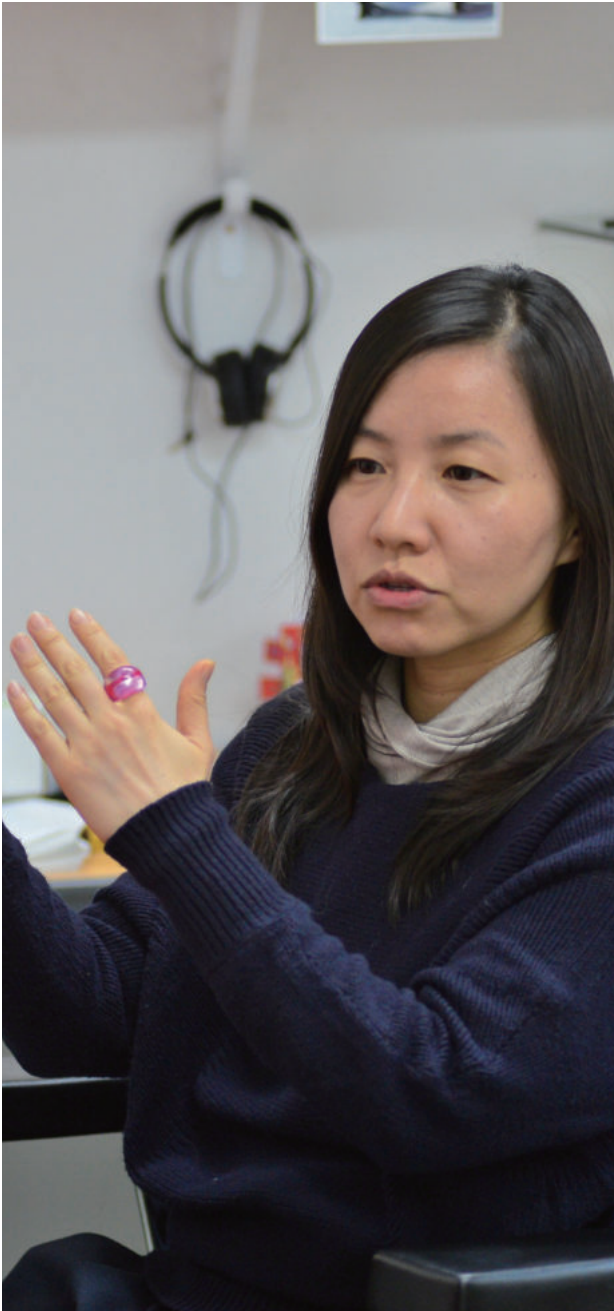
400 mouse lemurs. The KIST research team offers advanced technologies for molecular and anatomical analysis of the brain. In the words of Dr. Kim, “The joint research group is set to establish various new model systems in neuroscience research by working together and combining each other’s expertise.”

Generally in neuroscience, even though the brains of primates most closely resemble the human brain, many labs use rodent brains for research as there is limited access to primate brains. The mouse lemurs are the smallest known existing primates, and they are the optimal research subject due to a relatively short gestation period. Their brain size is similar to that of a rodent, allowing the research techniques acquired in rodent studies to transfer to mouse lemur studies. In the past, Director Kim has conducted research projects primarily using the brains of mice. Now however, she will be able to utilize mouse lemur brains, thanks to her project partners.

“As there hasn’t been much research using mouse lemurs, the results of this research are expected to be innovative and game-changing. Our goal is to use the results of mouse lemur studies to understand the human brain,” Dr. Kim explained. She went on to say, “Our team has a keen interest in Parkinson’s disease and autism. An autistic person may exhibit traits of a genius in one aspect while exhibiting little social skill. So far, there are only



hypotheses about what causes autism, and the exact cause has not yet been identified. We are focusing on building a map of the brain that may show the exact causes of dementia and autism.”



KIST CFC Director Jin Hyun Kim shared some of her personal background with our *KISToday* interviewer.

Q1 When did you start developing an interest in science?

When I was young, I liked observing ants and bugs in the front yard. I came to have more interest in science when I started taking biology classes at school.

Q2 What made you focus on brain science out of the many topics in biology?

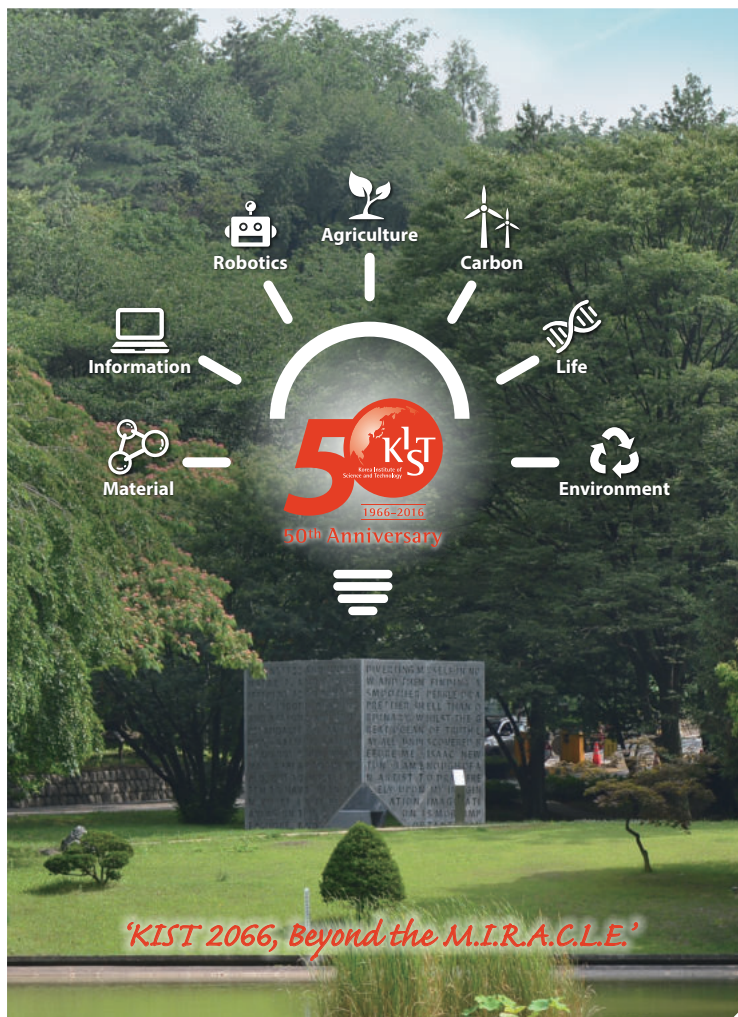
When I was an undergraduate student majoring in botany, I was interested in so many different areas of biology. “How do human beings think?” “Why does taking a pill make us feel better?” I was curious about all those things and this curiosity ended up leading to studying brain science in Germany.

Q3 After finishing your undergraduate studies, you flew to Germany without much preparation. Why did you choose Germany?

I went to Germany to learn about their doctoral programs. Back then, the majority of Korean researchers who studied abroad went to the U.S. and some to Japan. Thus, their approach to research was heavily influenced by American research culture. I wanted to experience something different.

I visited Max Planck Institute without any appointment and was stopped at the gate from entering the institute. Peter, who later became my academic adviser, happened to see me there. Amazed by my courage (or ignorance) in visiting the research institute without an appointment, he gave me a tour of his lab and suggested applying for the doctorate program. That’s how I ended up studying there.

I still keep in touch with Peter as well as Rolf Sprengel, my other academic advisor. In 2014, I invited Dr. Sprengel to KIST for that year’s Brain Pool Project.



Cover image :

KIST 50TH Anniversary Commemorative Sculpture,
“ The Meditation Pavillion”

The first president of KIST, Dr. Hyung Sub Choi’s inspirational sayings on virtues that researchers ought to have are carved on one side of the sculpture. The white icons represent materials, information, robotics, agriculture, carbon, life, environment, the seven research fields the present day KIST particularly focuses on. It is considered that the research outcomes from those fields will determine how well Korea will perform economically in the future.

Material	Develop the Next Generation Materials and Elements
Information	Lead the Post-Digital Era
Robotics	Realize Coexistence between Humans and Robots
Agriculture	Be a Mover in Agricultural Revolution
Carbon	Be a Post-Climate System Leader
Life	Pioneer the Bio & Medical Field in Aging Society
Environment	Realize a Sustainable Green City

Editorial Information

Editor-in-Chief
Tae Hoon Lim

Editorial Board Members

Il Joo Cho
Bradley Baker
Hyun Kwang Seok
Joonyeon Chang
Jong Ho Lee
Seok Won Hong
Young Soon Um
Eui Seong Kim
Gi Hong Yeum

Managing Editor

Jin Soo Kim
jinsoojs.kim@kist.re.kr
+82-2-958-6155
Web Address
www.kist.re.kr/en

English Advisory Services

Anne Charlton
The Final Word Editing
Services
the_final_word@live.com

KIST Korea Institute of
Science and Technology

5 Hwarang-ro 14-gil Seongbuk-gu Seoul 02792
Republic of Korea
Tel +82-2-958-6039 www.kist.re.kr/en
E-mail sarachang@kist.re.kr

KIST Europe

Open Research Platform for Korea-EU
R&D Collaboration and Industry Support



KIST Europe, located in Germany, has served as a bridge between Korean and European R&D institutes and industries since 1996. Furthermore, it provides guidance and assistance to the Korean companies seeking to establish their businesses in Europe and vice versa. KIST Europe carries out Open Research Programs in the fields of environment, energy, and integrative bio- and nano-engineering.

Research Fields

- Alternative Ecotoxicity Assessment & Computational Toxicology
- Bio- and Environmental sensors
- Electrochemical Energy Transformation & Storage
- IoT-based Smart Technology

Industry Support

- Chemical Regulation Compliance (REACH, K-REACH & REACH-like regulations)
- Technology Commercialization
- Technology Consultation

Tel. +49-(0)681-9382-0

e-mail info@kist-europe.de

Fax. +49-(0)681-9382-109